3/21/86

AN EXPERIMENTAL AND THEORETICAL STUDY OF THE ATMOSPHERIC SODIUM LAYER USING A LIDAR SYSTEM

BY

ANDREW C. SEGAL

B.S., Rensselaer Polytechnic Institute, 1980
M.S., University of Illinois, 1982

THESIS

Submitted in partial fulfillment of the requirements
for the degree of Doctor of Philosophy in Electrical Engineering
in the Graduate College of the
University of Illinois at Urbana-Champaign, 1986

Urbana, Illinois

ABSTRACT

Measurements of atmospheric sodium were made using the sodium lidar system at the University of Illinois. These measurements were analyzed, using signal processing techniques, to determine gravity wave effects seen in the data, to estimate the parameters of gravity waves, and to determine the variation in spectral energy with time of the gravity waves using the Wigner distribution. The seasonal and nocturnal variations of the sodium layer over Urbana, Illinois were measured by calculating the variations in the height, width, and column abundance of the sodium layer during this study. In addition, the seasonal variation of the gravity wave parameters was also observed.

The model of one gravity wave propagating in the sodium layer was extended to include the effects of two gravity waves in the sodium layer and also a gravity-wave/critical-layer interaction in the region of the sodium layer. The two gravity wave model was shown to agree closely with the data. The gravity-wave/critical-layer model predicted standing waves in the sodium layer which have been reported by other lidar studies.

ACKNOWLEDGMENTS

TABLE OF CONTENTS

LIST OF FIGURES

[1981]), Sao Paulo, Brazil (23^{o}S, 46^{o}W, Kirchhoff and Clemesha [1973]) and Urbana, Illinois, USA (40.2^{o}N, 88.2^{o}W, Richter et al. [1981]). These studies have observed and modeled the chemistry and dynamics of the sodium layer, including the seasonal variations, nighttime variations, daytime variations, and day-night transition of the sodium layer. The sodium layer has also been studied and modeled by many researchers to try to isolate the source of the sodium atoms (Allen [1970], Hunten and Wallace [1967],Donahue and Meier [1967], Narcisi [1968], Megie et al. [1977]), to study the removal of the sodium atoms from the layer (Hunten [1967], Richter and Sechrist [1979a], Hunten [1981], Kirchhoff [1983], Sze et al. [1982]) and to explain how these processes affect the chemistry of the mesosphere.

The effects of dynamic processes on the sodium layer have also been modeled (Chiu and Ching [1978], Shelton and Gardner [1981]). These models show that atmospheric gravity-wave effects are important in the analysis of the short-term variations of the sodium layer. The sodium layer, since it is affected by the gravity-wave perturbations, can be used as a tracer of wave activity in the mesospheric region (Megie and Blamont [1977]). This remote sensing technique can be used effectively to measure mesospheric waves, which would otherwise be difficult to measure. In situ experiments (except for rocket-based experiments, which last only a short time) are difficult due to the high altitude of the mesosphere, and satellite measurements are difficult due to the low altitude of the mesosphere. Thus, lidar and other remote sensing techniques such as meteor radar, are the only viable techniques to measure gravity-wave activity in the middle atmosphere region (Fritts et al. [1984]). The lidar technique is used to collect all the data in this study.

1.2 Overview of This Study

This study encompasses refinements and improvements on the University of Illinois lidar system, gathering lidar data, processing the data, analyzing the data, and modeling the sodium layer dynamics. Chapter 2 reviews the background theory needed for this study. This includes a survey of past lidar observations, models of the sodium layer, observation of gravity waves in the mesosphere (both from lidar and other remote sensing techniques), and a review of sodium-layer/gravity-wave models.

Chapter 3 describes the lidar system, including the laser system, computer system, and receiver system, as well as the enhancements made to the system to increase the resolution and improve the signal-to-noise ratio (SNR) of the data.

Chapter 4 describes the processing algorithms developed to analyze the data and to calculate layer parameters, such as width, height, and column abundance. The algorithms use signal-processing techniques to determine gravity-wave parameters and to determine the variability of the gravity waves that are observed. The processing steps used to analyze the data are also described.

Chapter 5 reviews gravity-wave theory and the one gravity-wave model of Chiu and Ching [1978] and Gardner and Shelton

[1985] and uses those models to calculate the layer sensitivity to gravity-wave wavelength. Two models are derived to consider more realistic atmospheric conditions, including a two-gravity-wave model and a wind-shear/gravity-wave model. These models are used to better understand the effects of gravity waves on the sodium layer and also can be used to determine the effects on any neutral atmospheric layer. In addition, a technique to derive gravity-wave wind velocity fields from lidar data is presented. These models assume that the gravity waves have discrete frequencies and wavelengths in order to model the atmosphere, in reality, the atmosphere is composed of a complex spectrum of gravity waves which have temporal variations.

Chapter 6 discusses the results of the data collected in the experiments, including seasonal and nocturnal variations of the width, height, and column abundance of the sodium layer. These results are then compared with the results of other studies. The analysis of gravity waves in the data are discussed including the estimation of the gravity wave parameters, and the variability of gravity waves in the data. The airborne lidar experiment performed with the University of Illinois lidar system is also discussed.

Finally, Chapter 7 presents the conclusions of this study and suggests possibilities for future research.

2.0 BACKGROUND THEORY

Laser radar (lidar) systems use a laser as a source of energy to remotely detect the state of the atmosphere or hydrosphere. Lidar systems typically are composed of a laser transmitter and optical receiver, usually a telescope. The operating characteristics of the system, such as wavelength of the laser, power of the laser, temporal and spatial resolution, etc., depend on the type of experiment being performed. A short review of lidar principles (specifically, sodium lidar) will be presented here; a good reference for general lidar principles is Measure [1984]. Following the review of lidar principles, Chapter 2 surveys the results of past sodium lidar research. This research includes investigations (using both observations and theoretical modeling) into the origins of the sodium layer, the seasonal and short-term variations of the layer, and gravity-wave observations. Chapter 2 also reviews gravity-wave observations made by other remote sensing techniques. These results are compared (in Chapter 6) with the gravity-wave observations made in this study. Finally, the gravity-wave/sodium-layer model of Gardner and Shelton [1985] is described. This model is expanded in Chapter 4 to include more realistic atmospheric conditions.

2.1 Lidar Fundamentals

The University of Illinois lidar system is a sodium lidar system which measures the density of neutral sodium atoms found in the mesosphere (80 km to 100 km above sea level). The system, which is fully described in Chapter 3, operates by tuning the dye laser to the D2 absorption line of sodium. The laser is fired vertically, and backscattered photons are collected by a receiver telescope. The returns are range-gated like conventional radar systems, with a vertical resolution of 150 meters per range bin. From these returns it is possible to calculate the density of sodium in these range bins.

2.1.1 The Lidar Equation, Including the Effects of Resonant Extinction in the Sodium Layer

The fundamental equation in lidar systems relates the returned photon signal counts to the density of the target at range z. This equation for a pulsed lidar system operating in the monostatic mode, where the backscatter is due to fluorescence (as in the sodium lidar system), was first derived by Measure [1977]. Simonich and Clemesha [1983] refined the lidar equation to include the resonant extinction effects of the laser pulse as it travels through the sodium layer. The lidar equation is derived assuming the alignment of the laser and telescope in a typical experiment is similar to the alignment shown in Figure 2.1. Ω_r, the solid angle of the receiver, is determined by the field-stop iris at the focus of the telescope and the diffraction

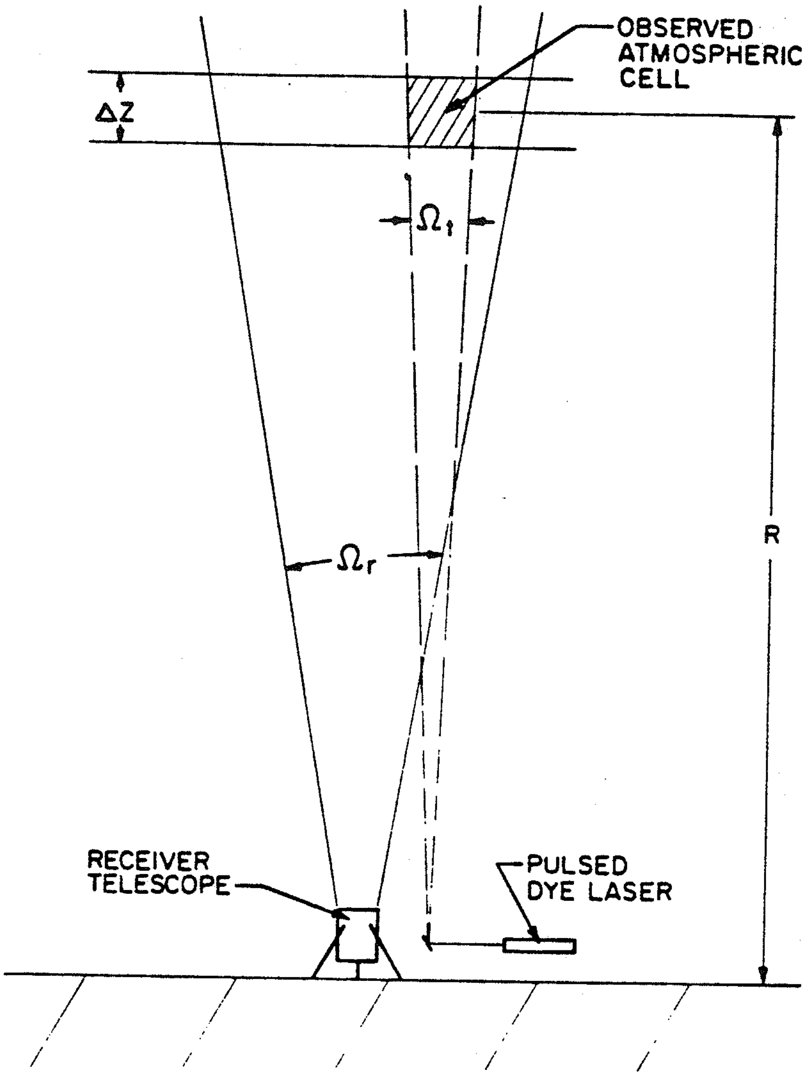

Figure 2.1 Monostatic lidar system, showing the field of view of the telescope and the divergence of the laser beam.

limit of the Fresnel objective lens. The value of Ω_r for the University of Illinois lidar system is approximately 3 mrad. Ω_t, the laser divergence angle, is approximately 1 mrad, thus $\Omega_r > \Omega_t$ which means that the entire scattering volume is illuminated by the laser pulse. With the University of Illinois lidar system, the lidar equation can be written

$$N_r(z_j) = \frac{N_t\ A_R\ T^2\ \eta\ n(z_j)\ \sigma_{eff}\ \Delta z\ C_j}{4\pi z_j^2} \qquad 2.1$$

where

$N_r(z_j)$ = the total number of photons collected in the j^{th} range bin,

N_t = the total number of photons emitted by the laser,

A_R = the receiver aperture,

T = the nonresonant atmospheric transmission,

η = the receiver efficiency,

$n(z_j)$ = the density of sodium in the j^{th} range bin,

σ_{eff} = the effective scattering cross section for sodium atoms,

Δz = the width of the range bin,

C_j = the correction term for the resonant extinction which is written

$$C_j = 1 - 2\,a_j \frac{\int_0^\infty L_0(\lambda)\ \sigma_{eff}^2(\lambda)\ d\lambda}{\int_0^\infty L_0(\lambda)\ \sigma_{eff}(\lambda)\ d\lambda} + 2a_j \frac{\int_0^\infty L_0(\lambda)\ \sigma_{eff}^3(\lambda)\ d\lambda}{\int_0^\infty L_0(\lambda)\ \sigma_{eff}(\lambda)\ d\lambda}$$

$$a_j = [\ n(z_j)/2 + \sum_{k=0}^{j-1} n_c(z_k)]\ \Delta z$$

$L_o\ (\lambda)$ = the number of photons transmitted per unit wavelength interval

$n_c(z_k)$ = the density corrected for resonant extinction

C_j is related to the line shape of the laser (the number of photons transmitted per unit wavelength), the resonant absorption cross section of the sodium layer, and the column abundance of the layer up to altitude z_j. The full description for C_j can be found in Simonich et al. [1983]. Equation 2.1 assumes negligible saturation effects; that is, the laser pulse will not cause a population inversion in the sodium atoms found in the sodium layer.

In practice, many parameters of the lidar equation are not known or not accurately known. A technique to normalize system-dependent parameters by using photon returns from low-altitude Rayleigh backscatter (about 30 to 40 km) has been implemented. The Rayleigh returns from low altitudes are independent of the wavelength of the laser light and can be written

$$N_{Ray}(z_r) = \frac{N_t\ A_R\ T_R^2\ \eta\ \Delta z\ \sigma_R(\pi)\ n_{Ray}}{4\pi\ z_r^2} \qquad 2.2$$

where

T_R = the atmospheric transmission to altitude z_r,
$\sigma_R(\pi)$ = the Rayleigh backscatter cross section,
N_{Ray} = the number of photocounts,
n_{Ray} = the average density of the atmosphere in range bin z_r.

Taking the ratio of the sodium density returns to Rayleigh density returns results in

$$n(z_j) = \frac{z_j^2\ N_r\ T_R^2\ \sigma_R(\pi)\ n_{Ray}}{z_r^2\ N_{Ray}\ T^2\ \sigma_{eff}\ C_j} \qquad 2.3$$

Furthermore, it can be shown that, in the region of the atmosphere from 30 to 90 km, $T_R = T$, that is, the transmission of laser light tuned to the D2 absorption wavelength is subject to only a small amount of absorption as it propagates from 30 to 90 km. This assumption leads to less than a 1% error in the calculation of sodium density. The effective scattering cross section of the sodium layer is related to the line width of the laser (for the University of Illinois system the line width is about 9 pm and the σ_{eff} is 1.84 X 10^{-16} m^2). The Rayleigh backscatter cross section can be calculated assuming the laser light is only weakly polarized and by using standard parameters for the atmosphere from CIRA [1972]. The calculations result in a value for σ_R=4.71 X 10^{-31} m^2.

The density of the atmosphere at the Rayleigh altitude can also be found in CIRA [1972] and at 40 km is equal to 8.0 X 10^{22} m^3. For these experiments, it was necessary to use an exponential fit of the data to calculate the photocounts due to Rayleigh backscatter in an altitude range of 35 to 40 km in order to accurately determine the density of the atmosphere. The altitude range 35 to 40 km was chosen to eliminate the effects due to the low-altitude blanking of the photomultiplier up to an altitude of 30 km.

Thus, for the lidar system used in these experiments, the density profiles of sodium, which vary with altitude, can be written in terms of received signal photocounts, Rayleigh photocounts and laser parameters as

$$n(z_j) = \frac{z_j^2 \, N_r \, \sigma_R(\pi) \, n_{Ray}}{z_r^2 \, N_{Ray} \, \sigma_{eff} \, C_j} \qquad 2.4$$

2.1.2 The Convolutional Form of the Lidar Equation

Another way to view the lidar data is to note that the photon counting rate at the receiver can be written (including background noise counts from ambient light and dark counts from the photomultiplier tube) as

$$N_r(z) = \frac{\eta A_R}{h\nu} \int_0^\infty d\sigma \int_0^\infty d\tau \; l(t-\tau)\, p(\tau-\sigma)\, \psi(\sigma) + x_b; \qquad t=2z/c \tag{2.5}$$

$$\psi(z) = \frac{n(z)\, \sigma_{eff}(\pi)}{z^2}\, e^{-2\int_0^z \alpha(s)\, ds}$$

where

x_b = the background noise counts,
$\alpha(z)$ = the atmospheric extinction coefficient,
c = the speed of light,
$\psi(z)$ = the scattering profile,
h = Plank's constant,
λ = the optical frequency of the laser light,
η = the overall system efficiency,
$l(t)$ = $\exp(-t/T_1)/T_1$, T_1 is the radiative lifetime of the scatterer.

If $\alpha(z)$ is negligible for altitudes greater then 30 km, and if the laser pulse and radiative lifetime of the scatter are short compared to the scattering profile, then Equation 2.5 can be simplified, and an expression similar to Equation 2.3 can be derived. More importantly (especially for signal processing considerations) Equation 2.4 can be written (if $l(t)$ and $\psi(t)$ are assumed zero for $t<0$) as a convolution of three terms:

$$n(z) = \frac{\eta A_R}{h\nu} l(t)*p(t)*\psi(t) \qquad 2.6$$

Note that there is some confusion in notation, since the pulse shape and radiative lifetime of sodium are both a function of time, and the photocount profile is a function of altitude. This can be resolved by observing that the laser pulse travels at the speed of light and that each altitude range bin refers to a specific time interval. This is shown in Figure 2.2 and is referred to as the space-time path of the laser pulse.

Equation 2.6 shows the effects of the laser pulse shape and radiative lifetime on the returned photocounts. The effect can be considered to be a low-pass filter on the data. Rowlett and Gardner [1979] investigated methods to deconvolve these effects out of the lidar data using Twomey estimators. Unfortunately, Rowlett found that the order of the filter used as the Twomey estimator has to be determined and that a large filter order is needed to ensure an unbiased estimate. Rowlett also found that classical low-pass filtering techniques could reduce the noise effects in the data. He also performed spectral analysis using periodograms to estimate the power spectrum.

Equation 2.4 indicates that the collected data can be modeled as signal returns with additive shot noise due to background illumination and dark counts produced by the photomultiplier tube (PMT). Typically, when processing data, the shot

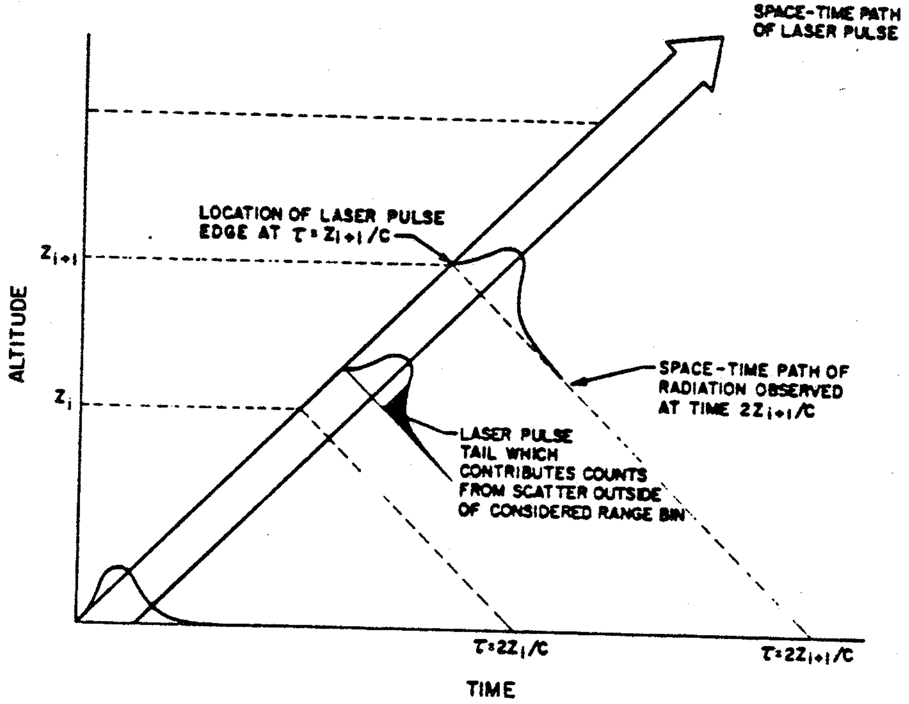

Figure 2.2 Space-time diagram of the propagating laser pulse (Richter [1978]).

noise level is found by averaging returns from the 60 to 70 km altitude range or altitude ranges above 110 km, since in these regions, the lidar system cannot detect Rayleigh scatter and sodium is not usually found. The returns are therefore an accurate measure of the system background noise level.

2.2 Past Sodium Layer Observations

The study of the sodium layer began with Slipher's [1929] discovery of radiation emissions at a wavelength of 589 nm in the nightglow spectrum. Since that time, many investigators have studied the origins and the behavior of the atomic sodium layer using a variety of atmospheric remote sensing techniques including lidar, sodium nightglow and sodium dayglow. Prior to 1970, the sodium layer was measured primarily by measuring the total flux of resonantly scattered sunlight. This measured only the total column abundance of sodium. Hunten and Wallace [1967] and Donahue and Meier [1967] used rocket experiments to measure the sodium density as a function of altitude and found the sodium was confined to a small region of the mesophere. Sodium lidar system, first introduced by Bowman [1969], are able to monitor the sodium layer over long periods of the day or night and produce data with the altitude resolution comparable to the resolution of rocket experiments. Appendix A reviews past work done by atmospheric sodium groups in the areas of seasonal variation of the sodium layer, short-term variations of the sodium layer, and gravity-wave activity in the sodium layer.

2.2.1 Origins of the Atomic Sodium Layer

The source of the sodium atoms in the 80 to 100 km range has been a controversial topic among researchers, whose theories suggested either a terrestrial or an extraterrestrial origin for sodium atoms. Allen [1970] suggested that the source of sodium was the salt in evaporating sea spray. Donahue and Meier [1967] and Hunten and Wallace [1967] independently suggested that sodium may be released from a layer of aerosol or dust particles. General agreement now is that the sodium layer is formed from sodium produced (at least partially) by the ablation of meteors as they enter the atmosphere (Junge et al., 1962). Gadsden [1968,1970] outlined this theory in a series of papers. The correlation of the enhancement of sodium (and other metallic ions) during meteor showers [Narcisi, 1968; Zbinden et al., 1975; Megie and Blamont, 1977] demonstrates that meteor influx has an important role as the source of atmospheric sodium. Megie et al. [1978] showed that the ratio of atmospheric sodium to atmospheric potassium varies seasonally by a factor of 4 to 5. They concluded that sodium is produced from a dual source of meteor ablation and vertical transport. Meteor ablation is assumed constant over the year, except during meteor showers. The vertical transport of sodium occurs only in winter at high latitudes when the circulation pattern of the polar stratosphere breaks down. As confirming evidence of their theory, they noted the small seasonal variation of sodium at low latitudes. Jegou et al.

[1984] in their more general model of the alkali metals in the atmosphere concluded that meteor showers have a small seasonal effect, but are the primary source of sodium in the layer.

The removal of sodium atoms from the layer has also been studied, and various chemical sink mechanisms have been suggested for the removal of sodium atoms from the sodium layer. Hunten [1967] suggested that the chemistry of the layer could be approximated at least to the first order by the reactions:

$$NaO + O \rightarrow Na + O_2 \qquad 2.7$$

$$Na + O_3 \rightarrow NaO + O_2. \qquad 2.8$$

Megie and Blamont [1977] proposed to include NaO_2 and NaH in their modeling reactions. Richter and Sechrist [1979a] proposed a model that added clustering of sodium ions to CO_2 and N_2 molecules as an intermediate stage in the hydration of sodium ions. Hunten [1981] proposed that clustering of dust particles and ionization of sodium atoms could act as a sodium sink. This model disagreed with the results of Clemesha et al. [1981a], who showed that the seasonal variation of the height of the layer at 23^{o} S latitude is much larger than Hunten's predicted value. Kirchhoff [1983] and Sze et al. [1982] included the reaction of NaOH as a sink of sodium to better model short-term (daily) changes in the sodium layer. Thus, the sources and sinks of atomic sodium have been and continue to be studied to better understand the chemistry of the mesospheric region.

2.2.2 Seasonal Variations of the Sodium Layer

A topic closely related to the production and loss of sodium in the mesospheric region is the seasonal variation of the column abundance, width, and height of the sodium layer. These parameters were first studied by Gibson and Sandford [1971] using the lidar system in Winkfield, England. They observed a large enhancement of sodium abundance in the winter months and a minimum of sodium abundance in the summer months. They also observed a lowering of the sodium layer in the winter months.

Further studies of the seasonal variation of the sodium layer were performed by Megie and Blamont [1977] in Haute-Provence, France. They also saw a similar peak of sodium column abundance in the winter, but no sharp minimum in the summer months. Megie and Blamont also calculated the height and width of the sodium layer by using a least-squares fit of the layer to a Gaussian shape. From the parameters derived from the least-squares fit, they observed a lowering of the sodium layer in the winter months, when the column abundance is at a maximum, and a rising of the layer in the summer, when the sodium abundance is at a minimum. They also observed no seasonal trend in their measurements of the width of the layer.

Simonich et al. [1979], Sao Paulo, Brazil, observed the seasonal variability of the sodium layer in the Southern Hemisphere. They also found that the sodium layer has a maximum column abundance in the winter (June-July) and a minimum column abundance in the summer (December-January) months. Their minimum in column abundance has a sharp peak, like that of Gibson and Sandford, but unlike the minimum of Megie and Blamont; thus, it appears that these results are conflicting. Since Megie and Blamont and Gibson and Sandford made measurements at approximately the same latitude, the difference in latitude cannot explain the difference in results. One possible explanation is that the data from all three groups spanned different years; thus, the seasonal variation of the sodium layer may have different characteristics from year to year.

The Simonich et al. group found no significant variation in the height or structure of the sodium layer. Simonich et al. did note a definite trend in the ratio of winter to summer column abundance and the variability with latitude. They showed that the ratio of column abundance for high latitudes was higher than the ratio for lower latitudes, and that the Northern and Southern Hemisphere were somewhat symmetric. Jegou et al. [1984] also modeled a meridional variation of the ratio of sodium layer column abundance in the winter to sodium column abundance in the summer. They noted a linear increase of the summer-to-winter ratio to 60° latitude then a slightly slower linear increase of the ratio in latitudes greater than 60° latitude. Unfortunately, not enough data are yet available to conclusively determine latitude effects on the column abundance of sodium or the global distribution of sodium.

The seasonal variability of the sodium layer was modeled by Fiocco and Visconti [1974], by assuming that the sodium in the atmosphere was caused by the sublimation of dust. The seasonal temperature change in the mesospheric region thus would control the sublimation rate, and by this mechanism, the seasonal variation of the column abundance of the sodium atoms can be shown to vary during the year. Since the origin of the sodium atoms is believed to be due mainly to meteoric influx, this theory has since been revised. Jegou et al. [1984] modeled the seasonal change by including the seasonal variability in the temperature and wind patterns. They reasoned that the lower the temperature (i.e., in summer) of the mesosphere, the more efficiently the sodium atoms would cluster to water molecules, thus reducing the column abundance. Also, the stronger the westerly wind (i.e., in winter) the higher the atomic sodium ion layers, thus causing less clustering of sodium ions and an increase in the column abundance. Swider [1985] noted that due to the inverse relationship between temperature and the loss rate for the three-body process for sodium, the loss rate will have variations much greater than the variations in pressure. He showed this effect can cause much greater seasonal variations in the rates of chemical processes then the seasonal variations of pressure at mesospheric heights and thus produce seasonal variations in the sodium abundance. Seasonal variation of sodium is one of the most fundamental features of the sodium layer and is still of current research interest, since the explanation of the winter enhancement is closely aligned to many other atmospheric seasonal changes.

2.2.3 Short-Term Variations of the Sodium Layer

Nocturnal variations in the sodium layer have been observed by all of the sodium lidar groups and are attributed to both chemical (sources, sinks, and rates of chemical reaction effects) and dynamical (gravity and tidal wave effects) changes in the atmosphere. The first study of nightly variations was performed by Sandford and Gibson [1970], Gibson and Sandford [1971]. They noted trends in the data that included a decrease in the column abundance during the night, until a minimum was reached at about midnight, and a steady increase in the column abundance until dawn. Further studies by Gibson and Sandford [1972] using a daytime lidar system showed little variation of atomic sodium density during the daytime and the day-to-night transition. Megie and Blamont [1977] also found systematic variations during each night of observation. They observed an increase in the topside scale height and a broadening of the layer. Also, they reported the effects that gravity waves have on data and concluded that dynamic processes in the mesosphere dominate the short-term variations.

Simonich et al. [1979] noted, in averaging their nighttime data (over 344 nights of data), a trend in the column abundance similar to Sandford and Gibson. They also noted an increase in scale height of the top side of the layer, an enhancement of sodium on the topside of the layer, and a depletion of sodium on the bottomside of the layer. This increased the height of the sodium layer and broadened it.

With the use of a daytime lidar system, Granier and Megie [1982] found no systematic variation of the sodium layer at sunset or sunrise or during the day or night. They also noted no direct influence of the solar diurnal cycle on seasonal or short-term effects. Clemesha et al. [1982] (Sao Paulo, Brazil) used a daytime lidar system to observe the 2,2 solar semidiurnal tide in the sodium density perturbations and found it to have an amplitude on the order of 30 cm/s at a height of 100 km, much higher than the value predicted by theory [Lindzen and Hong, 1974]. In a later paper, Batista et al. [1985]) traced tidal waves as they propagated through the sodium layer. By taking data continuously over a period of days, they were able to deduce the strong 12- and 24-hour tidal periods and showed that they agreed with tidal models (Forbes [1982a]). They also noted a lowering of the height of the layer at noon and a raising of the layer at midnight. Chemical modeling of the layer (Kirchhoff and Clemesha [1983] and Kirchhoff [1983]) predicted a depletion of sodium atoms at the bottom of the layer, about 80 km, during the nighttime hours, with a minimum at predawn and an enhancement during the daytime due to the inclusion of NaOH as a sink mechanism.

Another interesting phenomenon observed only by Clemesha et al. [1980], using a steerable lidar system, and Kirchhoff and Takahashi [1984], observing the nightglow of sodium, in Sao

Paulo, Brazil is the existence of sodium clouds. Sodium clouds are very large, short-lived enhancements of the observed sodium. These enhancements are too large to be caused by waves or other typical mesospheric activities. The observations of these sodium clouds by Kirchhoff and Takahashi have been correlated with meteor showers. Thus, it is hypothesized that the clouds are due to meteor ablation trails passing through the field of view of the lidar receiver. This substantiates the theory that the source of sodium is from the ablation of extraterrestrial meteors. Also, since these sodium clouds have been observed only at low latitudes (23°S), it implies that the global distribution of sodium differs with latitude.

2.2.4 Observations of Gravity Wave Features by Sodium Lidar Groups

As noted in the short-term variations, the existence of gravity-wave features (i.e., periodic sodium density variations in altitudes that propagate downward in time) have been observed by all lidar groups: Sandford and Gibson [1970]; Blamont et al. [1972]; Megie and Blamont [1977]; Simonich et al. [1979]; Juramy et al. [1981]; and Richter et al. [1981]. These studies used the sodium layer as an inert tracer of the dynamics of the mesospheric region. They also observed vertical wavelengths that vary from group to group: 11 km and 20 km for Simonich et al. [1979] and Clemesha et al. [1978a], 3 km to 15 km for Richter et al. [1981], and 8 km to 15 km for Chanin and Hauchecorne [1981].

Clemesha et al. [1981b] used a three-point scanning lidar system to determine the wind velocity of gravity waves in the mesosphere. They calculated an east-west vertical wind wavelength component of 10 km and a north-south vertical wind wavelength component of approximately 5 km. Chanin and Hauchecorne [1981] used a lidar system to measure Rayleigh returns from 30 to 80 km. They determined that atmospheric perturbations could be traced to both gravity and tidal waves. They also calculated temperature variations from the data and compared the wave-like structure in both parameters. Juramy et al. [1981] observed more wave activity in their high latitude measurements than in low latitude measurements.

Avery and Tetenbaum [1983] observed and compared the wave-like structures in their simultaneous measurements of sodium density by a lidar system and wind velocities by a meteor radar system. They concluded that the structures were due to gravity-wave perturbations on the order of a 10 km wavelength and could not be explained by the wind shear mechanism of Whitehead [1965], which was thought to produce similar results.

2.2.5 Observations of Gravity Waves by Other Remote Sensing Techniques

Gravity waves have been observed and studied by other atmospheric remote sensing techniques. These methods include observing wave motions in meteor trails, in chemical releases, in noctilucent cloud formations, temperature data from rocket-borne grenade experiments, radar tracking of balloon and rocket payloads, and ground-based radar and lidar experiments. A review and discussion of these techniques can be found in Fritts et al. [1984].

These studies of gravity waves have indicated that vertical wavelengths of gravity waves in the mesosphere vary from about 1 km to 10 km in the winter months (Philbrick et al.,[1983]) and from about 2 to 20 km in the summer months (Fritts, [1984]). Seasonal and latitudinal variations of gravity waves was first observed by Theon [1967]. He observed intense wave activity above 50 km in winter and above 70 km in summer.

A more complete study of seasonal and latitudinal variations of gravity waves is found in Hirota [1984]. This paper contains a statistical study of small scale disturbances in the stratosphere and mesosphere. Hirota's data were collected from rocket experiments in latitudes varying from 8° south to 77° north. Hirota observed that gravity waves in the 20 to 65 km region were isotropic (i.e., had no preferred direction). He also observed a maximum in gravity-wave activity in winter --twice as large as in the summer at high latitudes, but with smaller variation at lower latitudes. Also, as noted by a number of other authors (Witt [1962]; Grishin, [1967]; Haurwitz and Fogle [1969]; Carter and Balsley [1982]; Vincent and Reid [1983]; Balsley et al. [1983]; and Smith and Fritts [1983]), gravity waves have substantial temporal variation, which vary on time scales from a wave period to several days. Thus, with wave activity so variable (changing within a few wave periods), estimation of wave parameters is often difficult and inaccurate.

This wave variability can be traced to a number of causes, including gravity-wave saturation in the atmosphere, nonlinear wave-wave interaction, wave-mean flow interaction, and the variability of the sources of gravity waves. The main sources of gravity waves are considered to be mountain waves formed by flow over topographic features and waves produced by unstable wind shears. Other possible sources include geostrophic adjustment and frontal acceleration (Lindzen [1984]; and Einaudi et al. [1978/79]). Another characteristic of gravity waves is a variation with height of the gravity-wave frequency (Rastogi and Bowhill [1967]; Stening et al. [1978]; and Manson et al. [1979]). Such frequency changes are predicted by a quasi-linear theory of Coy [1983] and Fritts and Dunkerton [1984].

Photographic studies of noctilucent clouds, which appear at about 85 km in the summer months, have been used to estimate horizontal wavelengths of gravity waves ranging from 10 to 75 km with horizontal phase speeds of about 10 to 60 m/s (Witt [1962]; Grishin [1967]; and Haurwitz and Fogle [1969]). Similar studies of the perturbations of the OH emission layer by Herse et al. [1980] measured a horizontal wavelength of about 30 km to 100 km, and Armstrong [1982] measured a monochromatic wave with a horizontal wavelength of 244 km and a horizontal phase speed of 72 m/s.

Another characteristic of gravity waves is the "universal spectrum that appears in measurements of wind and temperature made in the mesosphere through the troposphere (Yeh and Liu [1985], Weinstock [1985], Dewan [1985], Scheffler and Liu, [1985], etc.). This Universal spectrum, similar to the Pierson-Moskowitz [1964] spectrum found in the ocean, shows that the spectral energy is related to frequency by a power law relationship ranging from 2.4 to 3.0 as power of the exponent. Unfortunately, due to the spatial distribution of sodium, the sodium layer acts as a spectral window on the data making measurements of the universal spectrum difficult on sodium lidar data.

2.3 Gravity-Wave/Sodium-Layer Dynamics

The response of the atmosphere to a gravity-wave phenomena has been observed using a variety of techniques. To compare the results of other techniques to the results of sodium lidar system, one must deconvolve the distorting effect of the sodium layer out of the returned data. The first study to realize the importance of layer effects on gravity-wave observations in a minor constituent layer in the atmosphere was Chiu and Ching [1978]. They showed that, since the gradient term was larger on the topside and bottomside of the layer, the background density perturbations were amplified by the gradient of the layer. Thus, the perturbation of the density of the layer is larger than the perturbations of the neutral atmosphere on the sides of the layer. Also, the amplification factor is larger on the bottomside of the layer than the topside of the layer. Chiu and Ching also noted that, due to the sign change of the gradient at the layer peak, the perturbations due to gravity waves had a 180° phase change above and below the peak of the layer. At the layer peak there was small amplification of the wave perturbations since the gradient approaches zero.

Gardner and Shelton [1985] derived a more exact solution by assuming a compressional and perturbation solution. They showed that near the peak of the layer, nonlinear terms dominate the solution. They also calculated the effects of the layer gradient on the power spectrum of the density perturbations. For a monochromatic wave, these effects produce a notch at the wavelength of the gravity wave and spectral peaks symmetrically on either side of the wavelength of the wave. Also, the 180° phase shift above and below the layer produces a temporal frequency component at the peak of the layer that is twice the value of the gravity wave's temporal frequency. Thus, these models of the sodium-layer/gravity-wave interactions aid in predicting the spectral signature of gravity waves in the lidar data as well as providing a tool to analyze the lidar data, and estimate the gravity-wave parameters and the variability of observed gravity waves.

3.0 LIDAR EQUIPMENT AND OPERATION

The University of Illinois sodium lidar system was originally developed in 1977 and has been continuously upgraded since that time. During this study, a number of modifications have improved the spatial and temporal resolution and the SNR of the data. The entire lidar system is outlined in this chapter, including the enhancements to the system.

3.1 Introduction

The lidar system of the University of Illinois consists of a tunable pumped dye laser, a computer controller and data logger, and a telescope receiver system. A block diagram of the system is shown in Figure 3.1. The operation of the system consists of tuning the laser to the D2 absorption line of sodium at 589 nm. The laser is coarse-tuned using a monochrometer, whose output is sampled with a photodiode array, and is fine-tuned using a hollow cathode tube and observing the opto-galvonic signal at its output. After each shot, the computer range-gates the returned signals collected at the receiver. The signal counts up to an altitude of about 50 km are due to scattering off molecules. The counts fall off exponentially with altitude. At about 80 to 100 km, the signal counts increase due to the resonant scattering off the free sodium atoms found in this region. Typically laser

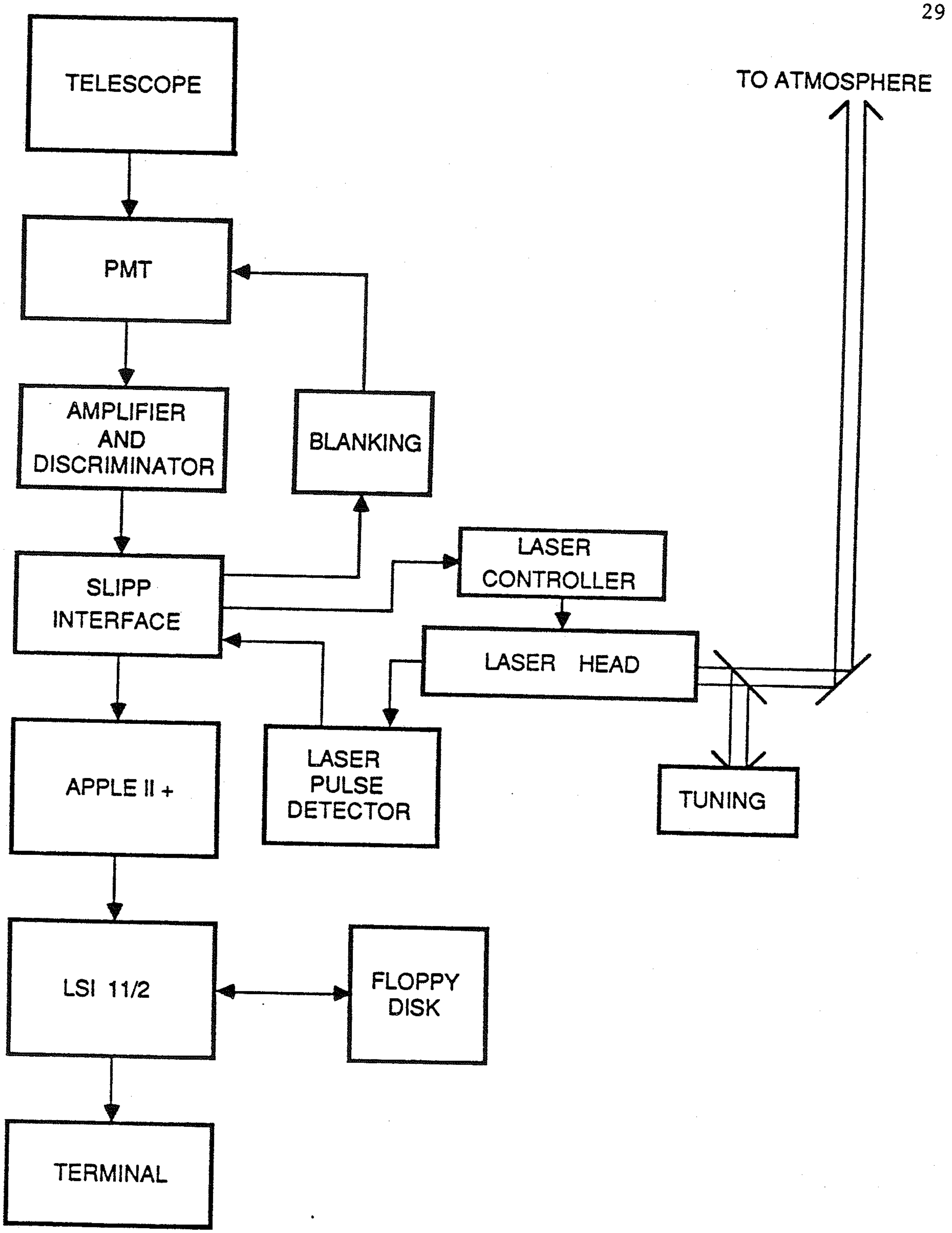

Figure 3.1 Block diagram of the lidar system.

pulses are integrated to reduce variance of the shot noise in the returned data. The result is one profile of raw data. The computer system has a real-time routine that plots the data after each profile. It also reports the signal counts, noise counts, and column abundance for each profile. The present system can collect a 250-shot profile in about one minute, firing the laser at 5 Hz. Later, these data are interpolated into ten minute intervals and normalized using the lidar equation to obtain sodium density profiles. The interval of ten minutes was found to be an optimal value. This choice trades temporal resolution for a lower variance of the shot noise and more condensed data. Once normalized and condensed, these profiles can be analyzed.

Experiments were conducted with this system at Wallops Island, Virginia; White Sands, New Mexico; and Urbana, Illinois. The same lidar system was used in all the experiments except for the telescopes. At the Urbana and White Sands sites, a 1.2 m Fresnel lens telescope (f1.56) was used with a field stop iris, 5 angstrom filter, collimating lens, and PMT. At Wallops Island, a 16-inch (f32.0) telescope was used with similar receiver optics.

3.2 The Laser System

The laser which is used to collect data at the University of Illinois lidar site is a Candella LFDL-1 flashlamp-pumped tunable dye laser. The dye used in the laser to produce the 589 nm wavelength light is rhodamine 6G perchlorate in a solution of methyl alcohol and water. The laser, whose specifications are given in Table 3.1 is composed of three parts: (1) the laser cavity (Figure 3.2), (2) the chiller unit (Figure 3.3), and (3) the high-voltage power supply and controller unit (Figure 3.4).

The laser cavity contains a front output mirror, a field stop iris to cut down on spatial modes of the laser, a housing containing the water-cooled flashlamp, and a dye cell. Also in the cavity is a beam expander with a magnification factor of four to avoid damaging the etalon filter and grating due to the intensity of the laser beam in the laser cavity. An etalon filter is used to narrow the line width of the laser to about ten picometer and has a free spectral range of approximately 0.5 angstroms. The etalon is tuned using a Burleigh inchworm, which is a piezoelectrically controlled micrometer. This enabled accurate tuning of the laser line during the fine-tuning procedure. The laser is tuned using an optical grading positioned at one end of the laser cavity (Figure 3.2). By tilting the grading, the output wavelength of the laser light could be adjusted.

The chiller unit has two main purposes. First, it pumps and refrigerates the water needed to cool the flashlamp, and second, it pumps the Rhodamine 6G Perchlorate dye-alcohol water mixture through the dye cell. Also, the dye mixture had nitrogen bubbled through it in the chiller unit to lengthen the lifetime of the dye. The dye was changed (typically after every 90,000 shots [about one night's data]) using the purge system connected

Table 3.1 University of Illinois Sodium Lidar System (40° 10' N, 88° 10' S)

<u>Laser</u>

Dye	Rhodamine 6G perchlorate
Wavelength	589.0 nm
Energy	50 mJ/pulse
Linewidth	10.2 pm
Pulsewidth	2 μs FWHM (300 m)
Repetition rate	5 Hz
Beam divergence	1 mrad

<u>Receiver</u>

Method	Photon counting
Objective	Fresnel lens
Area	1.2 m^2
Field of view	3 mrad
Bandwidth	5 angstrom
Receiver range bin size	150 m
Receiver efficiency	5%

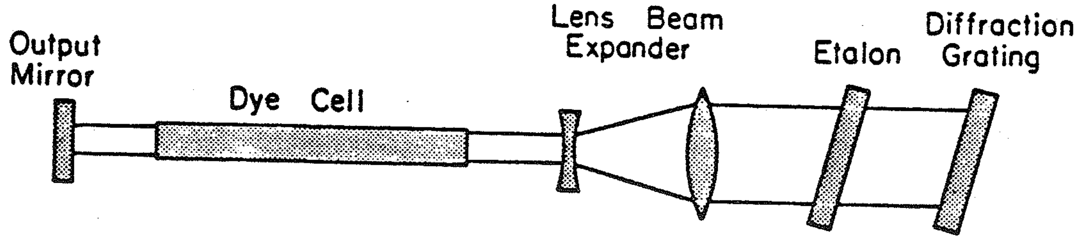

CANDELA DYE LASER CAVITY

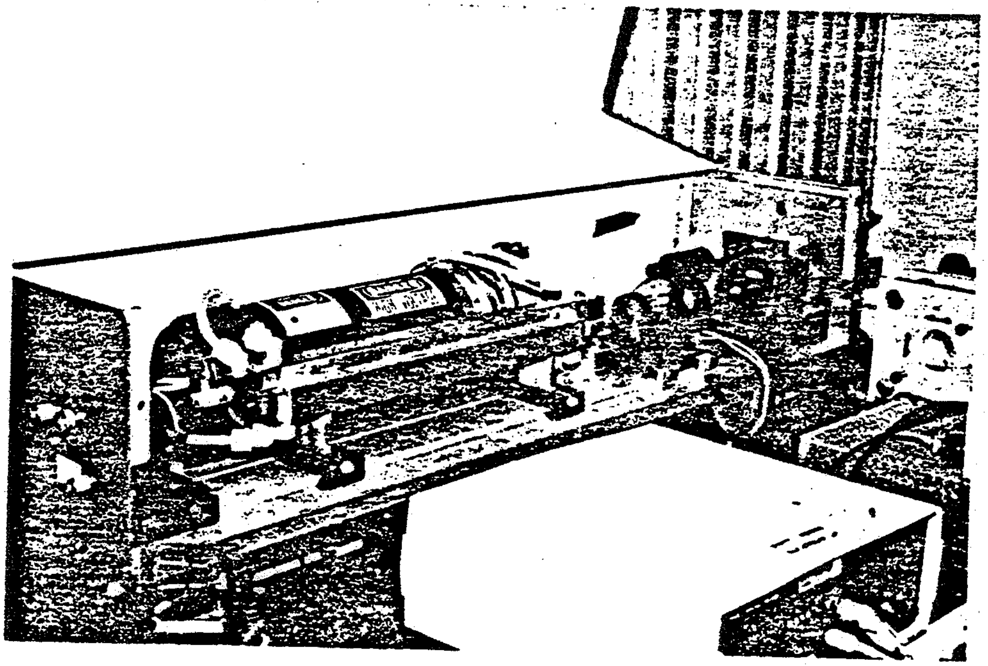

Figure 3.2 The University of Illinois Candela laser cavity.

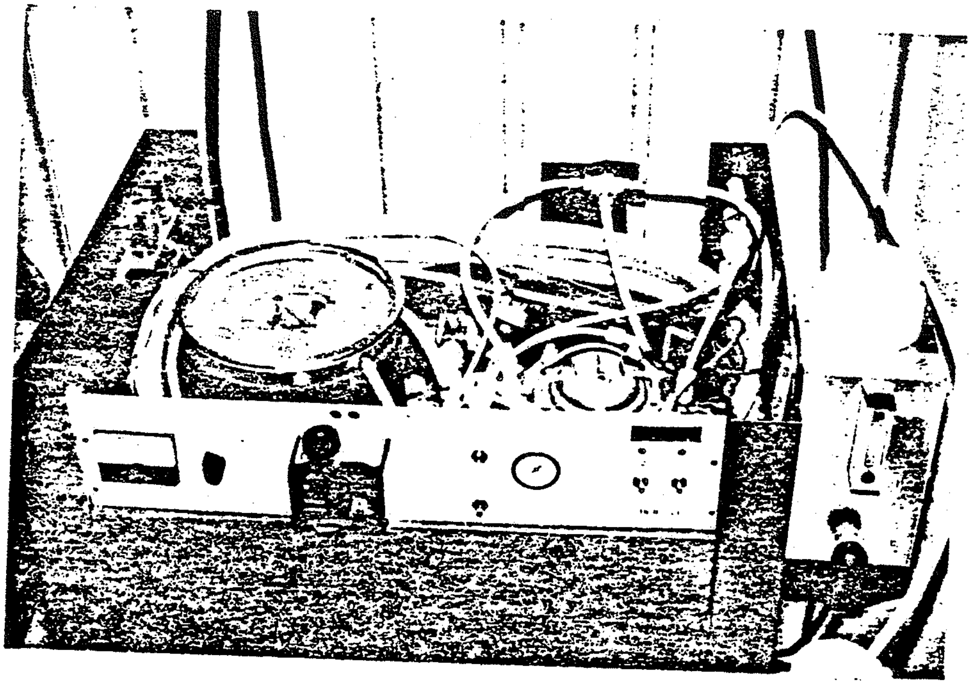

Figure 3.3 The University of Illinois Candela laser chiller unit.

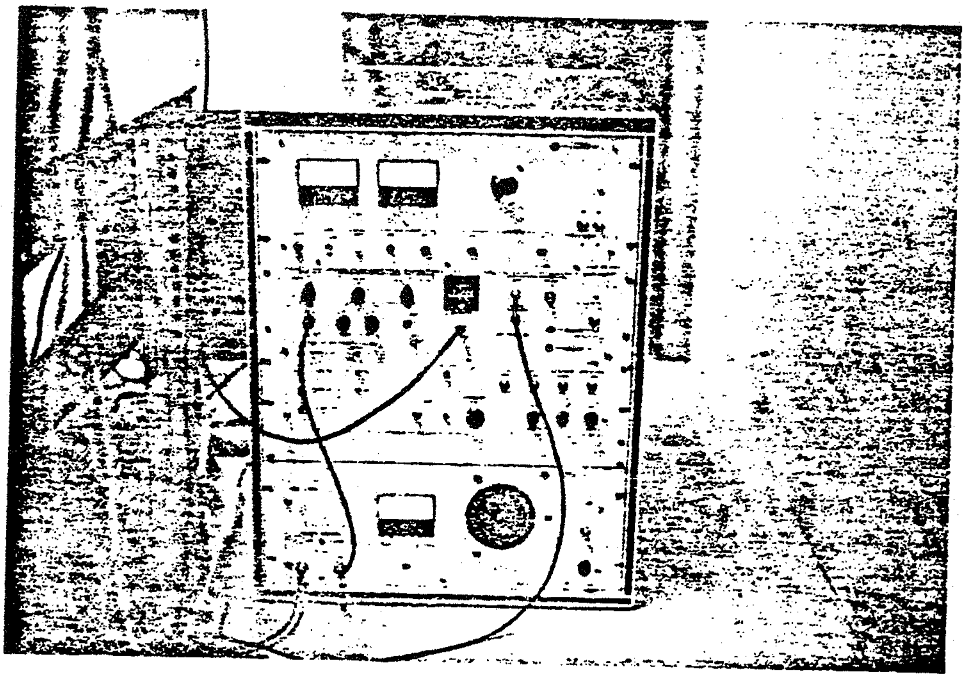

Figure 3.4 The University of Illinois Candela laser power supply.

to the dye reservoir.

The last part of the laser is the controller unit, which is composed of four separate sections: a high voltage power supply, a controller unit, a pump controller, and a simmer unit. The high-voltage power supply is used to charge the large (25 kV) capacitor in the laser cavity. This unit is also used to adjust the intensity of the output laser pulse; usually, a peak value of 50 mJ/pulse is used for data gathering.

The controller unit allows the laser trigger to be fired by either by the computer (externally) or by an internal variable-rate trigger. A manual option to fire only one shot can be used to burn in a new flashlamp.

The pump controller is connected to the chiller unit and the cavity to ensure proper operation of the pumps by means of flow gauges. This unit has a timing circuit that on power-up, delays firing of the laser for eight minutes until the filament in the flashlamp warms up.

Finally, the simmer unit keeps a simmer current in the flashlamp to prolong its lifetime.

Previous experiments using the lidar system (Richter and Sechrist [1978]; Rowlett and Gardner [1979]; and Shelton and Gardner [1981]) showed that one critical problem with the lidar system is keeping the laser tuned on the absorption line of sodium. Before 1982, the tuning system used an optical spectrometer and a sodium cell heated to 120°C. To use this system, researchers had to stop gathering data and use the laser output to try to fluoresce the sodium in the sodium cell. Since that time, a system using a Jerall-Ash monochrometer with a Reticon photodiode array (256 elements) on the output has been used. The photodiode puts out a signal that is proportional to the light intensity incident on the array, and the Reticon system displays the signal on an oscilloscope. Since the Reticon system sweeps across the diode array, the oscilloscope output is a digitized image of the spectrum of the laser pulse. This laser pulse and the output of the sodium reference lamp are combined using a Dolan-Jenner bifurcated fiber-optic cable. The laser pulse and reference sodium lamp output are then compared using the monochrometer. By adjusting the back grating, the laser line can be coarsely tuned to the 5890 angstrom line of sodium. Also, the Reticon outputs give information on the spectral structure of the laser pulse which is valuable while tuning.

After the laser is coarsely tuned, a finer tuning method is needed, because the photodiode array and monochrometer do not have enough resolution. To fine-tune the laser, a hollow cathode tube is used to produce an output signal that accurately detects the 5890-angstrom resonant lines of sodium. The hollow cathode tube has a cathode coated with sodium. When a 500 v dc bias is applied to the tube, a plasma is created between the anode and the cathode. Since the cathode is coated with sodium, when laser light of exactly the resonant wavelength of sodium hits the plasma, energy from the laser is absorbed by the plasma causing the stripping of electrons from the sodium atoms and an output pulse of approximately 50 mV is produced. This pulse, which can be viewed on an oscilloscope, is known as the Opto-Galvonic Effect (OGE) (Bridges [1978]; Keller and Zalewski [1980]) and can be used to tune the laser (Dovichi et al. [1982]). By using this system, the laser can be accurately tuned during data acquisition to the resonance line of sodium by adjusting the etalon filter with the Burleigh inchworm until the OGE signal is maximized.

3.3 The Receiver System

The receiver system (Figure 3.5) consists of a telescope that focuses the returned signal first to a folding mirror and then to a field-stop iris at the focal point of the telescope to limit the field of view of the telescope. The light is collimated by a Nikon 35 mm f/1.4 lens, then passed through a 5-angstrom interference filter, and finally focused onto a PMT. A complete description of the receiver setup can be found in Rowlett and Gardner [1979].

A number of problems arose in using the PMT. One major problem is that the PMT will overload due to strong signals from Rayleigh counts at low altitude. This causes distortion in the photon returns below 40 km and in the data calibration which relies on the data from 40 km. To solve this problem, the PMT is blanked up to an altitude of approximately 30 km. Blanking is accomplished by reducing the voltage on the first PMT dynode to that of the cathode or slightly negative [Shelton and Gardner,

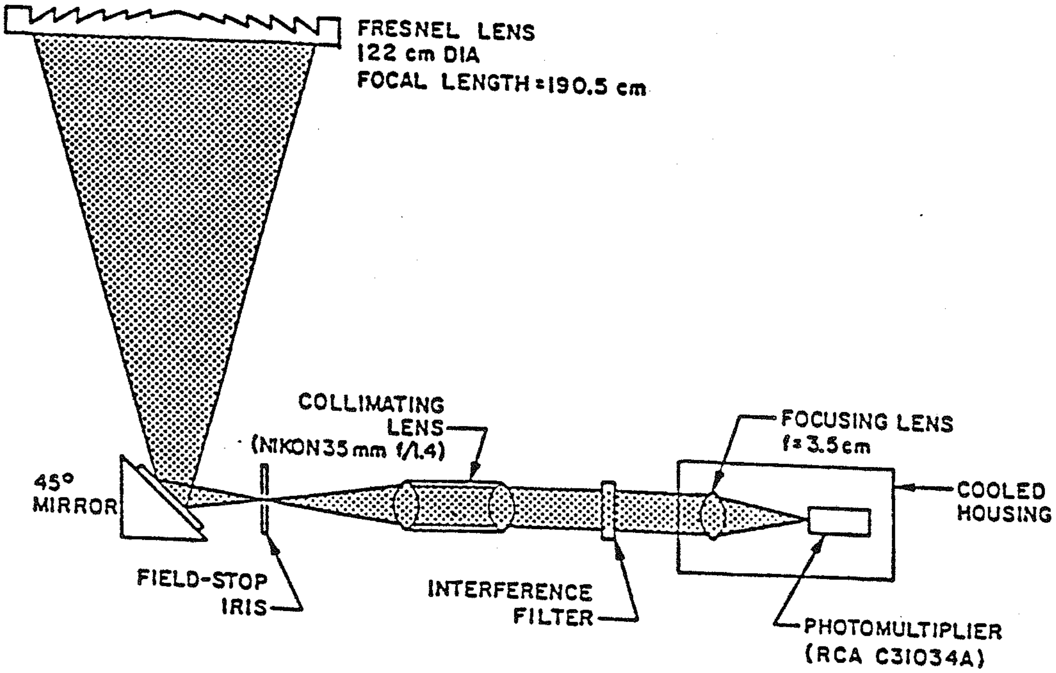

(a)

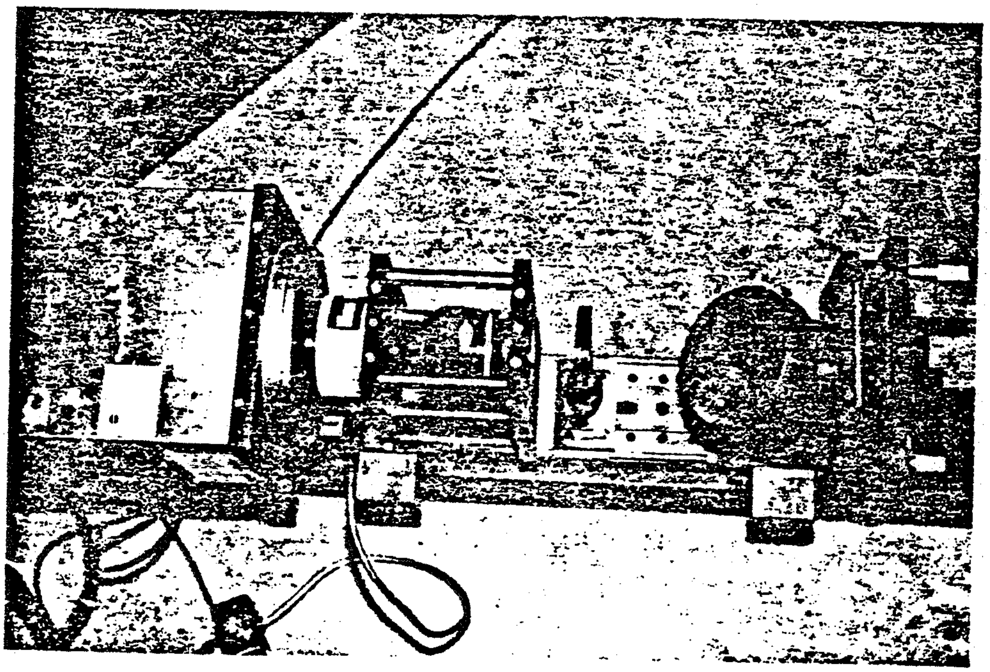

(b)

Figure 3.5 The receiver system for the lidar system. (a) diagrams the receiver set-up and (b) is a picture of the optics and the PMT.

1981]. This reduces the gain of the PMT by three orders of magnitude. After the blanking is switched off, the PMT recovers in about 6 to 10 μs. Thus, the data at an altitude of 40 km is unaffected and can be used to normalize changes in laser power in calculating sodium concentration.

The interference filters used at the output of the telescope were calibrated in a laboratory experiment. A sodium lamp was used as a light source, and the light was focused through the collimating lens and the filter. A power meter was then used to measure the intensity of the light passed through the filter on the wavelength of the sodium D2 line. The filter characteristics were photographed by passing white light through the filter and passing the output of the filter through the Jerall-Ash monochrometer. The output of the monochrometer was sampled with a Reticon array, and the intensity of the output was displayed on an oscilloscope.

3.4 <u>The Computer System</u>

The University of Illinois computer system used to collect lidar data consists of an LSI 11-02 computer, an Apple computer, and a photon-counter/system-interface (Voelz and Sechrist [1983]). The data collection process is controlled by the LSI 11 and enables the user to change the parameters of the experiment, such as the number of profiles per set, the number of range bins (up to 2000 bins), the laser repetition rate, the number of laser shots per profile, and the base altitude. The bin size is fixed at 150 m, which is the vertical resolution of the lidar system firing at zenith.

After the parameters of the experiment have been set up, the LSI 11 communicates, over a serial data link to the Apple computer, the number of laser shots and the repetition rate to fire the laser. The Apple acts as a slave computer whose task is to control the laser firing and keep a running log of the returns until all the laser shots have been completed. The Apple is connected via a Direct Memory access (DMA) link to the Sodium LIdar Pre-Process (SLIPP) box, which counts the photon returns from the PMT.

The SLIPP has two sets of counters, and after the laser is triggered by the Apple computer, the SLIPP waits for the laser control pulse (LCP), which is sent when a photodiode detects the light in the laser cavity due to the laser firing. After the LCP is received, the SLIPP reads continuously for 1 s and toggles the returns from the PMT between the two counters to determine the number of photons received in each range bin. These returns are stored in RAM in the Apple computer. If the LCP is not received, the Apple computer jumps to an error routine and informs the user of the failure.

After the profile is completed, the Apple transfers the data using a serial connection to the LSI 11. The LSI 11 plots the received data using an averaging window filter, stores the raw data on floppy disc for later analysis, and calculates the number of signal counts per shot and column abundance. By using both computers, the Apple computer is able to start taking the next profile while the LSI 11 is processing the data in real time, thus achieving a parallel collection and processing system.

4.0 SIGNAL PROCESSING AND DATA ANALYSIS TECHNIQUES

Sodium lidar data were collected with the University of Illinois lidar system on about 20 nights during this study. To analyze the data, a flexible software system was developed to filter the data, calculate gravity-wave parameters in the data, calculate the width, height, and column abundance variations of the sodium layer, and plot the data.

This computer program also simulated lidar data using the models derived in Chapter 5. The simulated data were processed in a similar fashion and then compared to the real data. Also, the simulated data was used to verify that the signal processing and data analysis programs were operating correctly. Chapter 4 outlines the techniques developed to process sodium lidar data and reviews the processing steps used in the data analysis.

4.1 Preprocessing of the Data

To process the data, it is necessary to combine the data into equally spaced temporal intervals. This is done to simplify the data processing and to increase the SNR of the data.

A simple interpolation scheme is used to place the data in equally spaced intervals. The profile in the interval $((m-1)T,mT)$ is simply the average of the normalized (by the lidar equation to density of sodium atoms) raw data collected by the system during this interval. If no data were collected during the interval, then the profile was interpolated by averaging the profile collected just before the current time interval and the profile collected just after the current interval. If more than one profile was missed, then a linear interpolator is used between the two profiles at the beginning and end of the missing section of data. The effects of this registration scheme on the data are: (1) The shot noise corruption of the registered profiles is reduced by a factor equal to the reciprocal of the square of the number of raw data profiles in the time interval. Thus, the integration to larger time intervals reduces noise in the data. (2) Since the data was simply averaged and not windowed, the high sidelobes of the averaging filter caused distortion in the data. Because of the preprocessing computational load, these effects are considered acceptable. (3) This technique trades off temporal resolution of the density profiles for lower white noise levels. Interpolation produces equally spaced density profiles, which are more easily analyzed using Fourier analysis and temporal plotting.

The interpolated profiles are sensitive to noise in either of the two end profiles which are used for interpolating. Thus, care must be taken not to interpolate between noisy profiles, especially when more then one profile is interpolated.

Next, the data are digitally filtered in both the temporal and spatial frequency domains. To reduce the effects of leakage signal power produced by the low-pass filtering of the data, a separable two-dimensional FIR Hamming window filter was used. The filtering process can be written:

$$n(z,t) = n(z,t) * h_{LPS}(z) * h_{LPT}(t) \qquad 4.1$$

where
h_{LPS} = the impulse response of the spatial filter
h_{LPT} = the impulse response of the temporal filter

h_{LPS} and h_{LPT} can be written in the frequency domain as:

$$H_{LPS}(\kappa_z) = 0.54 - 0.46 \cos\left(\frac{2\pi\ \kappa_z}{2\ \kappa_{z\text{-cut}}}\right) \qquad 4.2$$

$$H_{LPT}(\omega) = 0.54 - 0.46 \cos\left(\frac{2\pi\omega}{2\omega_{cut}}\right) \qquad 4.3$$

Where
H_{LPS} = the low pass spatial frequency response,
H_{LPT} = the low pass temporal frequency response,
$\kappa_{z\text{-cut}}$ = the 3 dB cut-off frequency of κ_z,
ω_{cut} = the 3 dB cut-off frequency of ω.

Since this is a two-dimensional filter it can also be analyzed in the w ω-k_z space as an ellipsoidal filter. The two-dimensional filter response can be written

$$H_{LP}(\kappa_z,\omega) = 0.29 - 0.25 \cos\left(\frac{2\pi\kappa_z}{2\kappa_{z\text{-cut}}}\right) - 0.25 \cos\left(\frac{2\pi\omega}{2\omega_{cut}}\right) + 0.21 \cos\left(\frac{2\pi\kappa_z}{2\kappa_{z\text{-cut}}}\right) \cos\left(\frac{2\pi\omega}{2\omega_{cut}}\right) \qquad 4.4$$

The response is plotted in Figure 4.1. This filter minimizes the

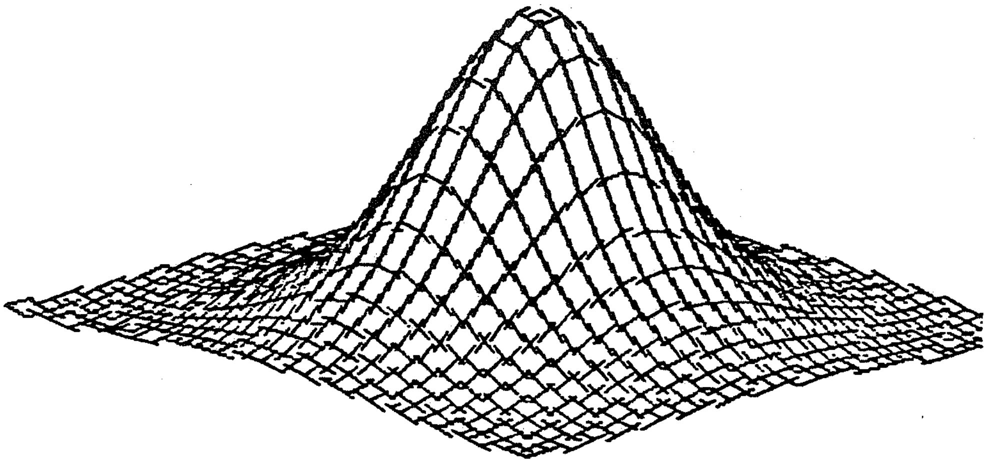

Figure 4.1 Two-dimensional frequency response of the two-dimensional Hamming window filter used in preprocessing the lidar data.

size of the first sidelobe (to -41 dB as compared to -13 dB for the rectangular filter) in the time domain and thus reduces the leakage effect of the filter which often resulted in "ringing" of the digital filter. Common filter cut-off frequencies used to filter the data spatially produced oscillations close to the wavelengths of gravity waves observed in the lidar data. Thus, using a Hamming window minimizes the "ringing" of the filter in the data.

This two-dimensional Hamming window filter was used in the preprocessing of all the data. The low-pass cut-off frequency of the filter was chosen by examining the power spectra. The periodogram was used to estimate the power spectrum of the signal. The mean of the spatial periodogram is given by

$$\begin{aligned} E[\phi_{\hat{n}}(\kappa_z,t)] &= \left(\frac{h\nu}{\eta A_R J \sigma_{eff}(\pi)}\right)^2 \sum_{i=1}^{M} (i\Delta z)^4 \, E[x(i\Delta z)] + |\phi_n|^2 \qquad 4.5 \\ &\approx \frac{C_s^2}{N_{tot}} + |\phi_n|^2 \end{aligned}$$

where

h = Planck's constant (6.63×10^{-34} J s),

ν = the optical frequency,

η = the overall system efficiency,

A_R = the receiver aperture area,

J = the laser pulse energy,

σ_{eff} = the effective sodium backscatter cross section,

κ_z = the spatial transform variable,

N_{tot} = the total number of signal photons collected in a profile,

C_s = the column abundance of the sodium layer,

ϕ_n = the actual power spectrum, and

$\phi_{\hat{n}}$ = the periodogram estimate of the power spectrum.

The spatial periodogram is a biased estimate of the sodium density power spectrum. The bias is related to the total photocount and the sodium abundance. In practice, it is most convenient to work with the normalized periodogram:

$$\frac{E[\phi_n(\kappa_z,t_0)}{E[\phi_n(0,t_0)} = \frac{|\phi(\kappa_z,t_0)|^2}{|\phi(0,t_0)|^2} + \frac{1}{N_{tot}} \qquad 4.6$$

The normalized periodogram has a maximum value of 1 at $\kappa_z = 0$. At high frequencies, where $\phi_n(\kappa_z)$ falls to zero, shot noise of the lidar system dominates the periodogram and establishes a noise floor at the level $1/N_{tot}$. This effect was observed in all the data collected in these lidar experiments (Figure 4.2).

A similar effect is observed in the temporal power spectral estimate. Here the perturbations about the average density at a particular altitude are used to estimate the temporal power spectrum of the data. Again, at higher frequencies the signal spectral power falls below the spectral power of the system shot noise floor (Figure 4.3). By using the periodogram as an estimate of the temporal and spatial power spectra, the temporal and spatial frequencies at which the spectral power of the signal falls below the spectral power of the shot noise can be determined. These frequencies can then be used as the cut-off frequencies of the two-dimensional Hamming window filter. Thus, with cut-off frequencies where the signal is lost in the noise,

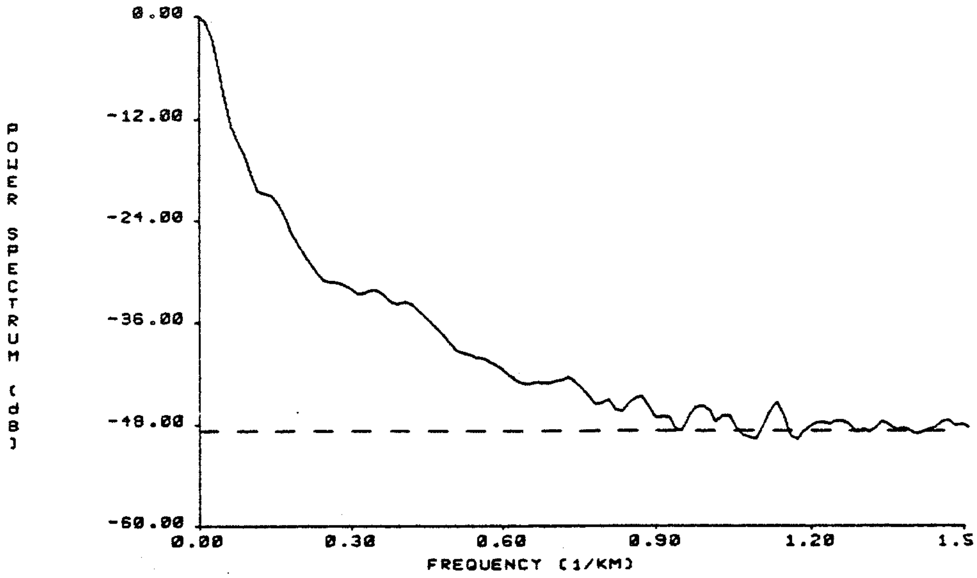

Figure 4.2 Periodogram estimate of the spatial power spectrum for the data collected from 20:20 CST on July 17, 1984, to 3:40 CST on July 18, 1984. The dashed line represents the background shot noise level. The signal drops into the shot noise level at a spatial frequency of 1.0 km^{-1}. These data were integrated over 79,000 laser shots.

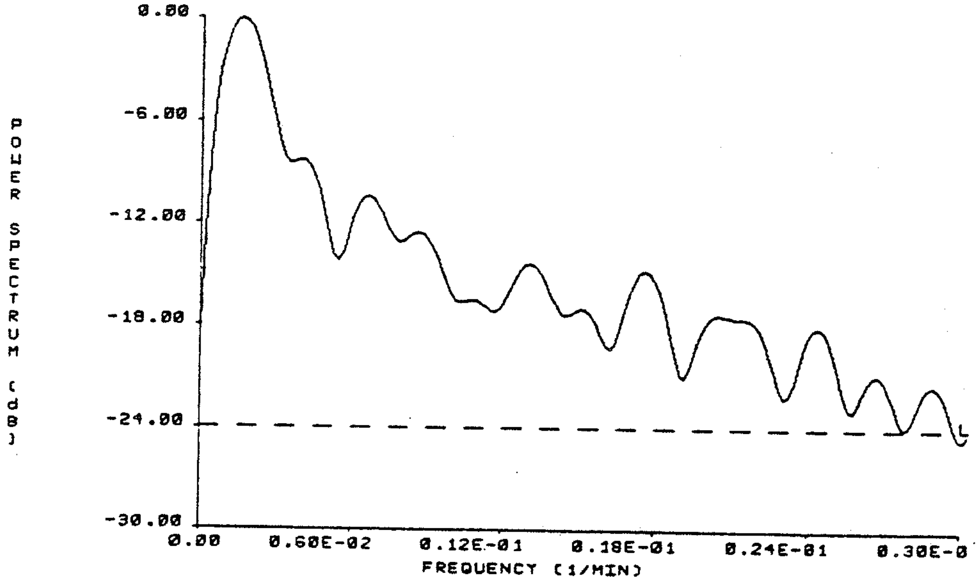

Figure 4.3 Periodogram estimate of the temporal power spectrum for the data collected from 20:20 CST on July 17, 1984, to 3:40 CST on July 18, 1984. The dashed line represents the background shot noise level. The signal drops into the shot noise level at a temporal frequency of 0.03 min^{-1}. These data were integrated over 79,000 laser shots.

one reduces the effects of high-frequency shot noise without reducing the low-frequency signal.

4.2 Layer Parameters

The width, height, and column abundance of the sodium layer are of interest in analyzing the dynamics and chemistry of the sodium layer. As noted in Chapter 2, the seasonal variations of these parameters have been studied. In this study, the column abundance, C_s, height, Z_s, and width, σ_s, are defined using the following formulas for the moments of the layer:

$$m_i = \sum_k (k\Delta z)^i \, n(k\Delta z, t_0) \qquad 4.7$$

$$C_s = m_0 \qquad 4.8$$

$$Z_s = \frac{m_1}{m_0} \qquad 4.9$$

$$\sigma_s = \left(\frac{m_2}{m_1} - \left(\frac{m_1}{m_0}\right)^2 \right)^{\frac{1}{2}} \qquad 4.10$$

These parameters are calculated and plotted by the main processing routine.

The width, height and column abundance are computationally simple to measure from the data and can be compared with the other lidar groups. Also, since these values are calculated from all the range bins, the effects of the shot noise are reduced by the integration procedure. A plot of these parameters (Figure 4.4) demonstrates their usefulness in determining both chemical and dynamical effects in the data. These measures are used in Chapter 6 to quantify the sodium layer variations.

4.3 Estimation of Gravity-Wave Parameters

As noted in Chapter 2, gravity waves have been observed and studied by numerous remote sensing techniques. In this section, both classical periodogram analysis and a new correlation technique are used to determine the wavelength, frequency, amplitude, and vertical phase velocity of gravity waves.

The gravity-wave parameters determined from estimates of the power spectrum through periodogram analysis are typically inaccurate due to various effects, both in the estimate and in the nature of the sodium-layer/gravity-wave interaction. Thus, the spatial correlation technique, which correlates successive spatial profiles and normalizes out the layer effects, is introduced to accurately calculate the wavelength and vertical phase velocity of the gravity wave. A dual technique using correlation of successive temporal profiles to calculate the period and vertical phase velocity is also introduced. These techniques, which can be summarized by

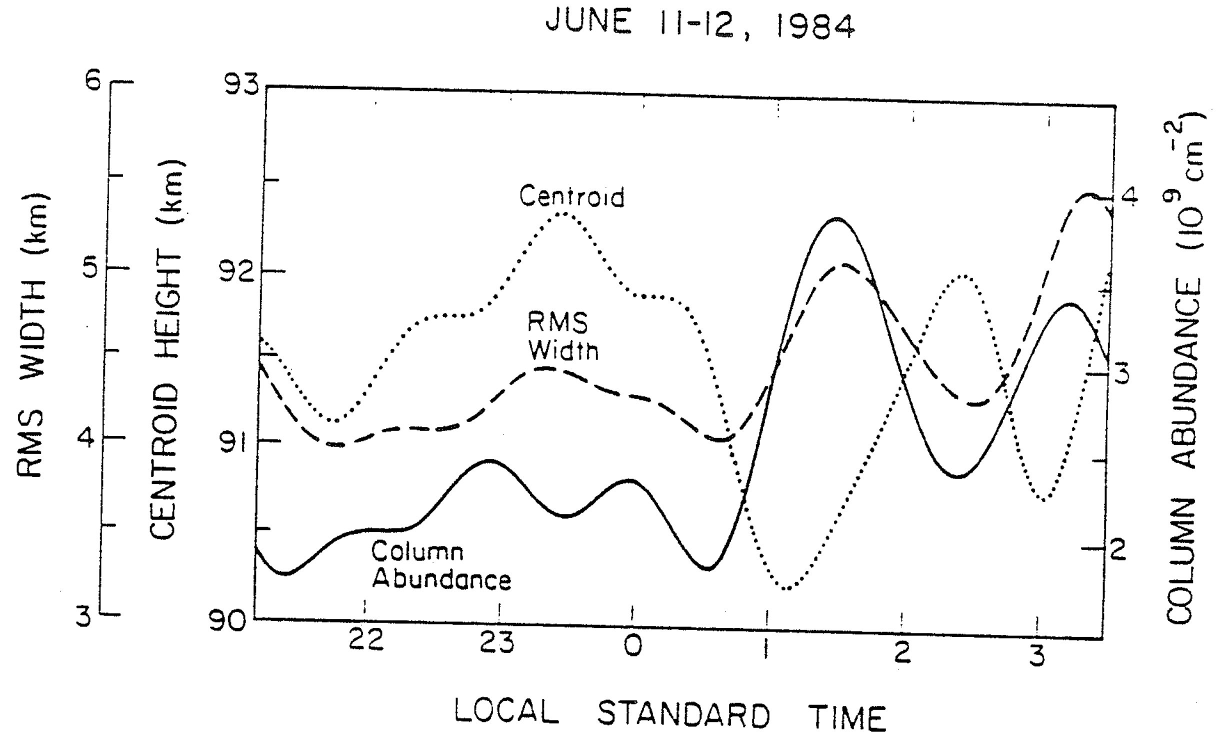

Figure 4.4 Column abundance, centroid, and RMS width of the mesospheric sodium layer collected at the Urbana lidar site from 21:10 CST on June 11, 1984, to 3:20 on June 12, 1984. The data were filtered with a spatial cutoff frequency of 0.5 km^{-1} and a temporal cutoff of 0.03 min^{-1}.

Technique	Gravity Wave Parameters
Spatial Periodogram	Vertical Wavelength and Amplitude
Temporal Periodogram	Period
Spatial Correlation	Vertical Wavelength and Vertical Phase Velocity
Temporal Correlation	Period and Vertical Phase Velocity,

are then compared with simulated and actual data. Wind velocity fields of gravity waves can be calculated by combining the parameters found by these techniques with the model of the gravity wave wind velocities in the atmosphere (Equation 5.22).

4.3.1 Periodogram Estimation of Gravity Wave Parameters

One method to estimate the power spectrum of the perturbations in the data is to use the periodogram. A complete development of the periodogram analysis can be found in Oppenheim and Schafer [1975]. They showed that the periodogram, which is defined by

$$I_n(k_z,t_0) = \frac{1}{N} \sum_{i=0}^{N-1} \sum_{m=0}^{N-1} n(i\Delta z)\, n(m\Delta z)\, e^{jik_z}\, e^{-jmk_z} \qquad 4.11$$

has a mean

$$E[I_n(\kappa_z,t_0)] = \sum_{m=-(N-1)}^{N-1} \left(\frac{N-|m|}{N}\right) \phi_n(m\Delta z,t_0)\, e^{-jk_z m} \qquad 4.12$$

In general, the periodogram is an inconsistent estimate (i.e., both the bias and the variance of the estimate do not approach zero as the sample length increases) of the power spectrum and can be expected to fluctuate wildly about the true power spectrum. Thus, it was found that the periodogram required windowed averaging to produce a consistent estimate of the power spectrum. In this application, Bartlett's procedure (found in Oppenheim and Schafer [1975]) of averaging the periodograms over many spatial profiles for the spatial power spectrum and over many temporal profiles for the temporal power spectrum was used to produce consistent power spectrum estimates.

To identify gravity waves in the periodograms of the data, it is necessary to identify the signature of the gravity wave in the Fourier domain. The spatial power spectrum has a spectral signature due to gravity waves (as noted in the model developed in Chapter 5). The gravity wave produces a notch at the wavelength of the wave and two spectral peaks symmetrically about the notch. Thus, to estimate the wavelength of the wave, one must estimate the position of the notch, and to estimate the amplitude of the gravity wave, one must estimate the value of the power spectrum at the notch or spectral peak. Since the notch is more sensitive to distortion due to filtering, the relative spectral peaks are used to determine the amplitude of the wave. Originally, the amplitude of the wave for a specified spectral peak value was determined numerically from the gravity-wave/sodium-layer models, but an analytic formula has since been derived (Voelz [1985]) and can be written

$$A^2 = \frac{|\phi(\kappa_{zp})|^2}{|\phi(0)|^2} \frac{(2(\gamma-1)\sigma_1)^2}{(\gamma H)^2} e^{(-z_s/H - \sigma_1^2/(2H)^2 - (1/\gamma H - 1/2H)^2 \sigma_1^2 + 1)} \qquad 4.13$$

Thus, by measuring the wavelength at the notch and the relative spectral peak value, the wave parameters can be estimated. Plots of the spatial power spectrum for the one gravity wave model (Shelton and Gardner [1981]) for various amplitudes and wavelengths are shown in Figure 4.5. The results show that, for lower spatial frequency waves, the layer shape corrupts the estimate of the wavelength and amplitude. Also, since no clear notch is present in the data, exact wavelength measurements are impossible. Figure 4.6 shows data collected on March 8, 1984, and its associated periodogram estimate of the power spectrum. This plot, which shows clearly the signature of gravity waves in the periodogram, is the best example of gravity wave signatures collected in this study; typically, less distinct signatures of gravity waves are present. One hypothesis for the changing signatures is gravity-wave variability, which is discussed in Section 4.5.

The periodogram method gives a good indication of how dominant a gravity wave is in the data, but does not accurately estimate the wavelength of the gravity wave. This is due to (1) the distortion of the layer and the inaccuracy of the periodogram estimate, (2) the effects of the shot noise background level on

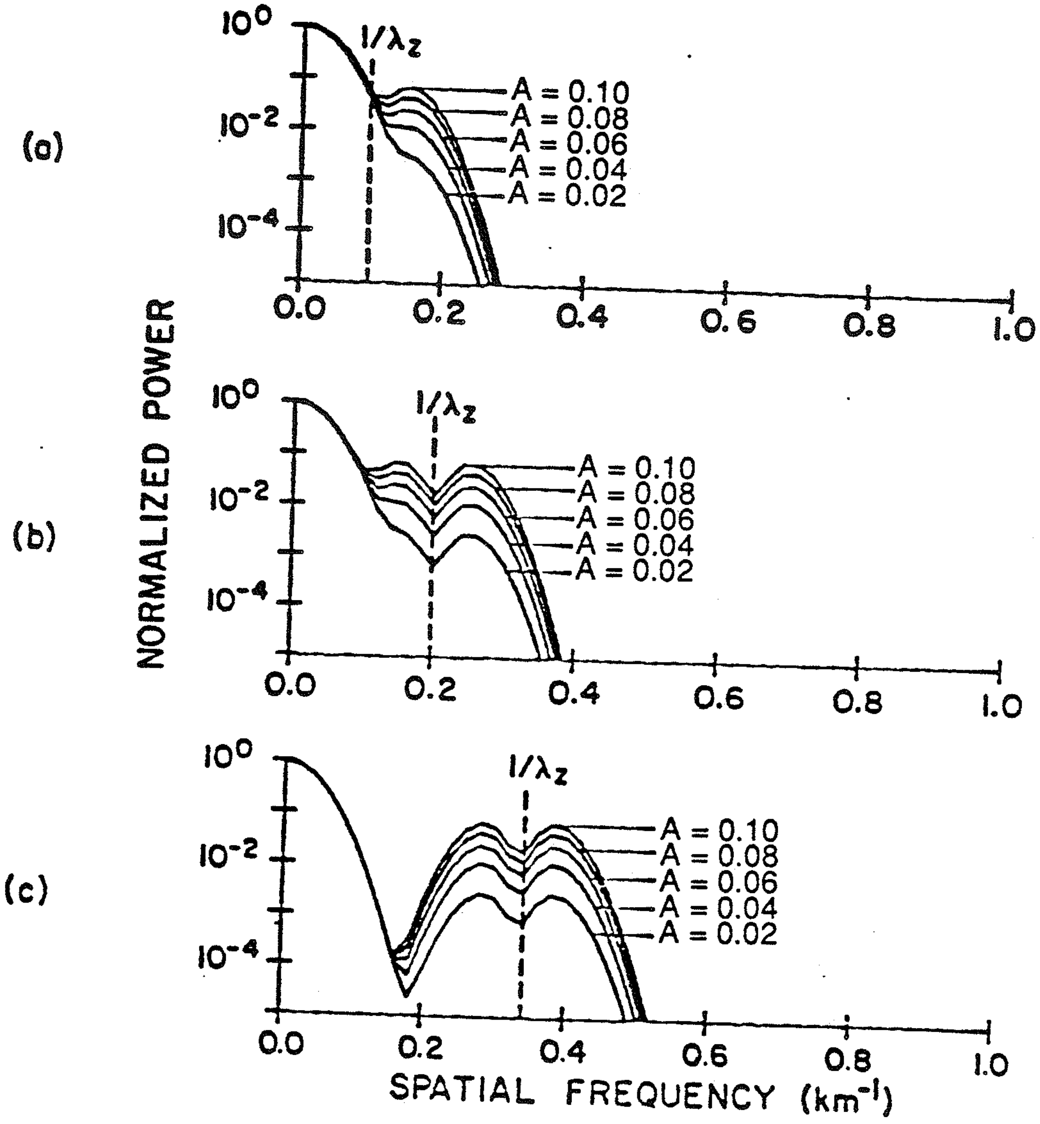

Figure 4.5 Simulated average spatial power spectra resulting from the linear density response to a gravity wave perturbation. The wave amplitude is given by A; the vertical wavelength of the gravity waves are (a) 10 km, (b) 5 km, and (c) 3 km. The width of the layer was 3 km and the mean height was 90 km. (corrected version of Shelton and Gardner [1981]).

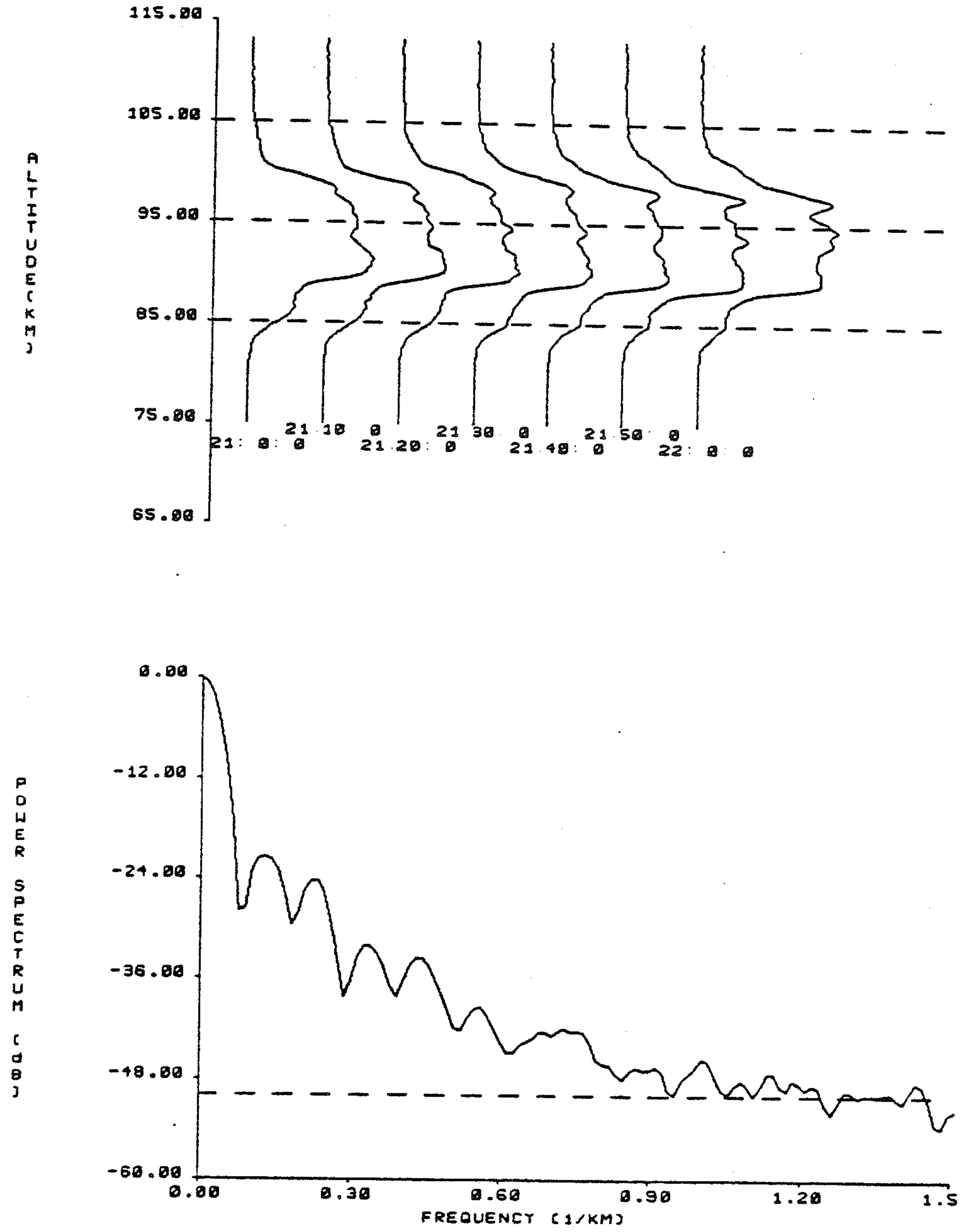

Figure 4.6 Data collected at the University of Illinois lidar site on March 8, 1984, from 21:00 to 22:00. The data were spatially filtered at 1 km^{-1}, and each profile is integrated over 2800 laser shots. The times of each profile in (a) is marked below the profile. (b) Periodogram estimate of the power spectrum.

the signature (this is especially true for low-amplitude waves), (3) the effects of averaging many profiles together to produce a good estimate of the power spectrum (if the wavelength is nonstationary, then the signature will effectively average out), and (4) the distortion effects due to multiple gravity waves or a continuous spectrum of energy due to other dynamical or chemical effects.

The temporal periodogram can be used to estimate the temporal power spectrum of the sodium density profiles. The temporal power spectrum is estimated by averaging the temporal periodogram (Bartlett's procedure) over an altitude range. The estimate of the temporal power spectrum of the March 8, 1984, data is shown in Figure 4.7. If the altitude is not near the peak of the layer, then the gravity wave period is estimated. If the data are near the peak of the layer, the estimate of the gravity-wave period is off by a factor of two due to the double frequency component of the wave found at the layer peak. These two altitude regions are labeled in Figure 4.7. If the altitude region used to calculate the periodogram includes both profiles from near the peak of the layer and away from the peak of the layer, then the estimate of the temporal power spectrum will be distorted and the period of the gravity wave would be unidentifiable. The estimate of the gravity-wave period from the temporal periodogram is a less accurate measure of the period than the spatial periodogram estimate of the wavelength, since gravity waves are typically more variable in time than in space.

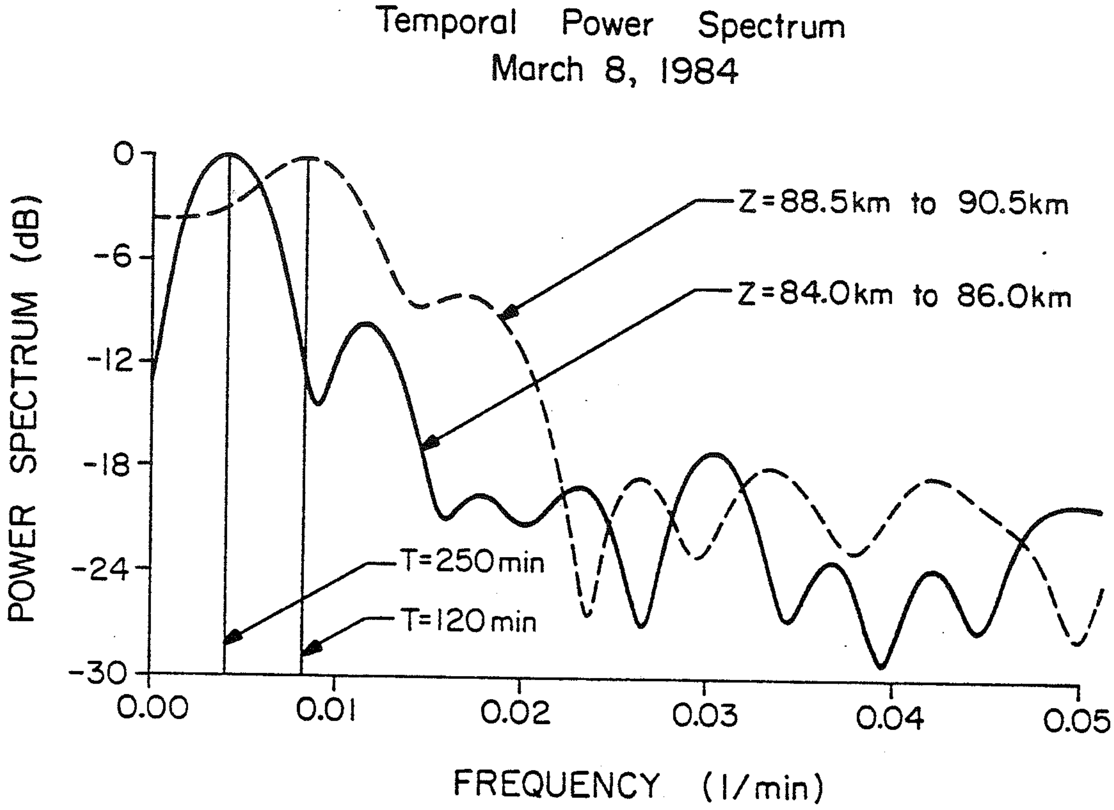

Figure 4.7 The average temporal power spectrum estimate of the normalized data collected on March 8, 1984. The data were spatially filtered with a cutoff of 0.3 km^{-1}. The solid line represents the temporal power spectrum average over the altitude range 4.0 to 86.0 km, a region of steep sodium gradient. The dashed line is the average over the 88.5 to 90.5 km region, the peak of the sodium layer. Note the double-frequency component of the gravity wave period at the layer peak, where the period is 250 minutes.

Thus, the temporal data show no clean temporal frequency peak, and for the relatively short periods where one gravity wave dominates the power spectrum, there are not enough data points for a good estimate of the gravity-wave period.

The periodogram method of estimating gravity-wave parameters is a first attempt to estimate qualitatively gravity-wave activity, but does not give good estimates of actual wavelength and period values. Section 4.3.2 introduces a correlation technique that estimates gravity-wave parameters more accurately than the periodogram.

4.3.2 Correlation of Spatial and Temporal Profiles to Determine Gravity-Wave Parameters

To calculate more accurately the wavelength, period, and vertical phase velocity of a gravity wave from profiles of lidar data, a technique to use the correlation of successive temporal profiles and successive spatial profiles is introduced. This technique assumes that one gravity wave is dominating the dynamics of the region and it is stationary for a long enough period of time to obtain a good estimate of the period. Also, this method defines an upper limit above which a gravity-wave spatial wavelength cannot be accurately measured using this method, since too few spatial data points are available to make a good estimate of the sinusoidal oscillations.

4.3.2.1 Spatial Correlation

The correlation of two functions is defined by

$$<f_1(z),f_2(z)> = \int_{-\infty}^{\infty} f_1(\tau)\, f_2(\tau-z)\, d\tau \qquad 4.14$$

and can be used to determine the vertical wavelength, temporal frequency, and vertical phase velocity of gravity waves propagating through the sodium layer. To analyze the results of the spatial correlation technique, the linearized model of Chiu and Ching [1978] (Equation 5.25), which models the effects of a gravity wave on the sodium layer, is used. The first-order perturbations of the Chiu and Ching solution can be written

$$n'(z,t) = -\left(\frac{n_s(z)}{\gamma-1} + \frac{\gamma H}{\gamma-1} \frac{dn_s(z)}{dz} \right) A \cos(\omega t - k_x x - k_z z) \qquad 4.15$$

Taking the Fourier transform of the correlation function of the first-order perturbations can be shown to be

$$\begin{aligned} \mathcal{F}\{ <n'(z,t_1),\ n'(z,t_2)> \} &= N(\kappa_z)\ N(-\kappa_z) \\ &= \frac{-A}{2(\gamma-1)} \Big((1+\gamma H(\kappa_z - 2\pi/\lambda_z))N_o(\kappa_z - 2\pi/\lambda_z) \\ &\quad +(1+\gamma H(\kappa_z + 2\pi/\lambda_z))N_o(\kappa_z + 2\pi/\lambda_z) \\ &\quad +(1-\gamma H(-\kappa_z + 2\pi/\lambda_z))N_o(-\kappa_z + 2\pi/\lambda_z) \\ &\quad +(1-\gamma H(-\kappa_z - 2\pi/\lambda_2))N_o(-\kappa_z - 2\pi/\lambda_z) \Big) \end{aligned} \qquad 4.16$$

If one defines the bandwidth of the sodium layer to be 2/(RMS width), and if these conditions hold: (1) bandwidth < $1/\lambda_z$, (2) the shape of the steady-state layer is Gaussian (i.e., the RMS width is equal to the variance of the layer), and (3) the layer is symmetric (N(f) = N(-f)), then Equation 4.17 results in

$$\langle n'_{t_1}(z), n'_{t_2}(z)\rangle = A\gamma H/(\gamma-1)\langle dn_0/dz, dn_0/dz\rangle \cos(\omega(t_1-t_2)+2\pi z/\lambda_z) \qquad 4.17$$

Thus, as long as the wavelength is shorter than the width of the layer, the correlation of $n(z,t_1)$ with $n(z,t_2)$ will be proportional to the autocorrelation of the gradient of the sodium layer multiplied by the wave perturbation. Since the correlation function under these assumptions is a function of t_1-t_2 only and the mean value of the layer perturbations is zero, the stochastic process describing the sodium layer density perturbations is wide-sense stationary. One limitation of using the correlation of successive profiles is that long-vertical-wavelength waves cannot be accurately measured; this is in agreement with intuition. Since less than one cycle of the wave is observed, wavelength estimation would be difficult, especially in the presence of noise. For long wavelength waves, it is difficult to estimate the wavelength due to the paucity of data. Calculating the gravity-wave parameters from the data requires the following processing steps:

1. Filtering the data to reduce noise effects.

2. Calculating the average sodium profile for the entire night, n_s.

3. Calculating the perturbation about n_s for the night, i.e., $n' = n - n_s$.

4. Calculating the correlation of $n(z,t_1)$ and $n(z,t_2)$.

5. Normalizing the correlation by the autocorrelation of the gradient of the sodium layer $(\langle dn_s/dz, dn_s/dz \rangle)$.

6. Finding the correlation peak, by a quadratic least-squares fit, which is related to the phase velocity (how much they moved in t_2-t_1 minutes) and find two successive peaks or two successive valleys. The separation between these two peaks or valleys is the wavelength.

A more accurate method of finding the wavelength is to calculate the autocorrelation of each profile. Then, Equation 4.18 reduces to

$$\langle n'(z,t_1), n'(z,t_1) \rangle = \frac{A\gamma H}{\gamma-1} \left\langle \frac{dn_o}{dz}, \frac{dn_o}{dz} \right\rangle \cos(2\pi z/\lambda_z) \qquad 4.18$$

Thus, phase changes due to time are eliminated, and the difference of the frequency between the first valleys on either side of the main correlation peak give an accurate estimate of wavelength.

This technique to measure parameters of gravity waves in the sodium layer was tested on simulated data, as well as actual lidar data collected with the Urbana lidar facility. Two cases are presented to demonstrate the accuracy and usefulness of this technique.

Case 1 uses data calculated from the one-gravity-wave model with the parameters λ_z = 5 km, T = 60 minutes, A = 0.03, σ_1 = 3 km and z_1 = 90 km. A plot (Figure 4.8) of the autocorrelation of a sodium density profile (after step 4) shows that the autocorrelation of the profile is enveloped by the autocorrelation of the gradient of the sodium layer. If the wavelength of the gravity wave is large, then the envelope will distort the correlation valleys and produce an inaccurate estimate of the wavelength (and violate condition 1). A plot of the correlation of two sodium density profiles 10 minutes apart (Figure 4.9) demonstrates that the shifted peak of the correlation is related to the phase velocity of the wave. Table 4.1 shows the results of the correlation from simulations for 60 minutes of profiles and demonstrates that this method produces accurate results within a 3.0% error for wavelength and within 15% for vertical phase velocity.

Case 2 uses the data collected on March 8, 1984. After processing the data, the correlation technique is used to identify the wavelength and vertical phase velocity. Table 4.2 shows the results of the calculations and identifies a 4.99 km gravity wave dominating the dynamics of the sodium layer for most of the early evening. From 22:20 to 22:50, a longer wavelength wave influenced the region, suggesting that the dynamics of the sodium layer are variable and subject to changes much more rapid than the period of one gravity wave. The correlation technique can be used to identify these rapid changes in the gravity-wave structure.

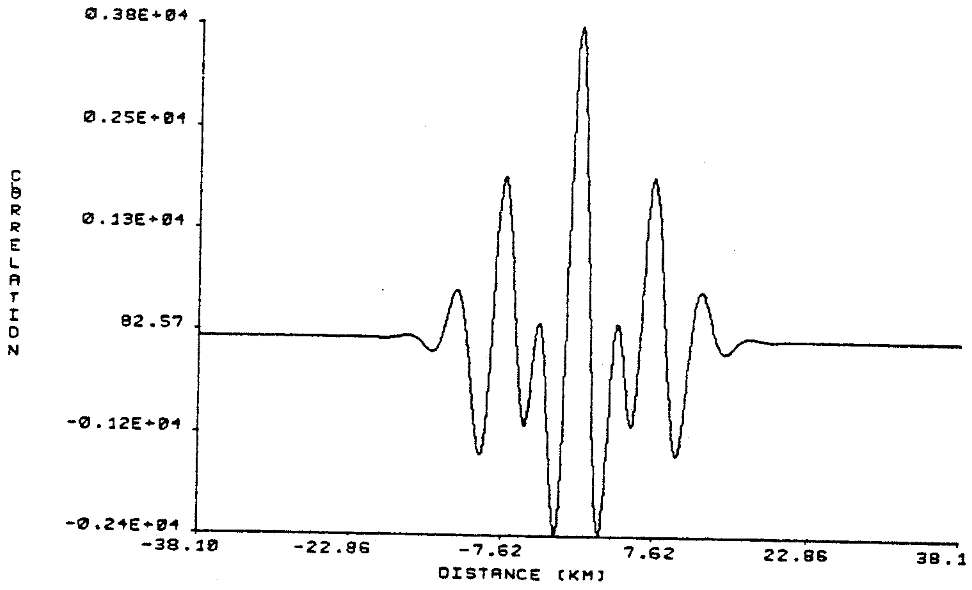

Figure 4.8 The autocorrelation of data calculated from the one-gravity-wave model with a wavelength of 5 km, a period of 60 minutes, and an amplitude of 1.5 m/s. The vertical wavelength can be measured as the distance between two successive peaks or two successive valleys after it is normalized by the envelope, which can be shown to be the autocorrelation of the gradient of the sodium layer.

Table 4.1 Tabulated results of the correlation analysis of the simulated data with a wavelength of 5 km, a period of 60 min, and amplitude of 1.5 m/s. The phase velocity is calculated by correlating the spatial profiles at time 1 and time 2. The wavelength is calculated by autocorrelating the profile at the time listed. The results show the correlation method accurately measures the wave parameters.

Time (min)		Phase Velocity km/min
1	2	
0	10	-0.0950
10	20	-0.0823
20	30	-0.0741
30	40	-0.0741
40	50	-0.0827
50	60	-0.0958
	Average	-0.0841
	Actual	-0.0833

Time (min)		Wavelength km
0		4.85
10		4.85
20		4.98
30		5.13
40		5.13
50		4.98
60		4.85
	Average	4.97
	Actual	5.0

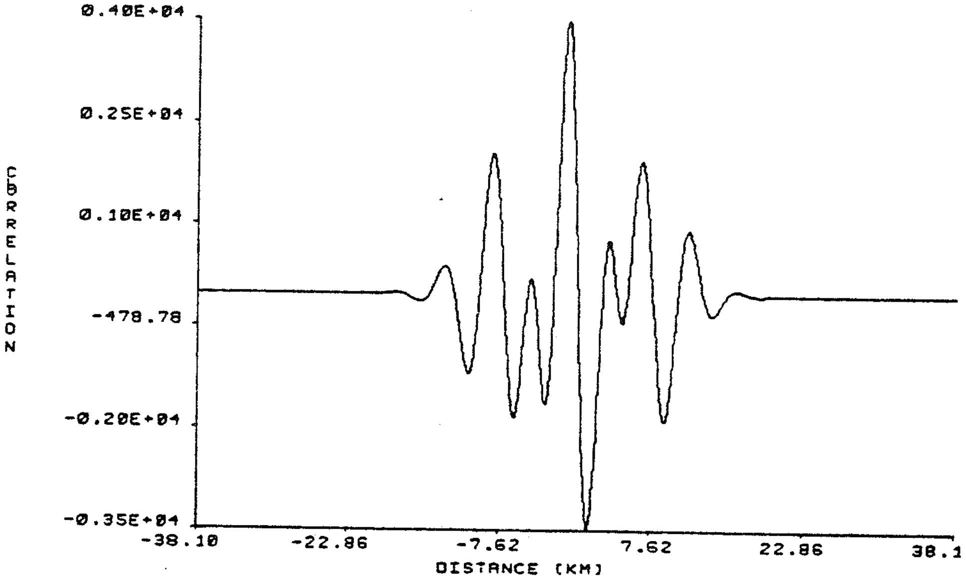

Figure 4.9 The correlation of two successive profiles of simulated data with the same parameters as in Figure 4.8. The phase velocity of the wave is 5 km/hr and causes a shift to the left of the main peak of 0.83 km.

Table 4.2 Tabulated results of the correlation analysis of the data collected on March 8, 1984. These results can be compared to the results of the ASPS which measured a vertical wavelength of 5.1.

Time (hr:min LST) 1	2	Phase Velocity km/min
20:30	20:40	-0.015
20:40	20:50	-0.016
20:50	21:00	-0.023
21:00	21:10	-0.016
21:10	21:20	-0.0091
21:20	21:30	-0.021
21:30	21:40	-0.025
21:40	21:50	-0.042
21:50	22:00	-0.014
22:00	22:10	-0.023
22:10	22:20	-0.018
22:20	22:30	-0.040
22:30	22:40	-0.020
22:40	22:50	-0.0061
22:50	23:00	0.029
23:00	23:10	0.032
23:10	23:20	0.012
23:20	23:30	-0.020
	Average of 20:30-22:30	-.0216

Time (hr:min LST)	Wavelength km
20:30	4.72
20:40	4.71
20:50	4.90
21:00	4.62
21:10	4.45
21:20	5.18
21:30	5.56
21:40	5.86
21:50	5.77
22:00	4.96
22:10	4.45
22:20	13.8
22:30	13.1
22:40	12.9
22:50	6.91
23:00	4.26
23:10	5.13
23:20	5.24
23:30	5.08
Average of 20:30-22:10 and 23:00-23:30	4.99

Period = wavelength/(phase velocity) = 231 min

4.3.2.2 Temporal Correlation

The counterpart of spatial correlation is temporal correlation in which successive temporal profiles are correlated to determine temporal period and vertical phase velocity of the wave features. In the temporal case, the correlation function is not distorted by the gradient of the layer except at the layer peak. The expression for the correlation of two successive temporal profiles can be written:

$$<n'(z_1,t), n(z_2,t)> = C_2 \cos(\omega t + 2\pi/\lambda_z (z_1 - z_2)) \qquad 4.19$$

$$C_2 = A^2\left(\frac{n_o(z_1)}{\gamma-1} + \frac{\gamma H}{\gamma-1} \quad \frac{dn_o(z_1)}{dz} \right) \left(\frac{n_o(z_2)}{\gamma-1} + \frac{\gamma H}{\gamma-1} \quad \frac{dn_o(z_2)}{dz} \right.$$

where n_z' is the variation of the temporal profile about the mean value of sodium density for that altitude. The procedure to calculate the period and vertical phase velocity from the temporal correlation is similar to the calculation for the spatial correlation, except that there is no need to normalize by the autocorrelation of the gradient of the layer (i.e., omit Step 5 of the spatial correlation technique). This is because the gradient of the layer affects only the variations in altitude, not the variations in time at a specific altitude. Again, two cases are used to demonstrate the accuracy of this technique; one with simulated data and one with actual lidar data.

Case 1 uses the same data used for Case 1 of the spatial correlation. The temporal profiles are shown in Figure 4.10 (at each altitude the profiles were normalized to have the same peak-to-peak values). The correlation of two successive profiles at altitudes of 86.5 km and 87.5 km is shown in Figure 4.11. This plot shows the sinusoidal oscillations of the wave at the period of the gravity wave and the offset of the peak closest to zero is related to the phase velocity (since the wave features propagate down, the phase velocity is the first peak on the negative time axis). Figure 4.12 shows the autocorrelation of the profiles at 86 km and demonstrates that the autocorrelation function is periodic at the same period as the gravity wave. Table 4.3 gives the results for a two-hour period of simulated data for all the altitude ranges. The results demonstrate that the method gives accurate results for the simulated data with a maximum error of 10% for period estimation for altitudes not near the peak of the layer or the tails of the layer (where the sodium density falls off to small values) and a maximum error of 15% for the vertical phase velocity.

Case 2 again uses the data from March 8, 1984, during the period from 20:30 to 23:30, to calculate the period and vertical phase velocity. A plot of the temporal profiles is shown in Figure 4.13. Table 4.4 shows the results of the temporal correlations and demonstrates that the double-frequency component of the gravity wave at the layer peak distorts the estimates of period and phase velocity there. Also, the variability of the

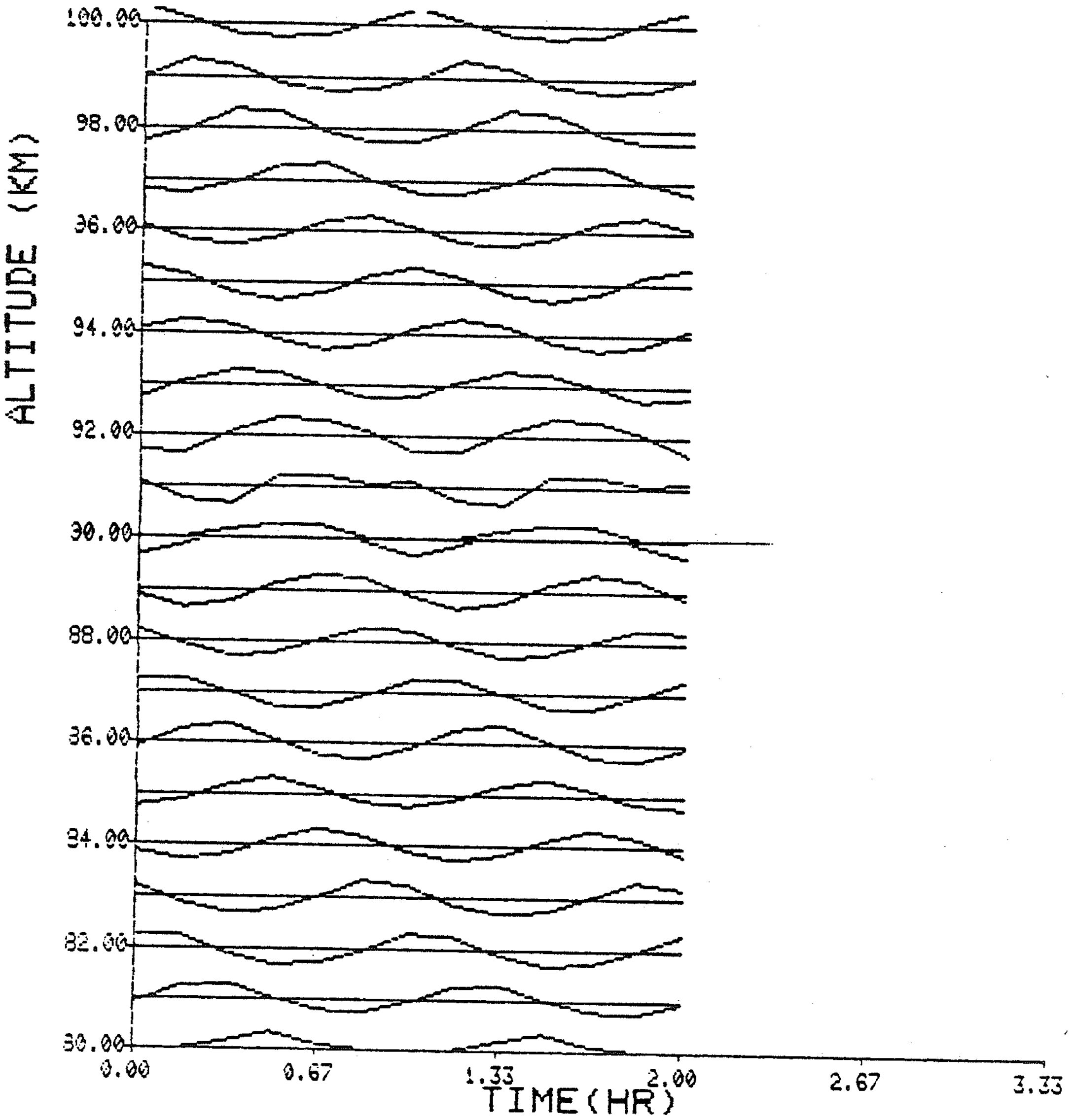

Figure 4.10 Temporal profiles of sodium density variations. The simulated data have a wavelength of 5 km, a period of 60 minutes and an amplitude of 1.5 m/s. The plots at each altitude have the mean density at that altitude subtracted, and the plots are normalized so each altitude range has the same peak-to-peak variations.

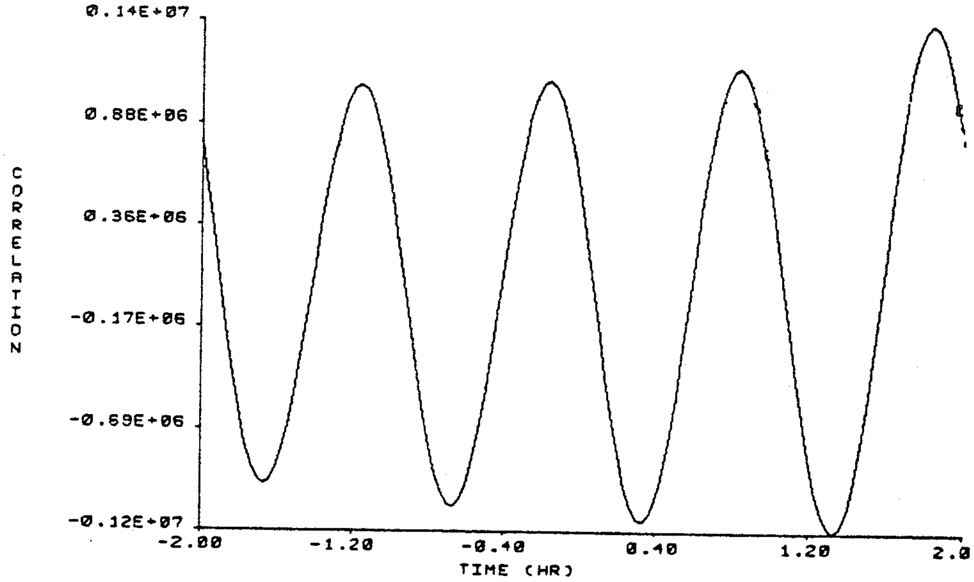

Figure 4.11 Correlation of two successive temporal profiles from Figure 4.11. The two altitudes are 86.5 km and 87.5 km. The period of the gravity wave can be calculated from two successive peak or two successive valleys and the shift of the center peak is related to the phase velocity of the gravity wave. It is known the the center peak will move to the left since the gravity wave phase fronts always propagate down.

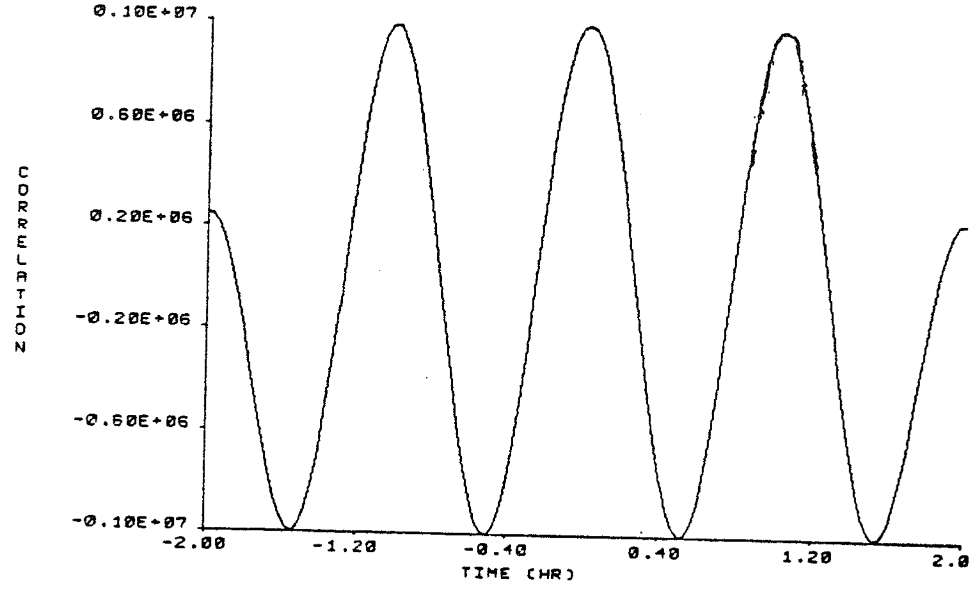

Figure 4.12 Autocorrelation of a temporal profile of the simulated data plotted in Figure 4.11 at an altitude of 86 km. The autocorrelation shows that the period of the wave can accurately be measured form two successive peak or two successive valleys.

Table 4.3 Tabulated results of the temporal correlation analysis of the simulated data with the simulation having the parameters: wavelength of 5 km, period of 60 min, and amplitude of 1.5 m/s. The correlation of two temporal profiles at altitude range 1 and altitude range 2 are used to calculate the phase velocity. The autocorrelation of the temporal profile in the specified altitude range is used to calculate the period.

Altitude Range (km) 1	2		Phase Velocity km/min
80-81	81-82		-0.0825
81-82	82-83		-0.0813
82-83	83-84		-0.0768
84-85	85-86		-0.0868
86-87	87-88		-0.0946
88-89	89-90		-0.0737
92-93	93-94		-0.0941
94-95	95-96		-0.0877
96-97	97-98		-0.0805
98-99	99-100		-0.0809
		Average	-0.0838
		Actual	-0.0833

Altitude Range km		Period min	
80-81		59.2	
81-82		66.6	
82-83		59.4	
83-84		67.8	
84-85		58.1	
85-86		58.6	
86-87		65.4	
87-88		57.5	
88-89		66.0	
90.6-91.0		29.0	(layer peak)
90-91		62.4	
91-92		66.0	
92-93		59.4	
93-94		66.6	
94-95		59.5	
95-96		60.6	
96-97		66.6	
97-98		54.7	
98-99		64.2	
	Average	62.4	(not including 90.6-91.0 km)
	Actual	60.0	

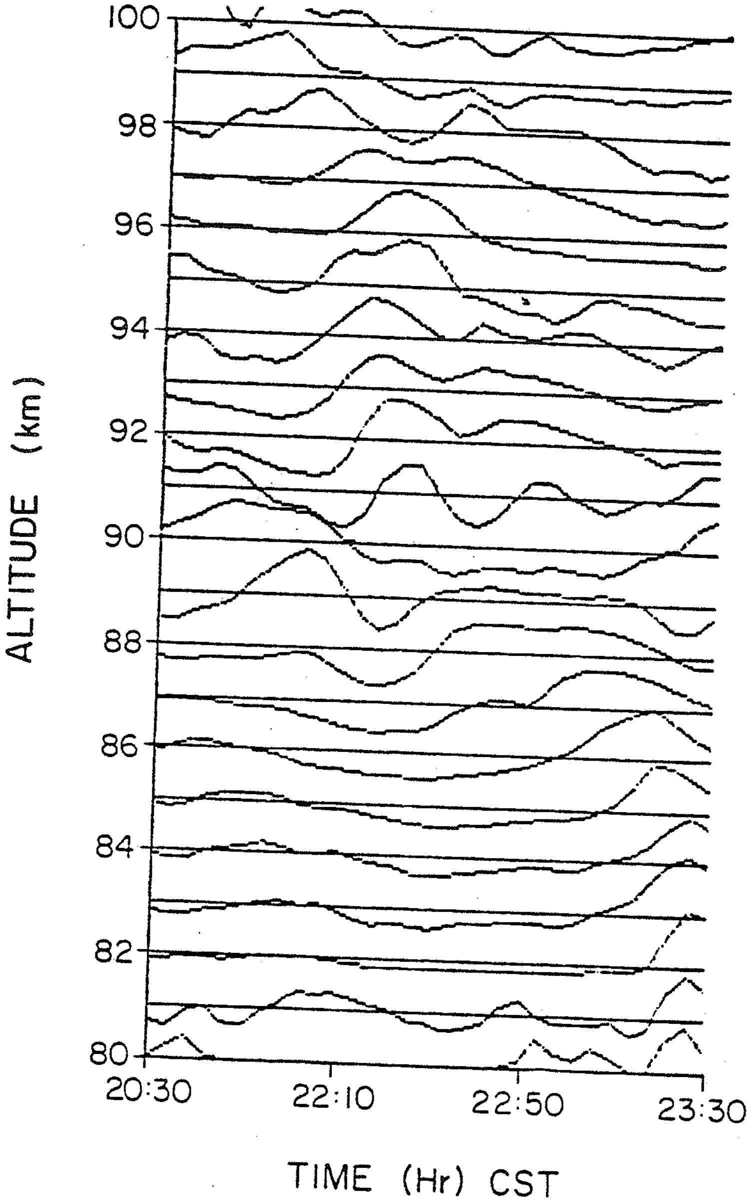

Figure 4.13 Temporal profiles of the data collected from 20:30 CST to 23:30 CST on March 8, 1984. The data were spatially filtered at a cutoff frequency of 1 km^{-1} and temporally filtered at a cutoff frequency of 0.03 min^{-1}. The same normalization steps were used in this temporal plot as in the plot in Figure 4.11.

Table 4.4 Tabulated results of the temporal correlation analysis of the data collected at the Urbana lidar site on March 8, 1984. The altitude ranges were chosen so the density of sodium was large enough to produce good phase velocity and period estimate.

Altitude Range (km) 1	2	Phase Velocity km/min	
84-85	85-86	-0.020	
85-86	86-87	-0.029	
86-87	87-88	-0.037	
87-88	88-89	-0.12	(near
91-92	92-93	-0.072	peak)
94-95	95-96	-0.050	
96-97	97-98	-0.022	
97-98	98-99	-0.019	
98-99	99-100	-0.024	
Average (except near layer peak)		-0.023	

Altitude Range km	Period min	
84-85	208	
85-86	242	
86-87	212	
87-88	144	(near
88-89	97.8	layer
91-92	129	peak)
92-93	229	
93-94	242	
96-97	175	
97-98	254	
98-99	210	
Average(except near the layer peak)	222	

Wavelength = Phase Velocity X Period = 5.1 km gravity-wave activity is shown by the variation of the values in altitude.

An assumption made in the correlation technique is that only one gravity wave is dominate in a spatial or temporal profile. Clearly, this assumption is not always true since typically a spectrum of wave energy is seen in the data, but for certain data sets one gravity wave appears to dominate the gravity wave spectrum (as calculated in the periodogram estimate of the power spectrum) and thus the wavelength and period calculations are valid only in these regions. Other assumptions including the wide-sense stationarity of the density perturbations and linear response of the sodium layer to gravity waves do not hold in general, but do allow for calculation of gravity wave parameters (with intrinsic error depending of the level of disagreement of the theory with the data).

Thus, the correlation technique is a method to accurately determine gravity-wave parameters when it is clear that one gravity wave is dominating the dynamics of the sodium layer. This technique can also be used to determine the variability of the dynamics of the upper mesosphere by observing the variance of the period, wavelength, and vertical phase velocity estimates.

4.4 Estimate of the Variability of Gravity-Wave Perturbations in the Lidar Data Using the Wigner Distribution

In Section 4.3, two techniques to determine the gravity-wave parameters from sodium lidar data were described. These techniques implicitly assumed that wide-sense stationary (i.e., non-time-varying mean) gravity waves were present in the data. The results of gravity-wave parameter estimation showed that the assumption that gravity waves were stationary in the atmosphere was not always valid (or valid for only short periods of time). Section 4.4 introduces a technique that analyzes how the frequency component of the gravity waves varies with time and shows that gravity waves are not in general stationary but can vary greatly over relatively short time periods. Also, features in the time-temporal frequency domain or space-spatial frequency domain can be traced over variations in time or variations in space, respectively.

The Wigner distribution was first proposed by Wigner [1930] for an application in quantum mechanics. It was rediscovered by Ville [1948] and de Bruijn [1973], who developed the mathematical theory of this distribution. Claasen and Mecklenbrauker [1980a, 1980b, 1980c] showed that the Wigner distribution was a powerful tool in the time-frequency analysis of signals. A complete development of the Wigner distribution, both the continuous and discrete forms, can be found in these papers. Also in this set of papers, is the relationship of the Wigner distribution to other time-frequency distributions. It was shown that the Wigner distribution is related to the other forms of the time-frequency distribution typically by a smoothing operation.

The Wigner distribution, which is defined by

$$W(t,\omega) = \int e^{j\omega\tau} \; f(t+\tau/2) \; f^*(t-\tau/2) \, d\tau \qquad 4.20$$

can be shown to be part of a general class of mathematical time-frequency functions first introduced by Cohen [1966] and Margeneau and Cohen [1967]. The Wigner distribution can be shown to have properties that make it an effective analysis tool for time-frequency analysis. These properties are briefly summarized here; a more rigorous analysis can be found in the references. The properties are: (1) The integral of the Wigner distribution over the time variable produces the power spectrum of the signal. (2) The integral of the Wigner distribution over the frequency variable produces the magnitude of the signal squared. (3) Shifts in the time (or frequency) of the signal produce the same shift in the time (or frequency) variable of the Wigner distribution. (4) Signals bounded in time (or frequency) produce Wigner distributions bounded in time (or frequency). (5) The first moment of the Wigner distribution in the time variable at a fixed frequency is equal to the group delay of the system at that frequency. (6) The first moment of the Wigner distribution in the frequency variable at a fixed time is equal to the instantaneous frequency of the signal. (7) The Wigner distribution is real valued. Unfortunately, one property which the Wigner distribution does not possess is that the values of the Wigner distribution are not always positive. Thus, the Wigner does not give exactly the time-frequency response of the signal, but is one of a class of representations which produce similar time-frequency responses. Since the Wigner distribution does not possess the positivity property, it is possible to produce negative energy values in the distribution, but with proper smoothing, these values can be reduced.

The Wigner distribution has been used to analyze a variety of signals including speech processing (Chester [1982]), seismic data, geomagnetic fluctuations, and loud speakers (Janse and Kaizer, [1983]). A fast algorithm using the fast Fourier transform (FFT) is described in Janse and Kaizer. This algorithm actually calculates a pseudo-Wigner distribution, as described by Claasen and Mecklenbrauker [1980a]. It is necessary to calculate the pseudo-Wigner distribution, since the data must be windowed in the time domain to produce finite limits of integration. By introducing this window, the pseudo-Wigner distribution is essentially the exact Wigner distribution convolved with the Wigner distribution of the window function. Thus, the pseudo-Wigner distribution is a spread version of the Wigner distribution and lacks some of the analytic properties of the Wigner distribution, including: (1) The integral of the pseudo-Wigner distribution over the frequency variable does not produce the exact power spectrum. (2) A signal bounded in the frequency will not necessarily have a pseudo-Wigner distribution bounded in frequency due the convolution of the Wigner distribution with a potentially unbounded window function. (3) The first moment of the time-domain variable will not exactly equal the group delay. For normal window lengths of the data, the pseudo-Wigner distribution will closely approximate the Wigner distribution and the pseudo-Wigner distribution will have the same properties as the Wigner distribution.

The Wigner distribution was used on lidar data to determine how the spectral energy of the data was distributed. Since the lidar data are two-dimensional, it is possible to produce both a temporal and spatial Wigner distribution by fixing either the altitude or the time. To improve the resolution of the pseudo-Wigner distribution and reduce the interference between the positive and negative frequency components, a technique that forms the analytic signal from the real signal was used (Janse and Kaizer [1983]). The analytic signal can be written in the Fourier domain as:

$$F_a(\omega) = \begin{cases} 2F(\omega) & \omega > 0 \\ F(\omega) & \omega = 0 \\ 0 & \omega < 0 \end{cases} \qquad 4.21$$

where F_a is the Fourier transform of the analytic signal, and F is the Fourier transform of the signal. This analysis using the analytic signal was performed for both the spatial and temporal Wigner distributions.

The spatial pseudo-Wigner distribution was calculated by first subtracting the average steady-state layer for the night of data, which was estimated by averaging all the profiles for that night, integrating these 10-minute perturbated profiles over a short period, and then calculating the analytic signal of the integrated signal. Finally, the pseudo-Wigner distribution was calculated using the fast algorithm. Figure 4.14 shows the pseudo-Wigner distribution of the data collected on March 8, 1984, from 23:30 to 23:50 CST. The results show that the layer shape greatly influences the spectral components of the wave. Near the peak of the layer, less spectral energy is observed than on the sides of the layer, where the gradient of the layer is large.

The temporal pseudo-Wigner distribution was calculated by integrating the density variations in an altitude range and subtracting the average value to reduce the finite window effects in the data. Then, the analytic signal for the spatially integrated temporal profile and the pseudo-Wigner distribution were calculated. A plot of the temporal pseudo-Wigner is shown in Figure 4.15 for the altitude range 85 to 87 km. The variable nature of the gravity waves in the atmosphere is clearly shown in this plot as the energy at temporal frequencies varies over short time. If stationary gravity waves were present, then energy would be at fixed frequencies and would not vary with time.

4.5 Processing of Lidar Data

To process lidar data more easily, a menu-driven software program was implemented. Section 4.5 describes the processing

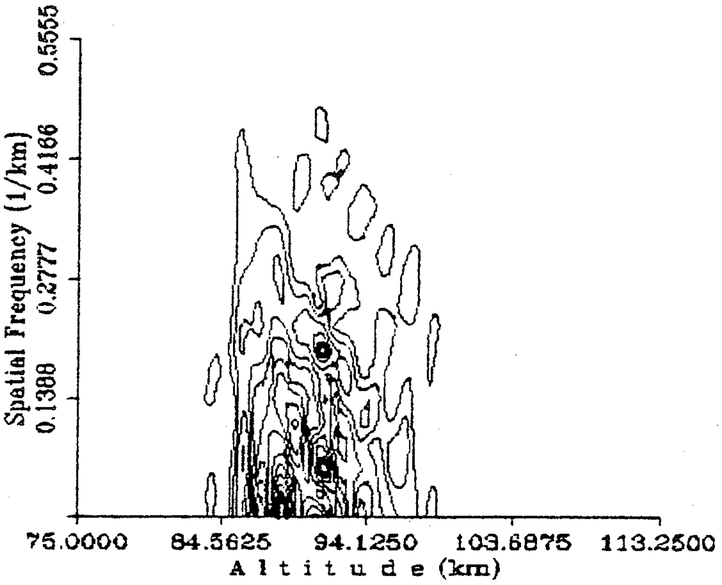

Figure 4.14 Spatial pseudo-Wigner distribution of the data collected on March 8, 1984 from 23:30 to 23:50. The plot shows the layer amplifies the gravity wave effects on the sides of the layer where the gradient is the largest and minimizes the gravity wave effects where the gradient of the layer is a small. Also the variation of the spectral components with altitude is apparent.

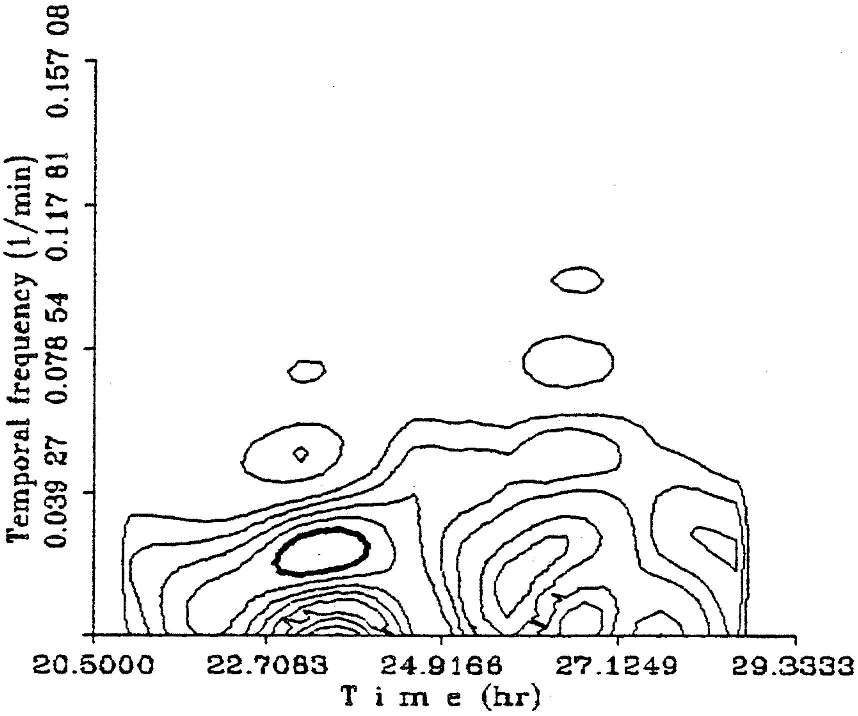

Figure 4.15 Temporal pseudo-Wigner distribution of the data collected on March 8, 1984 in the altitude range 85 to 87 km. While the data were collected, there was a significant change in the spectral components of the perturbations of the sodium layer.

sequence typically used to analyze the lidar data.

The program allows for the input of a data set or simulated data for any of the models derived in Chapter 5. After the data are read into the program, the following functions can be performed in any sequence:

-Spatial filtering
-Temporal filtering
-Spatial periodogram analysis
-Temporal periodogram analysis
-Spatial correlation
-Temporal correlation
-Spatial pseudo-Wigner distribution analysis
-Temporal pseudo-Wigner distribution analysis
-Plotting of spatial profiles
-Plotting of temporal profiles
-Normalization of profiles by column abundance
-Calculation and plotting of column abundance
-Calculation and plotting of centroid
-Calculation and plotting of RMS width
-Calculation of the velocity profiles from lidar data
-Writing data out to a file
-Changing default parameters in the data file.

A typical processing sequence of lidar data collected at the University of Illinois lidar facility is diagrammed in Figure 4.16. The first step of processing the data begins with determining the filter cut-off frequencies for the temporal and spatial Hamming window filters from the average temporal and spatial periodograms. The data are filtered using these cut-off frequencies and the two-dimensional Hamming window filter described in Section 4.1. The data can then be plotted either spatially or temporally to observe any qualitative features that might be in the data. Next, the temporal and spatial periodogram

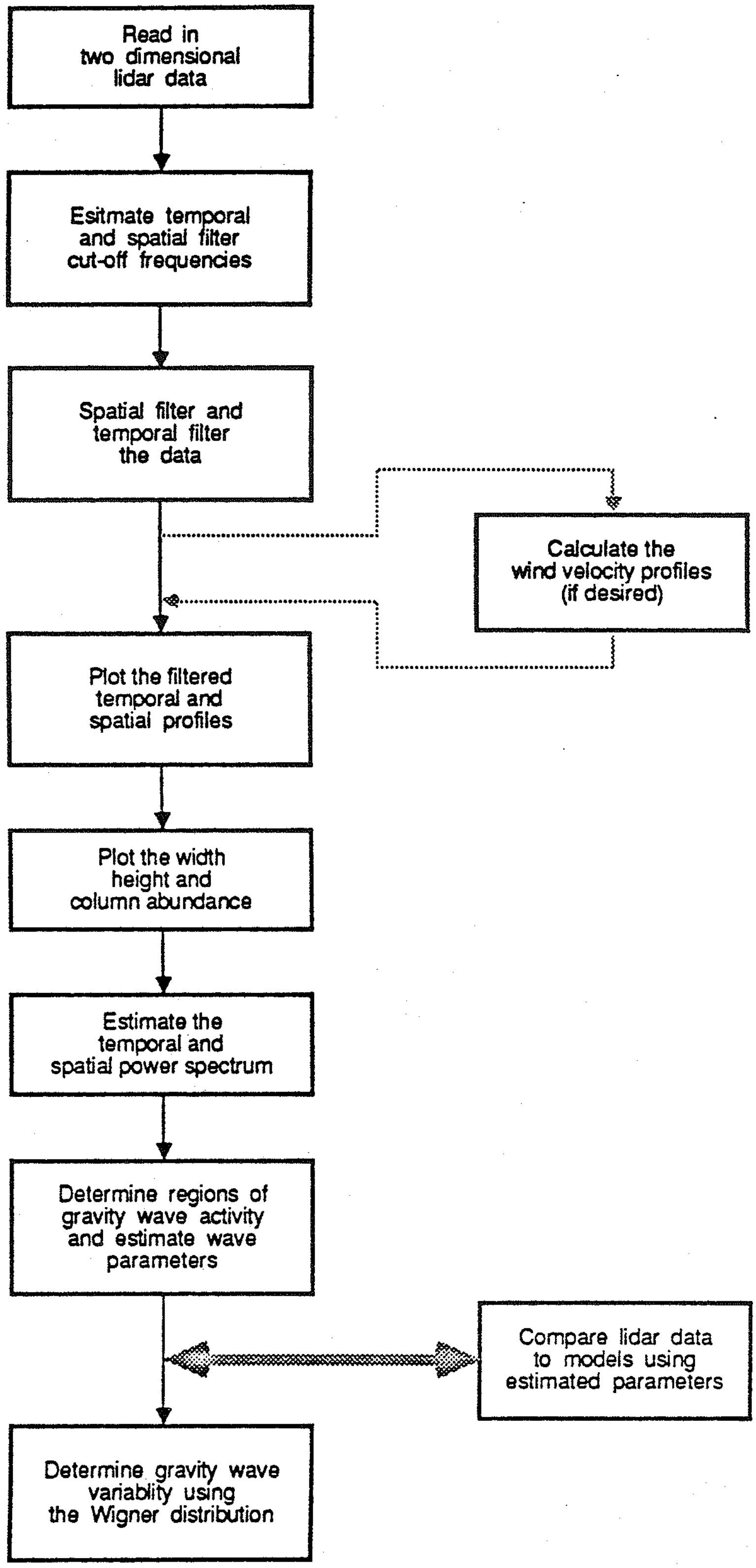

Figure 4.16 Processing steps to analyze lidar data.

estimates of the power spectrum of the raw data are plotted to check for gravity-wave signatures in the data. Typically, spatial periodograms are made for every hour of data, and temporal periodograms are made for every 2 km of data. Also, the RMS width, height, and column abundance variations during the night are plotted to see if any gravity-wave or chemical effects can be isolated. If gravity waves appear to dominate the power spectral estimates then the temporal and spatial correlation techniques are used to determine the wavelength, period and vertical phase velocity of the gravity wave. Next, if good estimates of gravity-wave parameters are made, then data are simulated using the models, and the simulated data are processed to determine whether the model correctly predicted the features. Pseudo-Wigner distributions are also calculated to determine the variability of the gravity-wave features.

A further processing step, especially useful if concurrent wind-velocity measurements are available from the meteor radar (Avery and Tetenbaum [1983]), is to calculate the wind velocity from the lidar data as derived in Chapter 5. The wind velocity profiles can then be processed with identical procedures used to process the sodium density data.

5.0 THEORETICAL DEVELOPMENTS

Modeling the effects of a single monochromatic wave in the atmosphere has been investigated by Chiu and Ching [1978] and Gardner and Shelton [1985]. Tidal oscillations of the sodium layer were observed and modeled by Batista et al. [1985]. This chapter extends the model of the sodium-layer/gravity-wave interactions to include the effects of multiple gravity waves and gravity-wave/mean-flow interactions on the sodium layer. The layer sensitivity to specific wavelengths of gravity waves is also derived and shows that the layer selectively traces gravity-wave activity. By modeling the sodium layer with more realistic atmospheric conditions, it is possible to understand and isolate the mesospheric dynamical features and ascertain the importance of gravity waves in the overall energy balance in the atmosphere. By understanding the layer dynamics through modeling its response, lidar data can be compared to other atmospheric remote-sensing data.

5.1 Review of Gravity-Wave Theory

Hines [1960] first associated irregularities detected in the atmosphere with the occurrence of gravity waves. Mathematically, Hines derived a dispersion relation for the existence of gravity waves by using the four equations that describe the state of the atmosphere: Newton's second law, the equation of energy conservation, the continuity equation, and the equation of state. These equations are:

$$\rho \frac{\delta \underline{\underline{V}}}{\delta t} - \rho \underline{\underline{g}} + \nabla p = 0 \qquad 5.1$$

$$c_v \frac{dT}{dt} + p \frac{d}{dt} \left(\frac{1}{\rho}\right) = 0 \qquad 5.2$$

$$\frac{\delta \rho}{\delta t} + \nabla(\rho \underline{\underline{V}}) = 0 \qquad 5.3$$

$$p = \rho RT \qquad 5.4$$

where

ρ = the density of the atmosphere,

V = the velocity field of the atmosphere,

p = the atmospheric pressure,

g = the acceleration due to gravity,

c_v = the specific heat at a constant volume,

T = the temperature,

R = the gas constant.

If the following assumptions are made:

(1) that the atmosphere is uniform in both temperature and composition,
(2) that wave motion behaves linearly (i.e., $\rho = \rho_o + \rho'$, $p = p_o + p'$, and $\underline{V} = (V_x, 0, V_z)$),
(3) that the gravitational acceleration is constant in both magnitude and direction,
(4) that the atmosphere is inviscid,
(5) that the wave motion is sinusoidal; then the pressure, density, and velocity fields can be written

$$j\omega V_x - jK_x gHp' = 0 \qquad 5.5$$

$$j\omega V_z + g\rho' - g(1+jK_z H)p' = 0 \qquad 5.6$$

$$\frac{\gamma-1}{H} V_z - j\omega\gamma\rho' + j\omega p' = 0 \qquad 5.7$$

$$-jK_x V_x - (1/H + jK_z) V_z + j\omega\rho' = 0 \qquad 5.8$$

where $H=a^2/\gamma g$ is the fluid scale height, and the perturbations due to wave oscillations can be written in complex Fourier form, proportional to $\exp(j(\omega t-K_x x-K_z z))$. The determinant of Equations 5.5 through 5.8 can be calculated, and a nontrivial solution exists only if the determinant equals zero. This equation formed by setting the determinant equal to zero is known as the dispersion relation, and relates the period of the wave, the horizontal and vertical wavelengths of the wave, the ratio of specific heats of the atmosphere, the speed of sound in the atmosphere, $a=\gamma p/\rho$, and the gravitational constant. The dispersion relation can be written

$$\omega^4 - \omega^2 a^2(K_x^2 + K_z^2) + (\gamma-1)\, g^2 K_x^2 + j\omega^2 \gamma g K_z = 0 \qquad 5.9$$

Equation 5.9 shows that K_x and K_z cannot both be real and nonzero (Georges [1967]). Assuming that properties of the medium do not change horizontally, and that there is no dissipation of the wave in the atmosphere, then the horizontal wave number must be real. Thus,

$$K_z = k_z + jk_{zi} \qquad 5.10$$

and

$$K_x = k_x. \qquad 5.11$$

Therefore, Equation 5.9 reduces to

$$2k_z k_{zi} a^2 \omega^2 = \gamma\ g\ k_z\ \omega^2. \qquad 5.12$$

Thus, by solving Equation 5.12 either

$$k_z = 0 \qquad 5.13$$

or

$$k_{z_i} = \frac{\gamma g}{2a^2} = \frac{1}{2H} \qquad 5.14,$$

where H is the scale height of the atmosphere. If k_z=0, then the solution corresponds to a surface or external wave. Thus, the second choice (k_{zi} = 1/2H) is of more interest. This solution implies that the wave grows exponentially with height, but it is also consistent with conservation of energy (Equation 5.2). The exponential decrease of the atmospheric density causes the wave energy density to be constant with height. Even with the amplitude of the wave growing exponentially with altitude, the wave energy is constant.

By using the real part of the dispersion relation and defining an acoustic cut-off frequency (Hines [1960]) as ω_a= g/2a. And also noting that the Brunt-Vaisala frequency, which is the frequency at which a fluid parcel oscillates about its equilibrium position, can be written

$$\omega_b^2 = \frac{(\gamma-1)g^2}{a^2} \qquad 5.15$$

Then the general conic form of the dispersion relation can be written (Georges [1967])

$$k_x^2 \frac{a^2(\omega_b^2 - \omega^2)}{\omega^2(\omega_a^2 - \omega^2)} + k_z^2 \frac{a^2}{\omega^2 - \omega_a^2} = 1 \qquad 5.16$$

For $1<\gamma<2$ (typically in the atmosphere $\gamma=1.4$), then $\omega_a > \omega_b$ and there are three frequency ranges of interest for atmospheric studies. Georges [1967] showed that the three regions of the solutions refer to different types of conic solutions to Equation 5.16 and this leads to three different types of wave oscillations. For $\omega < \omega_b < \omega_a$, the lines of constant ω in Equation 5.16 are hyperbolae in the k_x-k_z plane and produce waves that are influenced more by gravity than by compressional effects. The waves propagate vertically and are referred to as internal gravity waves. For the case of $\omega_b<\omega<\omega_a$, either k_x or k_z must be imaginary; thus, the solutions are evanescent waves, and the waves transport no energy or momentum. Finally, for $\omega_b<\omega_a<\omega$, the lines of constant ω form ellipses in the k_x-k_z plane, showing that the waves are influenced by compressional effects more than gravitational effects. The resulting waves are longitudinal waves, commonly referred to as acoustic waves. One way to describe wave motion is to consider the paths followed by fluid parcels. These parcel orbits, called the polarization relations, were first derived by Hines [1960] and can be written

$$\frac{p-p_0}{p_o P} = \frac{\rho-\rho_0}{\rho_0 R} = \frac{V_x}{X} = \frac{V_z}{Z} = A\,e^{j(\omega t-K_x x-K_z z)} \tag{5.17}$$

$$P = \gamma\omega^2 K_z - \frac{j\gamma g\omega^2}{a^2} \tag{5.18}$$

$$R = \omega^2 K_z + j(\gamma-1)gK_x^2 - \frac{j\gamma g\omega^2}{a^2} \tag{5.19}$$

$$X = \omega K_x K_z a^2 - jg\omega K_x \tag{5.20}$$

$$Z = \omega^3 - \omega K_x^2 a^2 \tag{5.21}$$

It is interesting to note the parcel orbits in two extreme cases. First, consider the case where the wave is influenced solely by compressional effects and no gravity effects, i.e., g -> 0; then the parcel orbits can be reduced to

$$\frac{V_x}{V_z} = \frac{Z}{X} = \frac{K_x}{K_z} \tag{5.22}$$

The parcel orbits are therefore parallel to the direction of wave propagation, making them longitudinal or acoustic waves. In this case, V_x and V_z are in phase. On the other extreme, if there are no compressional effects (which implies a->0) and gravity is the only driving force, then

$$\frac{V_x}{V_z} = \frac{Z}{X} = -\frac{K_z}{K_x} \qquad 5.23$$

If $k_z >> 1/2H$, then the parcel orbits are perpendicular to the direction of wave motion, and the waves are transverse (or gravity) waves. In this case, V_x and V_z are 180° out of phase.

In general, the atmospheric waves are a mixture of pure acoustic and pure gravity waves. Acoustic-gravity waves have parcel orbits that are elliptic. Figure 5.1 shows the parcel motions for various frequencies.

5.2 The Model of One Gravity Wave in the Sodium Layer

The linear model, relating interactions of a monochromatic gravity wave with the sodium layer, was first derived by Chiu and Ching [1978] by solving the linearized equations of continuity:

$$(\frac{\delta}{\delta t} + \underline{\underline{V}}\cdot\nabla)\frac{n'}{n_s} + (\frac{1}{n_s}\frac{dn_s}{dz} - jK_z)(1 + \frac{n'}{n_s})V_z - jK_x(1 + \frac{n'}{n_s})V_x = 0 \qquad 5.24$$

Here, it was assumed that the velocity field was due to gravity waves (Hines [1960]). The solution, which can be written as

$$\frac{n'(x,z,t)}{n_s(z)} \approx -\frac{1}{\gamma-1}(1 + \frac{\gamma H}{n_s}\frac{dn_s}{dz})\frac{\rho'}{\rho_a} \qquad 5.25$$

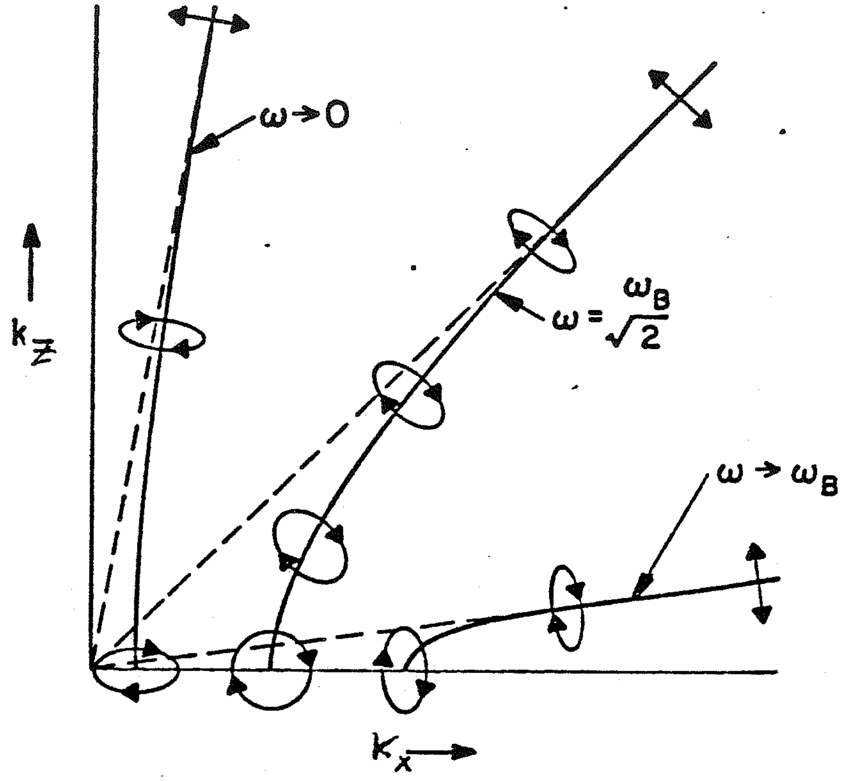

Figure 5.1 Typical air parcel orbits for internal gravity waves of various frequencies (after Georges, 1967).

$$n = n_s + n'$$

where

n' = the linear (first-order) perturbation of the unperturbated sodium layer, $n_0(z)$,

γ = the ratio of specific heats,

H = the scale height of the atmosphere and is assumed to be a constant in the region of the sodium layer,

ρ_a = the background atmosphere density,

ρ_a' = the neutral atmosphere linear perturbations.

The perturbations of the neutral atmosphere can be written

$$\frac{\rho'}{\rho_a} = A\, e^{j(\omega t - K_x x - K_z z)} \qquad 5.26$$

where A is equal to the amplitude of the gravity wave, ω is the temporal frequency of the gravity wave, k_x is the horizontal wave number, and $K_z = k_z + j/2H$, k_z is the vertical wave number. From Equation 5.25, Chiu and Ching showed that the sodium layer will amplify the gravity-wave effects on the sides of the layer, where the gradient is largest, and will not amplify the wave effects at the peak of the layer, where the gradient is small. Also, there is a 180° phase reversal at the peak of the layer due to the change of sign of the gradient. The solution was shown by Chiu and Ching [1978] to agree with the experimental results of measurements of the ozone layer, the atomic oxygen layer, the sporadic E layer, and the D and E regions of the ionosphere.

Gardner and Shelton [1985] solved the equations of continuity to find a more exact solution of the density response to a gravity wave in the sodium layer. To solve this equation, they made several assumptions: (1) The diffusion time of the minor constituent (sodium) forming the atmospheric layer is much greater than the period of the atmospheric waves, which induce the observed density perturbations. This implies that the velocity field of the minor constituent equals the atmospheric velocity. (2) Only wave-induced dynamics are considered; no chemical effects are included. This reduces the source and sink terms to zero. (3) The sodium layer has a density profile $n_s(\underline{\underline{r}})$. (In the absence of wave activity, it is a function of position only, where $\underline{\underline{r}}$ is the vector representation of Cartesian coordinates (x,y,z).) (4) The vertical wavelength of the gravity wave satisfies the inequality:

$$\lambda << 4\pi H \tag{5.27}$$

Furthermore, it was assumed that the solution has the form:

$$n(\underline{\underline{r}},t) = e^{\phi} n_s(\underline{\underline{r}} + \underline{\underline{\theta}}) \tag{5.28}$$

The factors ϕ and $\underline{\underline{\theta}}$ represent perturbations of the background density n_s. In general, $\underline{\underline{\theta}}$ has horizontal and vertical components, i.e. θ_x and θ_z. These terms account for displacements in the layer as it is swept along by the gravity wave. The factor $\exp(\phi)$ accounts for density perturbations that would result in a homogeneous atmosphere due to gradients in the gravity-wave velocity field.

Substituting 5.28 into the equation of continuity results in the following partial differential equations:

$$\frac{\delta \phi}{\delta t} = -(\nabla \cdot \underline{\underline{V}} + \underline{\underline{V}} \cdot \nabla \phi) \qquad 5.29$$

$$\frac{\delta \Theta_x}{\delta t} = -(V_x + \underline{\underline{V}} \cdot \nabla \Theta_x) \qquad 5.30$$

$$\frac{\delta \Theta_z}{\delta t} = -(V_z + \underline{\underline{V}} \cdot \nabla \Theta_z) \qquad 5.31$$

To solve Equations 5.29 through 5.31, the velocity field of the gravity wave must be known. The velocity field of a monochromatic gravity wave is, in general, given by Hines [1960]

$$\underline{\underline{V}} = A \, \mathrm{Re}\left[\underline{\underline{\beta}} \; e^{j(\omega t - K_x x - K_z z)} \right] \qquad 5.32$$

with

$$\beta_x = j \frac{K_x}{K_z} \gamma \frac{H\omega}{\gamma - 1} \left(1 - \frac{\omega_b^2}{\omega^2}\right) \qquad 5.33$$

$$\beta_z = j \frac{\gamma H \omega}{\gamma - 1} - \frac{\omega}{(\gamma - 1) K_z} \qquad 5.34$$

Gardner and Shelton determined the solution to be

$$n(x,z,t) = (1 - (\frac{A}{\gamma-1} e^{z/2H} \cos(\omega t-k_x x-k_z z) \cdot \qquad 5.35$$

$$n_s(z - \frac{\gamma H}{\gamma-1} A e^{z/2H} \cos(\omega t-k_x x-k_z z))$$

They showed that nonlinearities of the solution can affect the response of the layer for large-amplitude waves, but for waves in the amplitude region in which the velocity field (assumed by the solution) is valid, the linear and nonlinear solution are very close. However, it is important to note, that if the amplitude of the waves are allowed to get large, then other nonlinearities of the atmosphere, such as wave breaking and saturation, will distort the waves and thus contradict the velocity field assumed for this solution.

Gardner and Shelton also used the linear solution to predict the spectral signature of a monochromatic wave. They showed that the normalized average spatial power spectrum (ASPS) of a gravity-wave perturbing the layer can be expressed in the spectral domain as the Fourier transform of the steady-state layer added to the Fourier transform of the linear perturbations. The expression can be written assuming no amplitude growth of the wave in the layer (Equation 5.27), and the layer has a Gaussian shape defined by

$$n_s(z) = \frac{n_0}{\sqrt{2\pi}\,\sigma_1} e^{-(z-z_s)^2/2\sigma_1^2} \qquad 5.36$$

as

$$\mathrm{ASPS} = n_0^2 \{ e^{-\kappa\sigma_1^2} + (\frac{A}{2(\gamma-1)})^2 e^{-(\kappa-k_z)\sigma_1^2} (1 + (\kappa-k_z)^2\gamma^2H^2) \} \qquad 5.37$$

where κ is the transform variable and σ_1 is the width of the Gaussian layer.

Thus, it was shown that the spectral signature of a gravity wave, with these assumptions, is a notch in the power spectrum at the frequency of the wave and two peaks in the power spectrum offset from the notch. The offset distance is related to the width of the layer and the atmospheric parameters and the frequency of the two spectral peaks can be written

$$\kappa_{z_{peak}} = \kappa_{z_{wave}} \pm \sqrt{1/\sigma_1^2 - 1/\gamma^2H^2} \qquad 5.38$$

The model for the sodium layer can be used to predict the response of the layer height, width, and column abundance. The column abundance, C_s, the height, Z_s, and the width, σ_s of the sodium layer are calculated using the definitions of the moments of the layer as noted in Chapter 4, Equations 4.7 through 4.10.

Analytic expressions for C_s, Z_s and σ_s can be derived using the linear solution and can be written in terms of the steady-state layer (C_{ss}, Z_{ss} and σ_{ss}) and a perturbation solution. A Gaussian shape for the steady-state layer with a width σ_1 (Equation 5.36) is also assumed for this calculation. The expressions can be written, by using the moment theorem (Papoulis [1965]), as:

$$C_s = C_{ss} + \Delta C_s \qquad 5.39$$

$$Z_s = Z_{ss} + \Delta Z_s \qquad 5.40$$

$$\sigma_s = \sigma_{ss} + \Delta\sigma_s \qquad 5.41$$

The column-abundance, width, and height perturbations can be calculated in terms of the magnitude and phase. Since the phase of a harmonic signal is always relative to some origin or start time, the phase of the variations of the column abundance, width, and height are taken relative to the phase of the gravity wave causing the perturbations, i.e. the phase of the gravity wave is assumed to be zero. Assuming Equation 5.27 holds, these perturbations of the column abundance, height, and width can be expressed:

$$|\Delta C_s|^2 = (A\ e^{z_s/2H}\ e^{-k_z^2\sigma_1^2/2})^2\ \frac{C_{ss}^2}{(\gamma-1)^2}\ (1 + (k_z\gamma H)^2) \qquad 5.42$$

$$\text{phase}(\Delta C_s) = \tan^{-1}(\frac{k_z\gamma H}{-1}) \qquad 5.43$$

$$|\Delta Z_s|^2 = (\frac{A}{\gamma-1}\ e^{z_s/2H}\ e^{-k_z^2\sigma_1^2/2})^2\ [(\gamma H(k_z^2\ \sigma_1^2 - 1))^2 + (k_z\sigma_1^2)^2] \qquad 5.44$$

$$\text{phase}(\Delta Z_s) = \tan^{-1}(\frac{-k_z\sigma_1^2}{-\gamma H(k_z^2\sigma_1^2-1)}) \qquad 5.45$$

$$|\Delta\sigma|^2 = \left(\frac{A}{2(\gamma-1)\sigma_1} e^{z_s/2H} e^{-k_z^2\sigma_1^2/2}\right)^2 \left[(k_z^2 \sigma_1^4)^2 + (\gamma H k_z \sigma_1^2 (2-k_z^2\sigma_1^2))^2\right] \qquad 5.46$$

$$\text{phase}(\Delta\sigma_s) = \tan^{-1}\left(\frac{-\gamma H(k_z^2\sigma_1^2 - 2)}{k_z\sigma_1^2}\right) \qquad 5.47$$

Equations 5.42 and 5.43 are used to derive the plots shown in Figure 5.2. The results show that the column-abundance variations are sensitive to wavelength. A wave with a wavelength below 5 km is undetectable in column-abundance variations. Depending on the width of the layer, the column abundance variations reaches a peak in the 10 to 15 km wavelength range. This agrees with the observed gravity-wave effects on the column abundance and also explains why lidar systems typically detect waves with a 5 to 15 km wavelength. The phase variation of the column abundance (Figure 5.2b) shows that the oscillations are approximately 90° out of phase with the gravity wave and vary linearly with wavelength. The variation of the height (centroid) of the layer with wavelength and width of the layer is shown in Figure 5.3. The height of the sodium layer is more sensitive to certain wavelengths and layer widths. A peak occurs at $\lambda_z=2\pi\sigma_1$. Figure 5.3b shows that the phase of the variations relative to the gravity wave vary greatly depending on the wavelength. For small wavelengths, there is a -180° phase shift relative to the gravity wave, but for large wavelengths the phase shift is 0°, as

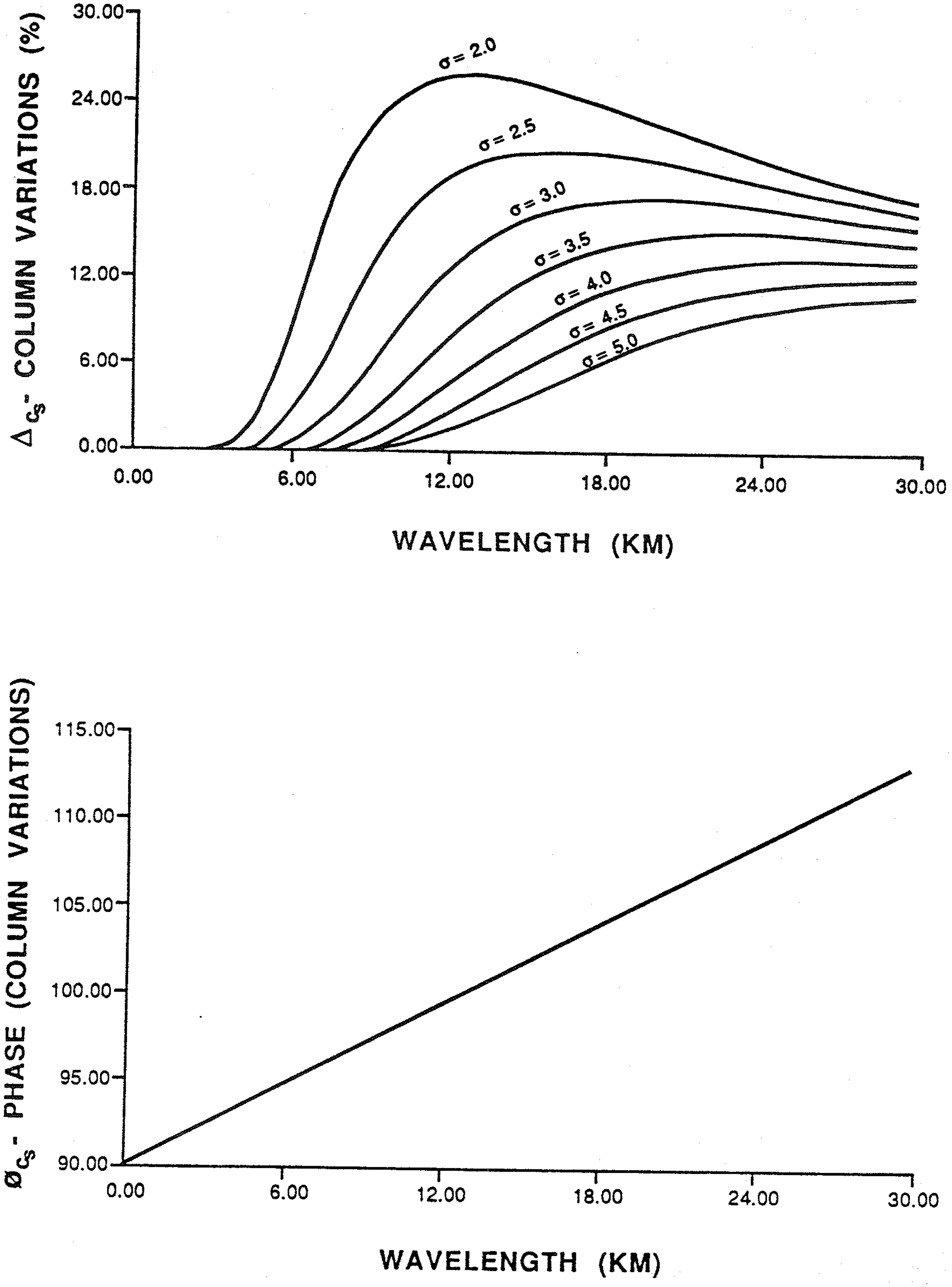

Figure 5.2 Sensitivity of the column abundance variations to various wavelengths and layer widths. (a) Magnitude of the variations. (b) Phase of the variations.

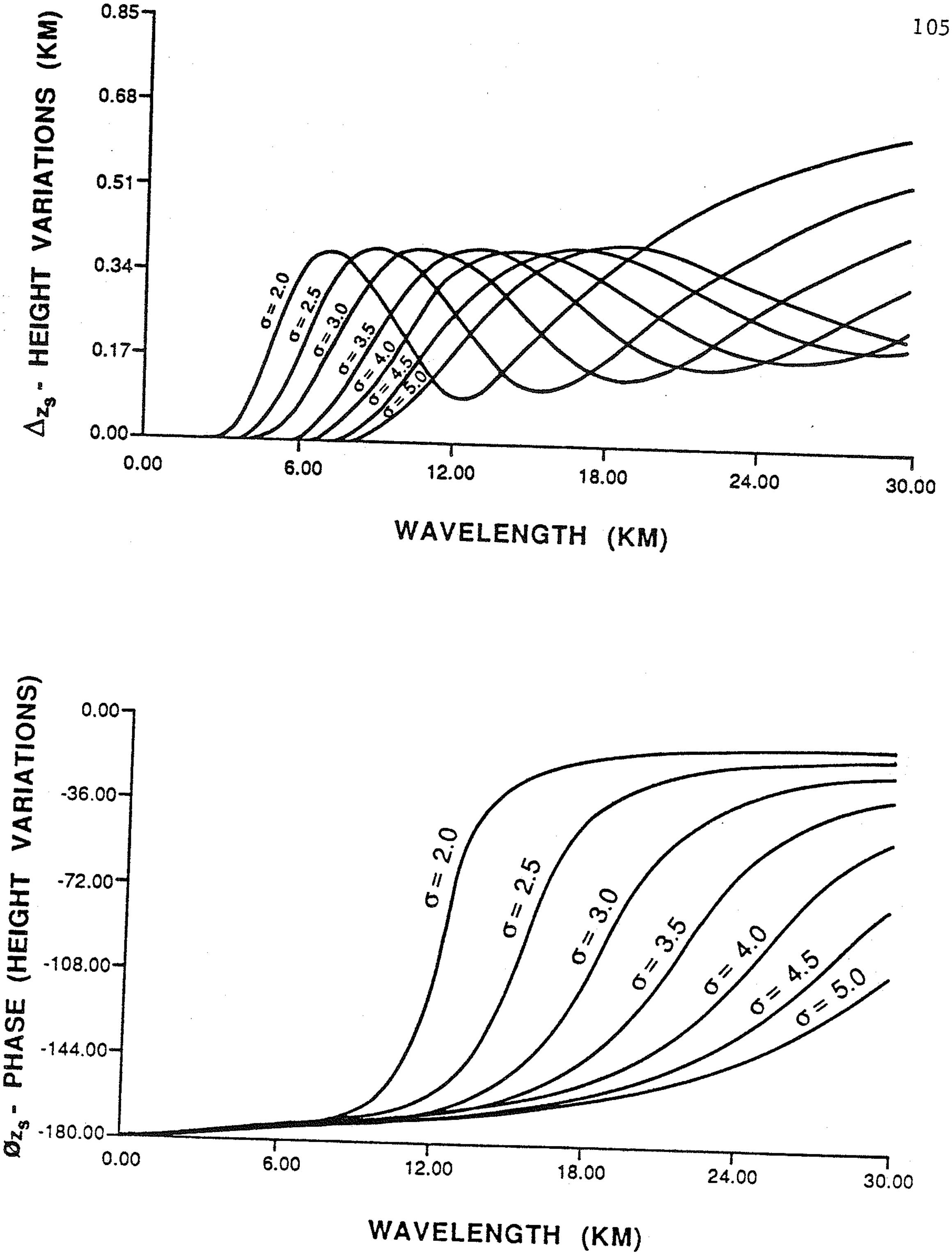

Figure 5.3 Sensitivity of the height variations to various wavelengths and layer widths. (a) Magnitude of the variations. (b) Phase of the variations.

seen in Equation 5.45. For wavelengths between the two extremes, the behavior follows the curve of an arc tangent; thus, the phase reverses rapidly.

Figure 5.4 shows the width variations versus wavelength of a monochromatic gravity wave for several layer widths. Similarly to Figures 5.2 and 5.3, Figure 5.4 shows that the width variations reach a sharp maximum, but the maximum occurs at shorter wavelengths than those observed for the column abundance or height. The phase of the width variations is very similar to that of the height variations except the phase ranges from -90° to 90° relative to the gravity wave, and the wavelength at which the phase changes is larger than that observed for the height variations.

By comparing Figures 5.2a, 5.3a, and 5.4a, one can draw several conclusions concerning the importance of the layer sensitivity to the wavelength of the gravity wave and to the width of the layer in the analysis of lidar data. For the width and height, there appears to be a sharp peak in magnitude where the response of the layer is most sensitive, and a sharp valley at a higher wavelength, where the response is least sensitive. Both the width and height show a maximum response to approximately the same wavelength for the same width of the layer (i.e., for $\sigma_1=3$ km the range from about 7 to 11 km has the greatest response for both the height and width). Also, the height and width have a minimum response to a gravity wave, depending on the width of the layer at about twice the wavelength of the maximum response.

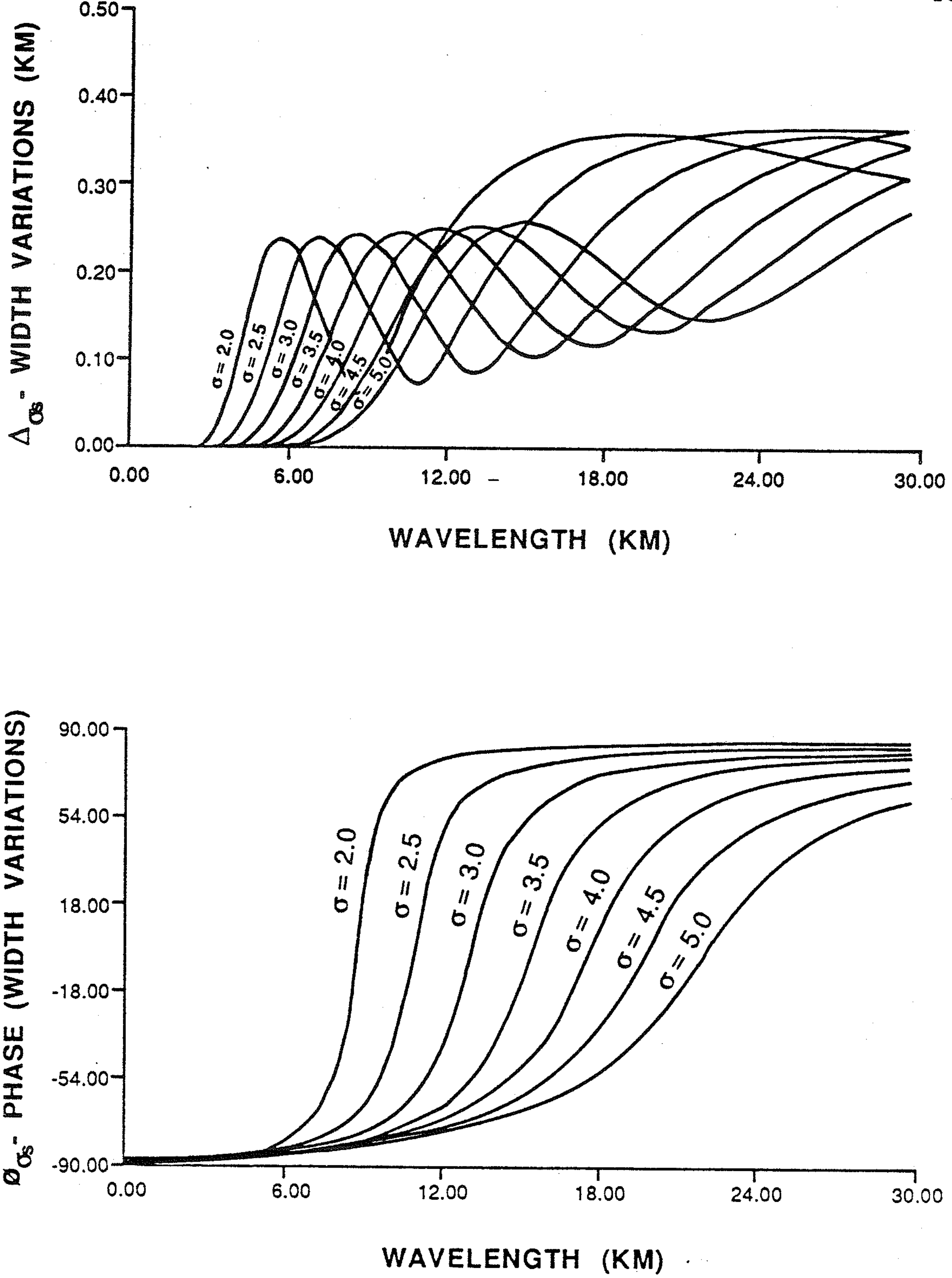

Figure 5.4 Sensitivity of the RMS width variations to various wavelengths and layer widths. (a) Magnitude of the variations. (b) Phase of the variations.

Above the minimum response wavelength, the curve for the width and height variations grows asymptotically to a constant value, but as the wavelength becomes large, the assumptions made in the derivation of the model break down, so the results are no longer valid. The column abundance, in contrast to the height and width, has a peak response at about $\lambda_z=2\pi\sigma_1$ and falls off asymptotically to a constant value at higher wavelengths. Also, the wider the layer is, the less sharp the peak of the curve, and thus, the column abundance is less sensitive to wavelength variations.

In terms of dynamics of the layer, these curves show that the layer has a wavelength at which the the response is "tuned" to the layer width. This means that the gravity wave pushes the maximum amount of sodium up to maximize the height variations of the layer. At a different wavelength, the gravity wave pushes sodium vertically away from the center of the layer to maximize the width. Finally, at a third wavelength, the gravity wave horizontally pushes sodium into the observed point in the layer to maximize the column abundance. The same is also true for the minimum points in the variations of the width and height.

Figures 5.2b, 5.3b, and 5.4b show the phase of the height, width, and column-abundance variations referenced to the phase of the gravity wave(i.e. the phase of the gravity wave is assumed zero). These figures indicate that, for gravity waves with small wavelength ($\lambda_z<2\pi\sigma_1$) the width and column-abundance variations are 180^o out of phase. The height variations lag the width variations by 90^o. This implies that short-wavelength gravity waves affect the layer first by broadening the layer, decreasing the column abundance, and causing a rise in the height of the layer. Then, a half gravity-wave cycle later, the layer becomes narrower, the column abundance increases, and the height of the layer decreases. For larger waves (i.e. λ_z=12 km for a σ_1=3 km) the only change is a 180^o phase shift in the width perturbations. Thus, as the column abundance increases, the width increases, and the height of the layer increases (lagging by 90^o). Then, the column abundance decreases, the layer narrows, and the height of the layer decreases. Figure 5.5 shows the results for the height, width, and column-abundance variations for simulated data, with λ_z=5 km, the wave period, T, equal to one hour, and the background density variations equal to 3%. These simulated results agree with the analytic results and graphically show the same effects of a gravity wave on the layer.

5.3 Sodium Layer Models with More Realistic Atmospheric Conditions

The one-gravity-wave model can be used to derive many characteristics of the sodium layer. But, in the atmosphere, a more complex situation typically exists. One way to model the complex atmosphere is to model several possible scenarios. Then, when analyzing the data, categorize the data into one of the models. In Section 5.3, two more complex dynamical models of the

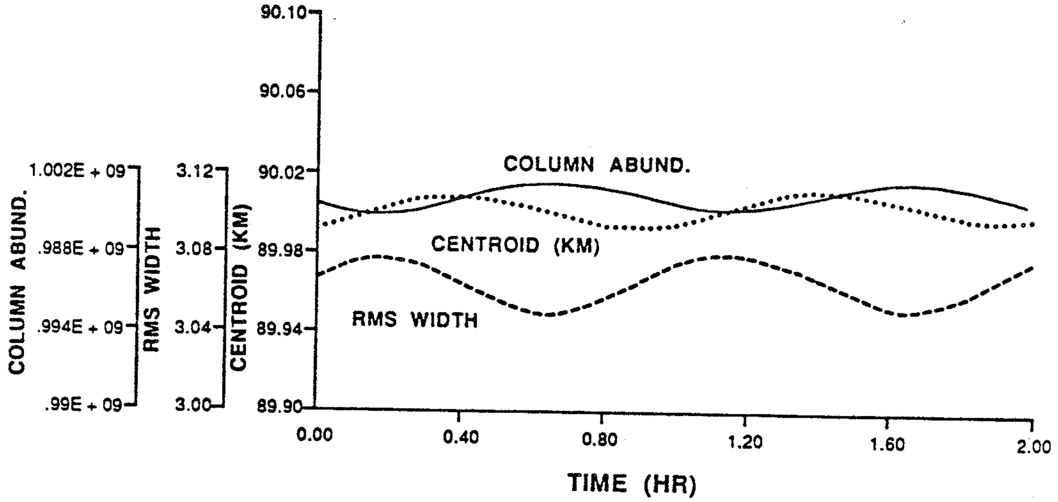

Figure 5.5 Simulated example of the amplitude and phase variations found in the height (centroid), width, and column abundance variations. The simulation has a vertical wavelength of 5 km, a period of 60 minutes, and an amplitude of 1.5 m/s.

the sodium layer, which are extentions of the one-gravity-wave model of Shelton and Gardner [1981], are derived and simulated.

5.3.1 Two-Gravity-Wave/Sodium-Layer Model

To include the effects of two gravity waves, the velocity vector for the two gravity waves is assumed to be the sum of the velocities of each gravity wave separately, i.e., $\underline{V}_T = \underline{V}_1 + \underline{V}_2$. This approach ignores the nonlinear coupling of two gravity waves and is valid only when the amplitudes of the gravity waves are small. Typically, the amplitude of the background density variations is on the order of a few percent of the neutral atmosphere; hence, the approximation is valid.

With this assumption, a perturbation series solution to Equations 5.29, 5.30 and 5.31 can be found (Gardner and Shelton [1985]). Assuming that ϕ, θ_x and θ_z can be represented as:

$$\phi(\underline{\underline{r}}, t) = \sum_{i=0}^{\infty} \phi_i(\underline{\underline{r}}, t) \qquad 5.48$$

$$\Theta_x(\underline{\underline{r}}, t) = \sum_{i=0}^{\infty} \Theta_{x_i}(\underline{\underline{r}}, t) \qquad 5.49$$

$$\Theta_z(\underline{\underline{r}}, t) = \sum_{i=0}^{\infty} \Theta_{z_i}(\underline{\underline{r}}, t) \qquad 5.50$$

it can be shown that

$$\phi_0 = -\int_{-\infty}^{t} d\tau \, \nabla \cdot \underline{\underline{V}} \qquad 5.51$$

$$\phi_i = -\int_{-\infty}^{t} d\tau \ \underline{\underline{V}} \cdot \nabla \phi_{i-1} \qquad i > 0 \qquad 5.52$$

$$\Theta_{x_0} = -\int_{-\infty}^{t} d\tau \ V_x \qquad 5.53$$

$$\Theta_{x_i} = -\int_{-\infty}^{t} d\tau \ \underline{\underline{V}} \cdot \nabla \Theta_{x_{i-1}} \qquad i > 0 \qquad 5.54$$

$$\Theta_{z_0} = -\int_{-\infty}^{t} d\tau \ V_z \qquad 5.55$$

$$\Theta_{z_i} = -\int_{-\infty}^{t} d\tau \ \underline{\underline{V}} \cdot \nabla \Theta_{z_{i-1}} \qquad i > 0 \qquad 5.56$$

ϕ_0, θ_{x0} and θ_{z0} are all terms on the order of the wave amplitude. ϕ_i, θ_{xi} and θ_{zi} are all terms on the order of the wave amplitude raised to the i+1 power. Since the wave amplitude is assumed small (typically $A\ e^{z/2H} = .03$ to $.07$), only the first two terms of the expansion are needed in the approximate expression for ϕ, θ_x and θ_z. These terms are

$$\phi_0 = -\frac{A_1}{\gamma-1} e^{z/2H} \cos(\omega_1 t - k_{x_1} x - k_{z_1} z) - \frac{A_2}{\gamma-1} e^{z/2H} \cos(\omega_2 t - k_{x_2} x - k_{z_2} z) \qquad 5.57$$

$$\phi_1 = \frac{1}{2} \left(\frac{A_1}{\gamma-1} e^{z/2H} \cos(\omega_1 t - k_{x_1} x - k_{z_1} z) \right)^2 \qquad 5.58$$

$$+ \frac{1}{2} \left(\frac{A_2}{\gamma-1} e^{z/2H} \cos(\omega_2 t - k_{x_2} x - k_{z_2} z) \right)^2$$

$$- \frac{A_1 \; A_2}{\gamma - 1} (\underline{\underline{K}}_1 \cdot \underline{\underline{\beta}}_2 + \underline{\underline{K}}_2 \cdot \underline{\underline{\beta}}_1) \left(\frac{\sin((\omega_1 - \omega_2)\; t - (k_{x_1} - k_{x_2})\; x - (k_{z_1} - k_{z_2})\; z)}{\omega_1 - \omega_2} \right.$$

$$\left. - e^{z/H} \frac{\sin((\omega_1 + \omega_2)\; t - (k_{x_1} + k_{x_2})\; x - (k_{z_1} + k_{z_2}) z)}{\omega_1 + \omega_2} \right)$$

5.59

$$\Theta_{x_0} = - \frac{A_1 \beta_{x_1}}{\omega_1} \; e^{z/2H} \cos(\omega_1 t - k_{x_1} x - k_{z_1} z)$$

$$- \frac{A_2 \beta_{x_2}}{\omega_2} \; e^{z/2H} \cos(\omega_2 t - k_{x_2} x - k_{z_2} z)$$

5.60

$$\Theta_{x_1} = \frac{A_1^2 \; \beta_{x_1}}{2\omega_1(\gamma - 1)} \; e^{z/H} \; \cos^2(\omega_1 t - k_{x_1} x - k_{z_1} z) + \frac{A_2^2 \; \beta_{x_2}}{2\omega_2(\gamma - 1)} \; e^{z/H} \; \cos^2(\omega_2 t - k_{x_2} x - k_{z_2} z)$$

$$-A_1 A_2 \left(\frac{\beta_{x_1}}{\omega_1} k_1 \cdot \beta_2 + \frac{\beta_{x_2}}{\omega_2} k_2 \cdot \beta_1 \right) \left(\frac{\sin((\omega_1 - \omega_2) t - (\underline{\underline{k}}_1 - \underline{\underline{k}}_2) \cdot \underline{\underline{r}})}{(\omega_1 - \omega_2)} \right.$$

$$\left. - \; e^{z/H} \qquad \frac{\sin((\omega_1 + \omega_2) t - (\underline{\underline{k}}_1 + \underline{\underline{k}}_2) \cdot \underline{\underline{r}})}{(\omega_1 + \omega_2)} \right)$$

$$\Theta_{z_0} = - \frac{A_1 \beta_{z_1}}{\omega_1} \; e^{z/2H} \cos(\omega_1 t - k_{x_1} x - k_{z_1} z)$$

5.61

$$- \frac{A_2 \beta_{z_2}}{\omega_2} \; e^{z/2H} \cos(\omega_2 t - k_{x_2} x - k_{z_2} z)$$

$$\Theta_{z_1} = \frac{A_1^2\, \beta_{z_1}}{2\omega_1(\gamma-1)}\, e^{z/H} \cos^2(\omega_1 t - k_{x_1} x - k_{z_1} z) + \frac{A_2^2\, \beta_{z_2}}{2\omega_2(\gamma-1)}\, e^{z/H} \cos^2(\omega_2 t - k_{x_2} x - k_{z_2} z) \tag{5.62}$$

$$-A_1 A_2 \left(\frac{\beta_{z_1}}{\omega_1}\, \underline{\underline{K}}_1 \cdot \underline{\underline{\beta}}_2 + \frac{\beta_{z_2}}{\omega_2}\, \underline{\underline{K}}_2 \cdot \underline{\underline{\beta}}_1 \right) \left(\frac{\sin((\omega_1 - \omega_2)t - (\underline{\underline{k}}_1 - \underline{\underline{k}}_2) \cdot \underline{\underline{r}})}{(\omega_1 - \omega_2)} \right.$$

$$\left. - e^{z/H} \quad \frac{\sin((\omega_1 + \omega_2)t - (\underline{\underline{k}}_1 + \underline{\underline{k}}_2) \cdot \underline{\underline{r}})}{(\omega_1 + \omega_2)} \right)$$

with the gravity waves having the wind velocity vectors

$$\underline{\underline{V}}_1 = A_1 \operatorname{Re}[\, \underline{\underline{\beta}}_1\, e^{j(\omega_1 t - \underline{\underline{K}}_1 \cdot \underline{\underline{r}})}] \tag{5.63}$$

$$\underline{\underline{V}}_2 = A_2 \operatorname{Re}[\, \underline{\underline{\beta}}_2\, e^{j(\omega_2 t - \underline{\underline{K}}_2 \cdot \underline{\underline{r}})}] \tag{5.64}$$

The terms in ϕ, θ_x and θ_z are the sum of each gravity wave perturbation. Cross coupling of the gravity wave does not occur until the i=1 order term. This cross coupling of the two gravity waves results in sinusoidal perturbations at the sum and difference frequencies of the two waves.

By taking the first-order perturbations, using the assumption in Equation 5.27 and assuming a Gaussian shape for the sodium layer, the spatial power spectrum can be written:

$$\text{ASPS} = n_0^2 \{ e^{-\kappa\sigma_1^2} + (\frac{A_1}{2(\gamma-1)})^2 e^{-(\kappa-k_{z_1})^2\sigma_1^2} (1 + (\kappa-k_{z_1})^2 \gamma^2 H^2) + (\frac{A_2}{2(\gamma-1)})^2 e^{-(\kappa-k_{z_2})^2\sigma_1^2} (1 + (\kappa-k_{z_2})^2 \gamma^2 H^2) \} \qquad 5.65$$

where the subscript 1 refers to the first gravity wave, and the subscript 2 refers to the second gravity wave. The solution clearly shows that the two waves have no spectral interference when $k_{z1} \gg k_{z2}$ or $k_{z2} \gg k_{z1}$. When k_{z1} is approximately equal to k_{z2}, the spatial power spectrum is no longer the simple signature of one gravity wave, but is distorted by the interaction of the two gravity waves. Since the peak of the spectral components are calculated in Equation 5.38, it can be assumed if $|k_{z1}-k_{z2}| > 4\ (1/\sigma_1^2-1/\gamma^2H^2)$, then there will be little interference between the spectral components of the two waves. In the Chapter 5, this model is used to analyze the features seen in the lidar data and to identify situations when two gravity waves are present.

The effects of two gravity waves in the height, width, and column abundance can be calculated, and with assumptions similar to those in the one-gravity-wave case, the magnitude and phase of the variations for the column abundance can be written

$$|\Delta C_s|^2 = c_{11}^2\ (1+(k_{z_1}\gamma H)^2) + c_{12}^2(1+(k_{z_2}\gamma H)^2) + 2\cos(u_2-u_1)\ (c_{11}c_{12}(1+k_{z_1}k_{z_2}(\gamma H)^2)) + 2\sin(u_2-u_1)\ (c_{11}c_{12}\gamma H\ (k_{z_2}-k_{z_1})) \qquad 5.66$$

$$\text{phase}(\Delta C_s) = \tan^{-1}\left(\frac{c_{11}k_{z_1}\gamma H - c_{12}\sin(u_2-u_1) + c_{12}k_{z_2}\gamma H\cos(u_2-u_1)}{-c_{11} - c_{12}\cos(u2-u1) - c_{12}k_{z_2}\gamma H\sin(u_2-u_1)}\right) \qquad 5.67$$

$$c_{11} = \frac{A_1 C_{ss}}{\gamma-1} e^{z_s/2H} e^{-k_{z_1}^2\sigma_1^2/2}$$

$$c12 = \frac{A_2 C_{ss}}{\gamma-1} e^{z_s/2H} e^{-k_{z_2}^2\sigma_1^2/2}$$

$$u_1 = \omega_1 t - k_{x_1}x - k_{z_1}z$$

$$u_2 = \omega_2 t - k_{x_2}x - k_{z_2}z$$

The width variations can be written

$$\begin{aligned}|Z_s|^2 = {} & c_{21}^2\left(\gamma^2H^2(1-k_{z_1}^2\sigma_1^2)^2 + k_{z_1}^2\sigma_1^4\right) + c_{22}^2\left(\gamma^2H^2(1-k_{z_2}^2\sigma_1^2)^2 + k_{z_2}^2\sigma_1^4\right) \qquad 5.68\\ & + 2\cos((\omega_2-\omega_1)t - (k_{x_2}-k_{x_1})x)\,(c_{21}c_{22}(\gamma^2H^2(1-k_{z_1}\sigma_1^2)(1-k_{z_2}\sigma_1^2) + k_{z_1}k_{z_2}\sigma_1^4))\\ & + 2\sin((\omega_2-\omega_1)t - (k_{x_2}-k_{x_1})x)(-c_{21}c_{22}\gamma H\sigma_1^2(k_{z_1}(1-k_{z_2}\sigma_1^2) - k_{z_2}(1-k_{z_1}\sigma_1^2))\end{aligned}$$

$$\text{phase}(\Delta Z_s) = \tan^{-1}\left(\frac{-c_{21}k_{z_1}\sigma_1^2 + c_{22}\gamma H(1-k_{z_2}\sigma_1^2)\sin(u_2-u_1) - c_{22}k_{z_2}\sigma_1^2\cos(u_2-u_1)}{c_{21}\gamma H(1-k_{z_1}^2\sigma_1^2) + c_{22}\gamma H(1-k_{z_2}\sigma_1^2)\cos(u_2-u_1) + c_{22}k_{z_2}\sigma_1^2\sin(u_2-u_1)}\right) \qquad 5.69$$

$$c_{21} = \frac{A_1}{\gamma-1} e^{z_s/2H} e^{-k_{z_1}^2\sigma_1^2/2}$$

$$c_{22} = \frac{A_2}{\gamma-1} e^{z_s/2H} e^{-k_{z_2}^2\sigma_1^2/2}$$

and the height variations can be written

$$|\Delta\sigma_s|^2 = c_{31}^2\, k_{z_1}^2 \sigma_1^4\, (k_{z_1}^2 \sigma_1^4 + \gamma^2 H^2\, (2-k_{z_1}^2 \sigma_1^2)^2) \qquad 5.70$$

$$+\, c_{32}^2\, k_{z_2}^2 \sigma_1^4\, (k_{z_2}^2 \sigma_1^4 + \gamma^2 H^2\, (2-k_{z_2}^2 \sigma_1^2)^2)$$

$$+\, 2\cos(u_2-u_1)(c_{31}c_{32}k_{z_1}k_{z_2}\sigma_1^4(k_{z_1}k_{z_2}\sigma_1^4+\gamma^2H^2(2-k_{z_1}^2\sigma_1^2)(2-k_{z_2}\sigma_1^2)))$$

$$+\, 2\sin(u_2-u_1)(c_{31}c_{32}k_{z_1}k_{z_2}\sigma_1^6\gamma H(k_{z_2}(2-k_{z_1}^2\sigma_1^2)-k_{z_1}(2-k_{z_2}^2\sigma_1^2)))$$

$$\text{phase}(\Delta\sigma_s) = \tan^{-1}\left(\frac{c_{31}\gamma Hk_{z_1}\sigma_1^2(2-k_{z_1}^2\sigma_1^2)+c_{32}k_{z_2}^2\sigma_1^4\sin(u_2-u_1)+c_{32}\gamma Hk_{z_2}^2\sigma_1^2(2-k_{z_2}\sigma_1^2)\cdot\cos(u_2-u_1)}{c_{31}k_{z_1}^2\sigma_1^4+c_{32}k_{z_2}^2\sigma_1^4\cos(u_2-u_1)-c_{32}\gamma Hk_{z_2}\sigma_1^2(2-k_{z_2}^2\sigma_1^2)\sin(u_2-u_1)}\right)$$

$$c_{31} = \frac{A_1}{2(\gamma-1)\sigma_1}\, e^{z_s/2H}\, e^{-k_{z_1}^2\sigma_1^2/2} \qquad 5.71$$

$$c_{32} = \frac{A_2}{2(\gamma-1)\sigma_1}\, e^{z_s/2H}\, e^{-k_{z_2}^2\sigma_1^2/2}$$

These results show that, when the waves have similar amplitudes, the height, width and column-abundance variations will have a modulation of the oscillations due to the two gravity waves, with a modulation frequency of the frequency difference of the two gravity waves. Also, the height, width, and column abundance have a modulated horizontal variation with a spatial modulation frequency $k_{x2} - k_{x1}$. As expected, if one of the waves has a much larger amplitude than the other, i.e., $A_1 >> A_2$, then the solution reduces to the result found in the one gravity wave solution.

5.3.2 Model of the Gravity-Wave/Critical-Layer Effects on the Sodium layer

To explore the effects of a gravity-wave/critical-layer in the region of the sodium layer, a simple model derived by using the wind velocity calculated from a linear inviscid model is used. This model of the sodium layer is shown to produce standing waves in the lidar data, much like those waves reported by lidar groups (Clemesha et al. [1978a] and Rowlett et al. [1981]).

The model for gravity-wave motion in the vicinity of a critical layer was first examined by Booker and Bretherton [1967]. Due to the complex nature of the atmosphere, the following assumptions are needed to simplify the four equations of which describe the state of the atmosphere.

(1) Rotational effects are negligible.
(2) The mean state is in hydrostatic equilibrium, $\delta p_0/\delta z=-\rho_0 g$.
(3) The Boussinesq approximation is valid, $\nabla\cdot\underline{V}=0$.
(4) Motion is two dimensional with mean velocity $(U(z),0)$ only in the x direction.
(5) All wave motions are of perturbation magnitude and proportional to $\exp(j(\omega t-k_x x)$.
(6) Parcel motions are adiabatic.
(7) The motion is inviscid.

With these assumptions, the equations of the state of the atmosphere, Equations 5.1 through 5.4, can be reduced to

$$(U-V_{ph})\frac{\delta V_x}{\delta x} + V_z\frac{dU}{dz} + \frac{1}{\rho}\frac{\delta p'}{\delta x} = 0 \qquad 5.72$$

$$(U-V_{ph})\frac{\delta V_z}{\delta x} + \frac{\rho' g}{\rho_0} + \frac{1}{\rho}\frac{\delta p}{\delta z} = 0 \qquad 5.73$$

$$(U-V_{ph})\frac{\delta(\rho' g/\rho_0)}{\delta x} - \omega_b^2 V_z = 0 \qquad 5.74$$

and the wind velocity can be written

$$V_z = W(z)\, e^{j(\omega t - k_x x)} \qquad 5.75$$

By combining Equations 5.72 to 5.75 and noting the Brunt-Vaisala frequency is given in Equation 5.15, an equation involving only the vertical wind velocity can be derived and is written:

$$\frac{d^2W}{dz^2} + \left(\frac{\omega_b^2}{(U-V_{ph})^2} - \frac{\frac{d^2U}{dz^2}}{(U-V_{ph})} - K_x^2 \right) W = 0 \qquad 5.76$$

If the velocity shear, $U(z)=U_z\ (z-z_c)$, is assumed to be linear, then Equation 5.76 further reduces to

$$\frac{d^2W}{dz^2} + \left(\frac{\omega_b^2}{U_z^2(z-z_c)^2} - K_x^2\right) W = 0 \qquad 5.77$$

Solutions to Equation 5.77 have been by developed Booker and Bretherton [1967], Holton [1975], Fritts [1975], and many other researchers studying the critical layer. A slightly different solution to this problem is shown here by noting that Equation

5.77 is in the form of a Bessel equation of imaginary order and imaginary argument. Equation 5.77 can be reduced to the Bessel equation by using the change of variables

$$\begin{aligned} z_1 &= z - z_c \\ \lambda &= j\,K_x \\ \mu &= j\sqrt{Ri-1/4} \end{aligned} \qquad 5.78$$

where Ri is the Richardson number due to the wind shear. For the derivation here, it is assumed the wind shear has laminar flow; thus, the Richardson number is always greater then 0.25. For ease in simulations, $\mu = 1$ is used. The result of Equation 5.77 after the change of variables in Equation 5.78 is

$$z_1 \frac{d^2W}{dz_1^2} + (\lambda^2 z_1^2 - \mu^2)\, W = 0 \qquad 5.79$$

and a closed-form solution in terms of Bessel functions can be written (Abramowitz and Stegun [1972])

$$W(z) = z_1^{\frac{1}{2}}\, \zeta_{\pm\mu}(\lambda z_1) \qquad 5.80$$

where, ζ is the general form of the Bessel function. To derive the correct solution from all types of Bessel functions, it is necessary to fit the correct function form to the solution. Booker and Bretherton [1967] have shown that the wave is severely attenuated at the critical layer, $z=z_c$. Thus, the only Bessel function with this form of the solution is a Bessel function of the first kind. The complete solution can be written

$$W(z) = jA(z-z_c)^{\frac{1}{2}} J_{j\mu}(jk_x(z-z_c)) + jB\,(z-z_c)^{\frac{1}{2}} J_{-j\mu}(jk_x(z-z_c)) \qquad 5.81$$

By imposing boundary conditions at the source of the wave and the propagation condition that the gravity-wave energy propagates vertically, the constants in Equation 5.81 are that A is the amplitude of the wave and that B = 0. The wind velocity then can be written

$$W(z) = jA\,(z-z_c)^{\frac{1}{2}} J_{j\mu}(jk_x(z-z_c)) \qquad 5.82$$

Having derived the wind velocity for the gravity-wave/critical-layer situation, it is possible to derive the linear response of the sodium layer for this forcing wind velocity field. The series solution introduced in the two-gravity-wave solution can be used to derive the response. Since the Boussinesq approximation was invoked to derive Equation 5.82, the compressional term, ϕ, is zero. The term that is linear in the amplitude of the wave for θ_z can be written:

$$\theta_{z_0} = -\frac{A}{\omega}\,\mathrm{Re}[(-z-z_c)^{\frac{1}{2}} J_{j\mu}(jk_x(-(z-z_c)))\,e^{j(\omega t-k_x x)}] \qquad 5.83$$

and n can be found to be

$$n(x,z,t) \; = \; n_s(z- \; \frac{A}{\omega} \, \mathrm{Re} \, [(-(z-z_c)^{\frac{1}{2}} \, J_{j\mu}(jk_x(-(z-z_c))) \, e^{j(\omega t \, - \, k_x x)} \,] \,) \qquad 5.84$$

Simulations of the result are presented in Figure 5.6. A number of features can be observed, including: (1) the characteristic gradient amplification of the wave in the sodium layer, (2) the decrease in wavelength of the wave as it approaches the critical layer (as shown by Booker and Bretherton [1966]), (3) the attenuation of the wave as it passes through the critical layer, (4) the standing-wave effect of the gravity-wave/critical-layer. This standing wave has been noted by lidar groups observing gravity waves (Clemesha et al. [1978a] and Rowlett et al. [1981]) and thus suggests that, in fact, critical-layer observations in the region of the sodium layer can be made. And (5) the large variations in column abundance near the critical layer (92 km). These large fluctuations are due to a break down in the linearized theory of the critical layer, since no nonlinear dampening mechanisms were included in the model (such as Rayleigh friction) the fluctuations are over estimated near the singular point of Equation 5.77.

5.4 Estimation of Gravity-Wave Velocity Fields from Lidar Data

As noted in Chapter 2, the output from a sodium lidar system is sodium density measurements versus altitude. Thus, to compare the velocity fields observed in the atmosphere by other remote-

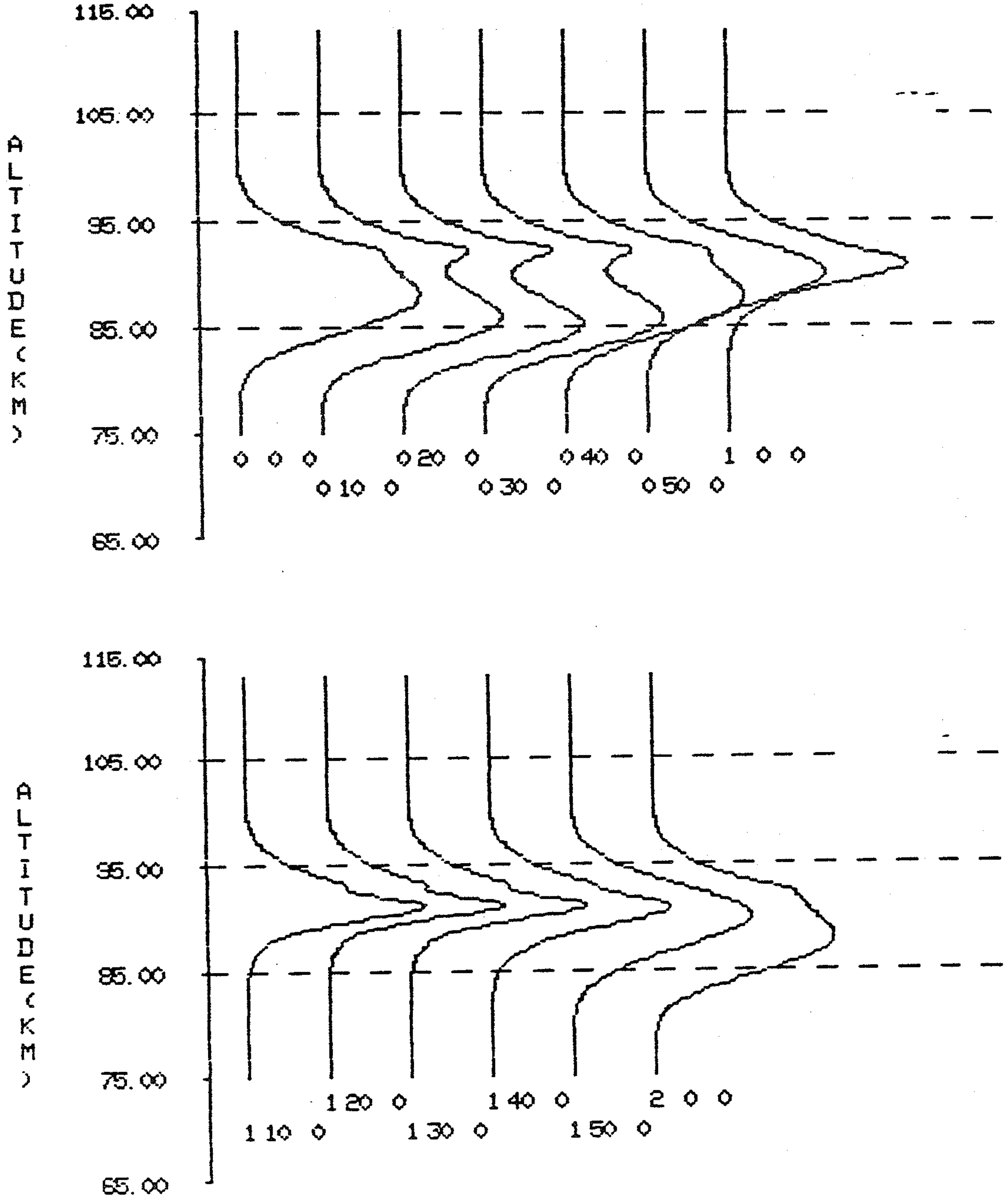

Figure 5.6 Results of the model of the critical layer near the sodium layer. The critical layer was located at 93 km altitude, the horizontal wavelength was 350 km, and the period of the wave was 120 min. The results show that a standing wave was created below the critical layer, but it was distorted by the gradient effects of the layer.

sensing techniques, it is desirable to know the relationship between the velocity field and the density perturbations. In general, this relationship between V̲ and n requires the solution of the four equations of state, but for the case of gravity waves, assuming the linear solution of Chiu and Ching [1978] and using the polarization relations, the relationship between n and V̲ can be expressed as

$$n' = \frac{-V_z}{(\gamma-1)\beta_z} \left(n_0 + \gamma H \frac{dn_0}{dz}\right) \qquad 5.85$$

or

$$V_z = \frac{-n' \cdot (\gamma-1)\, \beta_z}{n_0 + \gamma H \frac{dn_0}{dz}} \qquad 5.86$$

Thus, by fixing a point in the horizontal plane, as is the case with lidar data, the wind velocity profile can be calculated from the density profile by normalizing the gradient effects of the layer. Two problems are associated with this calculation. First, the background sodium density is not known exactly. To solve this problem, an average over the night or part of the night can be used to estimate the steady-state layer. Second, since in Equation 5.85 the gradient is in the denominator, there is a singularity when the gradient equals $-n_0/\gamma H$. This causes large perturbations in the wind estimate at the peak of the layer. To reduce this effect, a low-pass filter can be used to interpolate the points where the gradient is zero.

This technique to estimate wind profiles was performed on both simulated and actual data. Data simulated using the one-gravity-wave model with vertical wavelength of 5 km and a temporal period of one hour is shown in Figure 5.7. The results of normalizing by the gradient (Figure 5.8) show that, when the gradient approaches $-n_0/\gamma H$, the perturbations become large. The low-pass-filtered output of the wind profiles are shown in Figure 5.9 and show the sinusoidal oscillations that are characteristic of gravity waves. Also, oscillations are seen in the region outside the layer since the Gaussian distribution of sodium in the model is never equal to exactly zero. The average power spectrum of the wind profiles (Figure 5.10) shows that, with the removal of the gradient effects, only one spectral peak is observed.

The results of processing actual lidar data to produce wind velocity profiles are shown in Figure 5.11. The velocity field shows a wave of wavelength approximately 5 to 6 km. The power spectrum of the velocity field for the data in Figure 5.11 is shown in Figure 5.12 and shows a spectral peak at about 5.5 km wavelength and also a second peak at a longer wavelength. In Chapter 4, the techniques to analyze the data collected using the lidar system are developed to estimate the parameters of the gravity waves such as vertical wavelength, period, amplitude, and vertical phase speed, as well as the variability of these parameters during the night. These techniques showed that there was two dominate gravity waves present in this data at

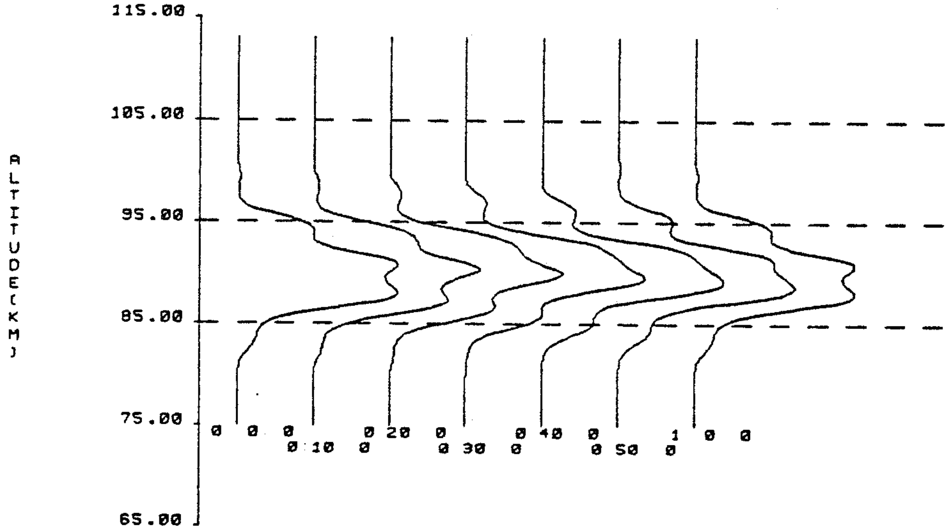

Figure 5.7 Simulated data with a wavelength of 5 km, a period of 60 min, and a amplitude of 1.5 m/s. The steady-state layer is centered at 90 km and has a width of 3 km. These data are used to calculate the wind profiles caused by gravity waves.

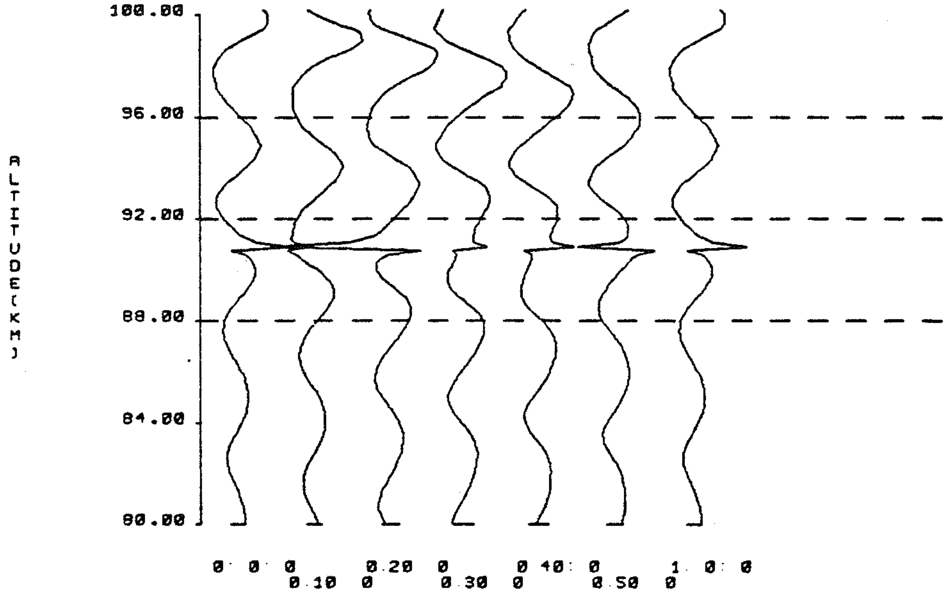

Figure 5.8 Vertical wind profiles calculated by normalizing by Equation 5.86. Note the singularity at the peak of the layer at 90 km. These profiles are calculated by removing the distortion caused by the gradient of the sodium layer and adjusting the wind using the polarization relations to calculate only the vertical component.

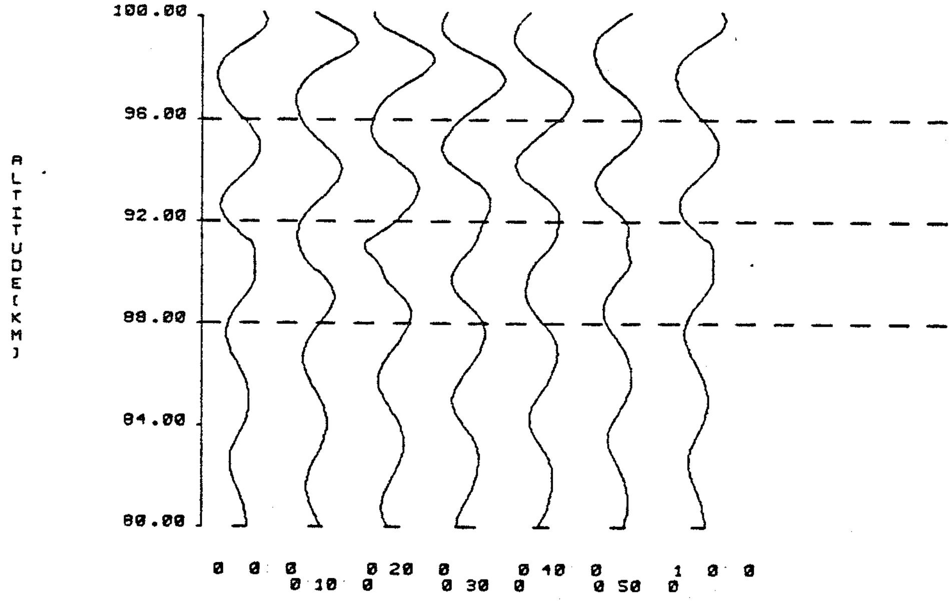

Figure 5.9 The wind profiles after spatial low-pass filtering with a cut-off frequency of 0.5 km^{-1}. The filtering interpolates the data where the gradient of the layer goes to zero thus better estimating the wind profiles. Since the layer is Gaussian (thus is never equal to zero) and no noise is present, this routine is able to estimate the wind velocity over the full range of the plot.

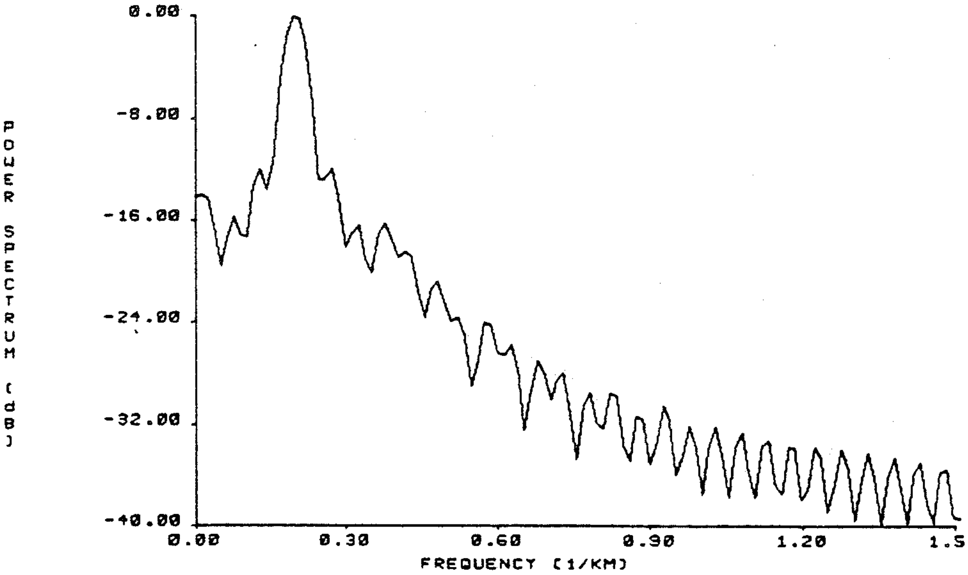

Figure 5.10 Periodogram estimate of the power spectrum of the wind profiles in Figure 5.9.

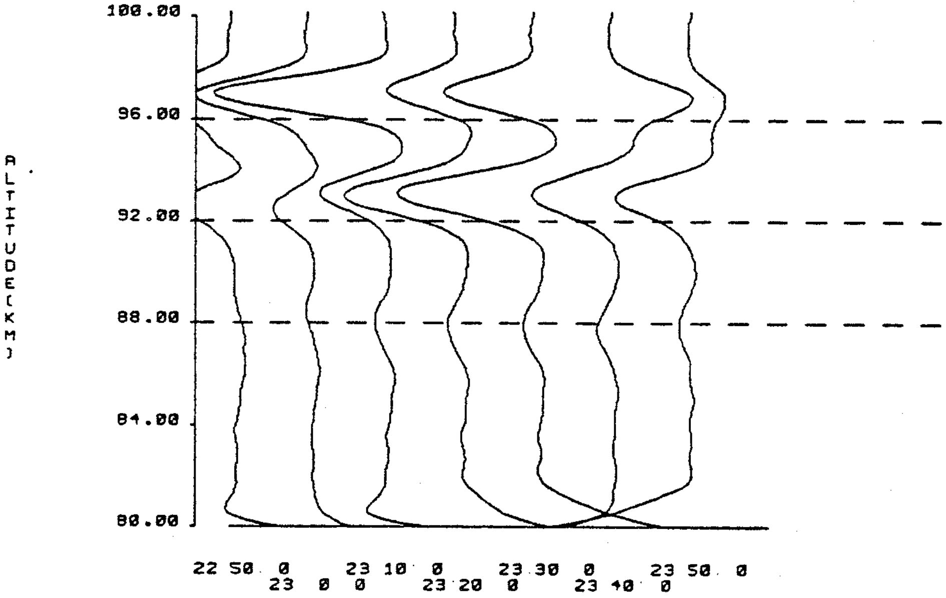

Figure 5.11 Wind velocity estimates of the data collected on March 8, 1984. The data were spatially filtered at a low-pass cut-off frequency of 0.3 km^{-1}.

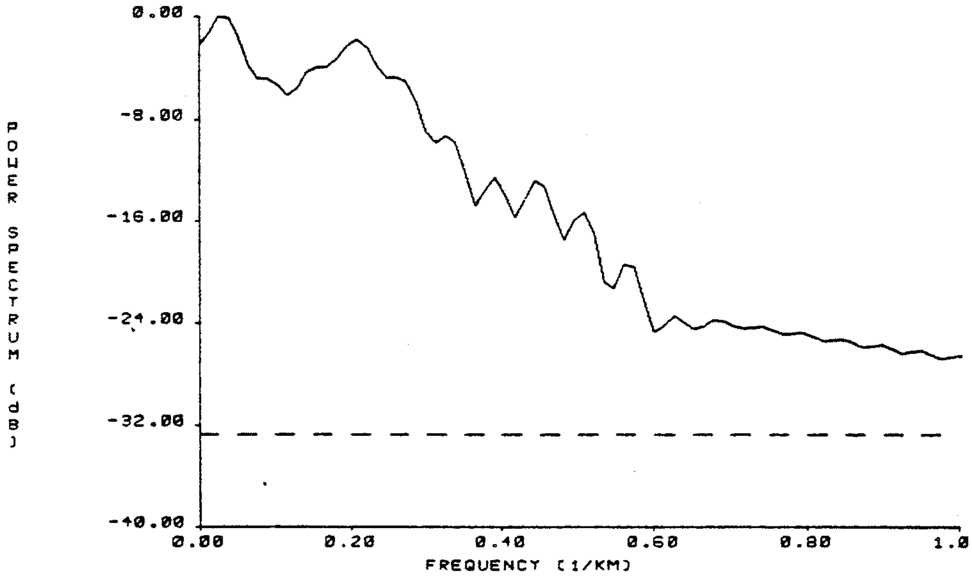

Figure 5.12 Periodogram estimate of the power spectrum of the wind profiles in Figure 5.11. The two spectral peaks imply two-gravity-wave wind fields are present. This agrees with the parameter estimation techniques, which also found that two gravity waves were present.

wavelengths of 5.5 and 12 km. Thus, this technique of calculating velocity profiles from lidar density data can improve the ability to analyze lidar data.

As noted in Figure 5.9, this technique works well on modeled data, which contains only one dominate gravity wave and no noise corrupting the data (an infinite SNR). In real data, where one dominate wave is present (Figure 5.11) this technique works but is limited to regions where the SNR is high, (i.e. where the sodium density is large and thus the signal is strong). Near the edges of the sodium layer, where the density is small, the estimation of the gradient of the sodium layer is poor due to the low SNR. This causes the vertical wind velocity calculation to be inaccurate in regions below 82 km and above 100 km.

6.0 RESULTS OF EXPERIMENTS AND DISCUSSION

During this study of the sodium layer, data were collected on 20 nights at three separate locations, including Urbana, Illinois; Wallops Island, Virginia; and White Sands, New Mexico. The nights on which data were collected are listed in Table 6.1, with the total number of raw data profiles, the shots per profile, and remarks on the type of experiment attempted.

The data were processed using techniques described in Chapter 4, and the results of the processing are discussed in this chapter. Seasonal variation of the sodium layer, nocturnal variation of the sodium layer, and observations of gravity waves in the mesosphere are discussed in relation to the data collected in studies reviewed in Chapter 2. Also, the results of the airborne lidar experiment to measure the horizontal structure of the sodium layer that was performed in March, 1983, are discussed.

6.1 <u>Seasonal Variations</u>

The seasonal variation of the sodium layer using a lidar system was first measured by Gibson and Sandford [1971] in Winkfield, England. Since that time, other groups, including Megie and Blamont [1977] in Haute Provence, France and Simonich et al. [1979] in Sao Paulo, Brazil, have made similar measurements. Since 1981, 23 nights of data were collected in

Table 6.1 Dates and Times of Lidar Experiments

Date	Time (CST)	Profiles	Shots/profile	Experiment
3/30/83	21:06-21:59	63	500	Airborne experiment in Urbana, IL simultaneous with coherent scatter
10/6/83		20	100	
10/27/83	22:45-5:29	150	500	
2/13/84	22:09-6:09	250	500	
2/20/84	20:45-4:44	460	500-250	
2/29/84	21:21-5:10	440	250	
3/8/84	20:32-5:49	640	250	
4/24/84	20:31-1:59	280	250	
6/11/84	21:07-3:44	190	250	simultaneous with meteor radar
6/12/84	21:02-2:29	153	250	"
6/14/84	20:45-2:08	125	250	"
7/17/84	20:22-3:53	400	250	
8/10/84	22:20-4:25	350	250-125	
8/13/84	21:18-4:26	560	250-125	
9/30/84	19:20-5:39	700	125	
10/19/84	01:20-5:03	100	250	At Alamo Peak, N.M. simultaneous with rocket launch at White Sands Missile Range
10/22/84	23:59-4:54	140	500	
11/12/84	20:40-6:04	845	50-100-75	In Urbana, IL
12/23/84	20:50-6:20	440	125	"
1/25/85	20:10-3:00	470	250	"

Urbana, Illinois. The majority of the night data was recorded in late 1983 or 1984, and observation periods ranged from 4 to 10 hours. A synopsis of the seasonal column abundance data is plotted in Figure 6.1, where the lines on the plot refer to the range of the column abundance values seen for that night, and the dot is the average value for the night. These results show a sharp peak in sodium abundance in November and a minimum in June. This is in general agreement with the other Northern Hemisphere observations, including those of Gibson and Sandford, Megie and Blamont, and the twilight measurements of Hunten [1967]. Simonich et al., observing in the Southern Hemisphere, also report a winter maximum and a summer minimum. The winter maximum at Urbana is sharp and restricted to the November-December months, similar to the trends found in the data of Gibson and Sandford, and Megie and Blamont, but different from the results of Simonich et al., who showed a broad winter maximum. This implies that the seasonal variations are affected by latitude, as suggested by Simonich et al. Also, our data tend to show a minimum point in June, similar to the results of Simonich et al. In contrast, Megie and Blamont report a rather broad minimum column abundance throughout the summer months. The ratio of column abundance in the winter months to the summer months at Urbana is approximately 3:1, which is the same as the results of Megie and Blamont. This supports the trend reported by Simonich et al. [1979], that the ratio of maximum column abundance to minimum column abundance depends on the latitude of the observer.

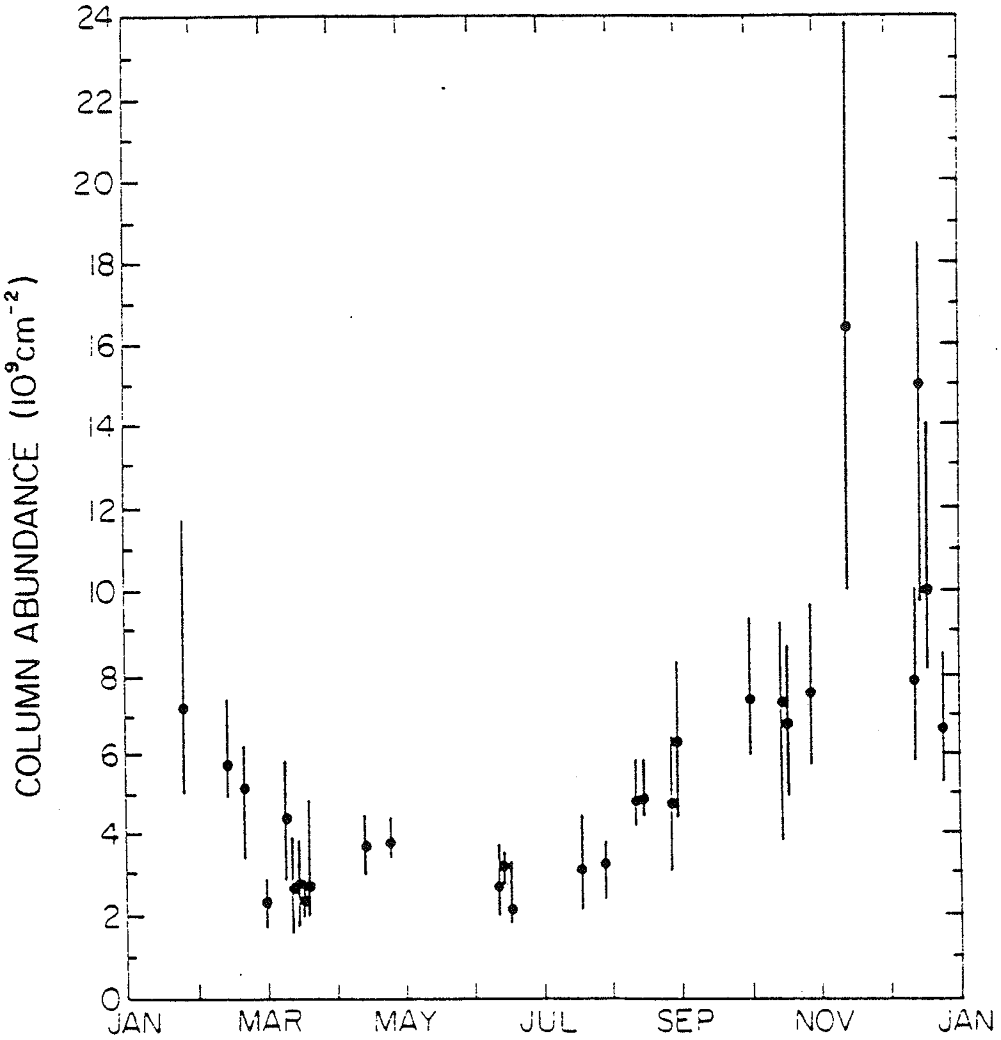

Figure 6.1 Seasonal variation of the column abundance of the data collected in Urbana. The points represent the average value of column abundance during the night. The lines are the range of values of column abundance found in that night of data.

The seasonal column abundance results at Urbana are also in agreement with the modeling results obtained by Jegou et al. [1984], which suggest that wind and temperature patterns cause seasonal variations.

Thus, although fewer data are available for the Urbana lidar site than for other sites, the trends found in the seasonal column abundance data are similar to reported trends found in other parts of the world and the latitude of the observer appears to have a large effect on the column abundance of the layer.

The height of the sodium layer was determined in this study by taking the first spatial moment (centroid) of the layer density profile. To compare the measurements of the height of the layer with those of other lidar groups, one must be aware of the differences between the measures. For example, a double peak in the layer profile, which is occasionally observed, could produce various layer height values, depending on the method of calculation. Gibson and Sandford [1971] and Simonich et al. [1979] used the height where the sodium layer reaches a maximum without considering the distribution of sodium atoms with altitude. This method could result in significantly differing height values as compared to the centroid, depending on layer shape. Megie and Blamont [1977] fit the profiles to an asymmetric Gaussian profile and from the parameters of the curve fit determined the height, width, and column abundance. This measure could also give different values for the layer height as compared to the centroid. However, the methods are similar in that all the profile points are used in the calculation. The layer height analysis done by Simonich et al. [1982] employed the centroid method used in this study.

Figure 6.2 plots the centroid of the layer as it varies during the calendar year. Again, the lines represent the variation of the centroid over the night, and the dot is the average value for the night. The centroid of the layer deviates from an average value by as much as 2.0 km during the night. The height reaches a seasonal maximum during the summer at about 92 km and a seasonal minimum during the winter at about 91.5 km. This is in general agreement with the results of Gibson and Sandford, and Megie and Blamont. Simonich et al. see no clear height variation trends in their data. Thomas et al. [1983] and Jegou et al. [1984] have proposed models that explain height effects seen in the data, as mentioned in Chapter 2.

Figure 6.3 shows the variation of the width of the sodium layer during the year. The lines in this figure are the variations of the width during the night, and the dots are the average values of the width for the night. The plot shows that the width can vary during the night from 0.4 km to 2.1 km in some cases. The width appears to have higher values in June and December and lower values in March and September, although more data are needed to substantiate this trend. Megie and Blamont [1977] showed no clear seasonal trend in width, and other lidar groups have not reported seasonal width data.

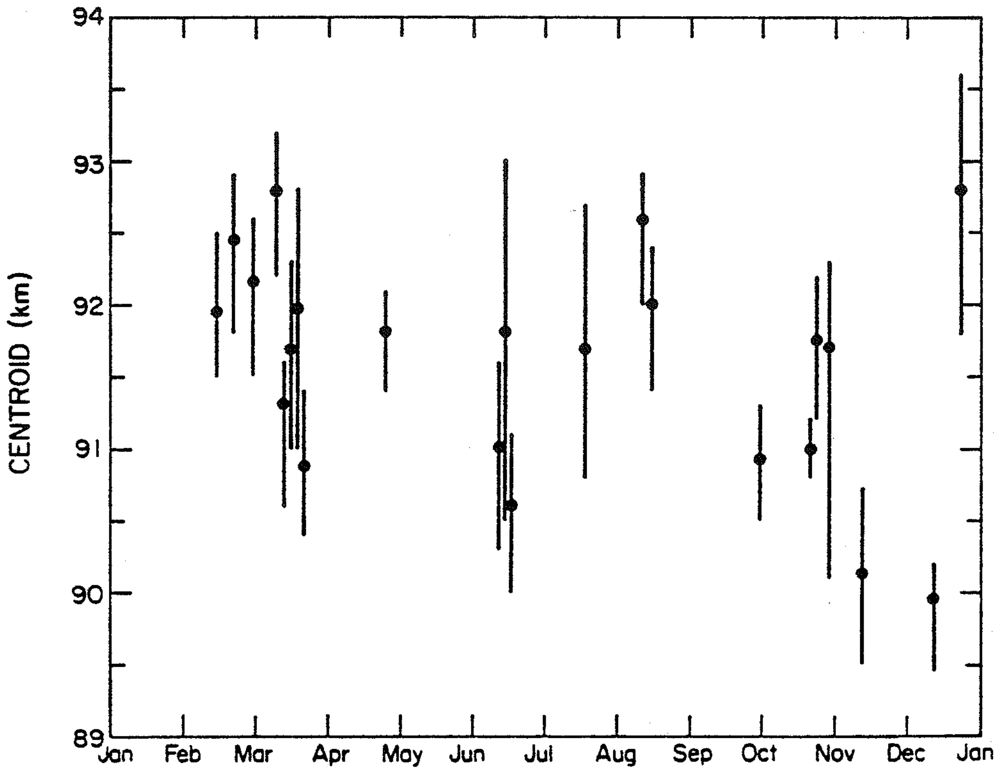

Figure 6.2 Seasonal variation of the height of the sodium layer of the data collected in Urbana. The points represent the average value of column abundance during the night. The lines are the range of values of column abundance found in that night of data.

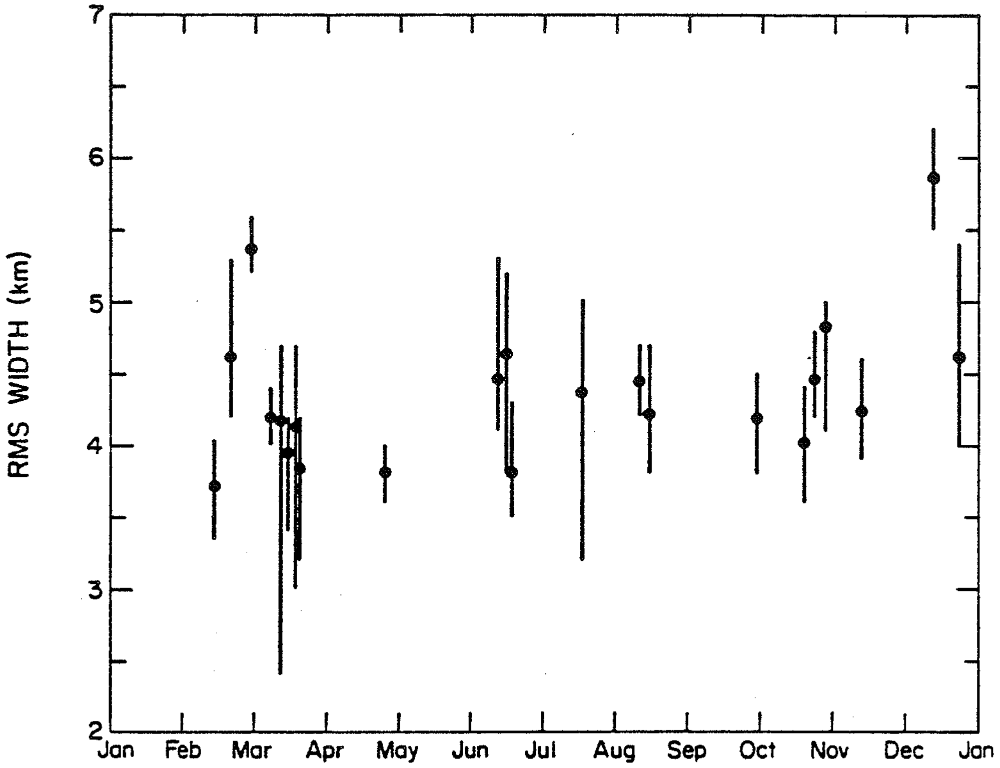

Figure 6.3 Seasonal variation of the width of the sodium layer of the data collected in Urbana. The points represent the average value of column abundance during the night. The lines are the range of values of column abundance found in that night of data.

6.2 Nocturnal Variations

The nocturnal variations of the Urbana lidar was measured from the data collected from the Urbana lidar site and processed using the procedures described in Chapter 4. To report on the mean nocturnal variations of the sodium layer over Urbana, fifteen nights of the data collected throughout the year were averaged, and a set of mean nocturnal sodium density profiles were produced. The average observation time was 7 hours during the night. To reduce the effects of the sodium abundance enhancement in the winter months, each night of data was normalized so the average column abundance was the same for all of the nights. The profiles were then averaged over the altitude and time intervals of the data. The resulting profiles were filtered at a spatial low-pass cut-off frequency of 1 km^{-1} and a temporal cutoff of 0.5 hr^{-1} (Figure 6.4). The data were then analyzed by Voelz [1985] and the following conclusions were reached:

- The most notable feature of the the density variations is that the peak of the layer reaches a maximum density near 3:00 LST (Local Standard Time). This trend was also seen in the data of Simonich et al. [1979] and Sandford and Gibson [1970]. There was a 1 hour shift (later) in the time of the peak for the data collected by Clemesha et al. [1982] during their daytime experiment, and this has been correlated to the 2,2 mode of the semidiurnal tide, which Clemesha et al. suggested was the source of these oscillations.
- The density variation at 92 km (near the peak of the layer) is about 20%, with a maximum occurring just prior to 3:00 LST.
- Sodium abundance increased on the topside of the layer (heights above 95 km), which was also observed by Simonich et al. [1979].

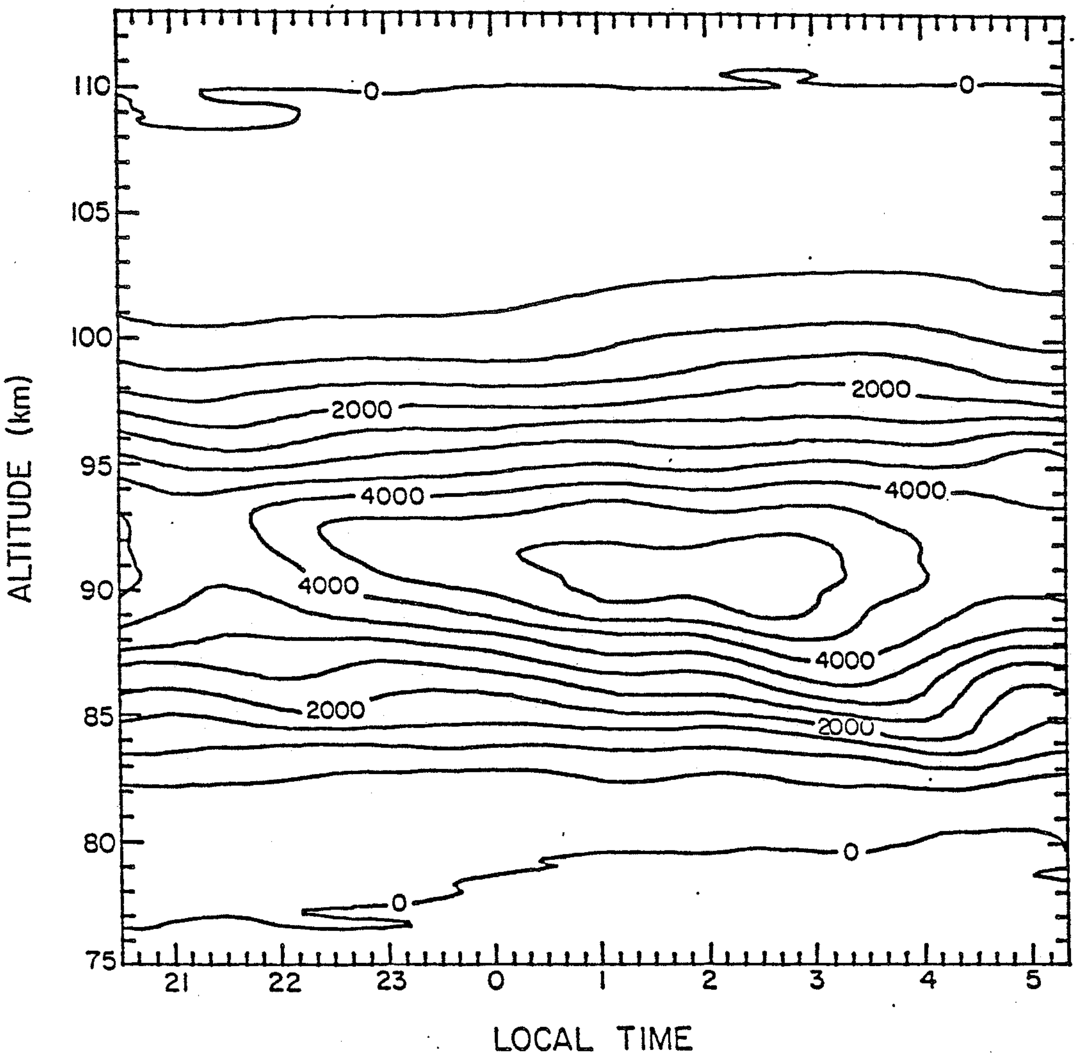

Figure 6.4 Mean nocturnal variation of sodium layer for an average of 15 nights of data collected in Urbana. The contour intervals are 500 cm^{-3}, the spatial low-pass filter cut-off is 1 km^{-1}, and the temporal low-pass filter cut-off is 0.033 min^{-1} (Voelz [1985]).

- The density at 106 km increases by 350% over the averaged data, and the scale height of the topside of the layer also increases from about 2.5 to 3.0 km. This increase in scale height was smaller than the scale height increases reported by Megie and Blamont [1977] and Simonich et al. [1979].
- The bottomside of the layer showed a sharp decrease in density during the night, dropping by a factor of 7.5. A similar decrease in density was mentioned by Kirchhoff [1983].
- The density between 83 to 88 km was stable during the night.
- The average column abundance for the data was $2.1X10^{-9}$ cm^{-2}, the average height of the layer was 91.8 km, and the average width of the layer was 4.51 km.
- The layer appears to broaden during the night. This agrees with the observations of Megie and Blamont [1977].
- The height of the layer appeared to increase slightly in contrast to the slight lowering of the layer noted by Simonich et al., possibly due to the difference in measurement techniques to calculate the layer height.

The nocturnal variations of the sodium lidar data are in general agreement with the findings of other lidar groups. A general enhancement of the layer has been traced to tidal waves. This average night analysis ignores the night-to-night variation seen in the data. These variations included a variety of shapes of the layer from very broad to very narrow, possibly due to chemical effects.

6.3 Gravity-Wave Observations

One feature observed by all of the sodium lidar groups is gravity-wave effects on the sodium layer (as mentioned in Chapter 2). Section 6.3 analyzes the lidar data to estimate the parameters of the gravity waves seen in the data. By using the techniques developed in Chapter 4, the data collected in these experiments are analyzed, and parameters of gravity-wave activity are calculated. Unfortunately, gravity-wave parameter identification is very subjective due to the variable nature of the gravity waves in the mesosphere.

6.3.1 Gravity-Wave Parameters

Table 6.2 shows the gravity-wave parameters measured from the data. In examining this table it is important to note: (1) gravity waves measured in the data varied widely, lasting from 1 to 4 hours. (2) The parameters varied during the observation interval, so an exact estimate was not possible. (3) Gravity waves increased and decreased in amplitude, possibly due to atmospheric conditions or changes in the source of the waves. Thus, gravity waves appear to fade and then reappear in the data. This variability of gravity waves lead to further investigations using the time-frequency analysis. The values presented in Table 6.2 are estimates of the average values of the gravity wave parameters during the period of observation.

Since the wave parameters are variable, it is difficult to derive conclusions about the seasonal variations of the gravity waves. Figure 6.5, which is a plot of the wavelength of the observed gravity waves over the year, shows that the wavelengths

Table 6.2 Gravity Wave Parameters from Lidar Data

Date	Vertical Wavelength (km)	Period (min)	Horizontal Wavelength (km)	Amplitude (m/s)
2/13/84	5.1	330	300	0.23
2/20/84	8.3	150	220	1.2
2/29/84	4.1	100	75	0.55
3/8/84	5.0	250	220	0.35
	2.5	87	40	0.25
4/24/84	3.1	140	80	0.49
6/11/84	6.7	130	160	1.3
6/12/84	3.7	70	45	0.35
6/14/84	10.	100	180	1.1
	3.2	50	30	0.70
7/17/84	2.5	60	25	0.73
	10.	110	200	1.1
8/10/84	11.	160	310	1.1
	5.0	90	80	1.1
8/13/84	5.0	135	120	0.44
	3.5	65	40	0.47
9/30/84	10.	250	450	0.70
	4.8	160	140	0.49
10/18/84	3.6	70	45	1.1
10/21/84	5.0	110	100	.71
11/12/84	6.7	90	107	0.86
12/23/84	5.1	270	250	.21
	2.5	160	70	.087
1/25/85	6.0	120	130	.65
	3.5	90	60	.34

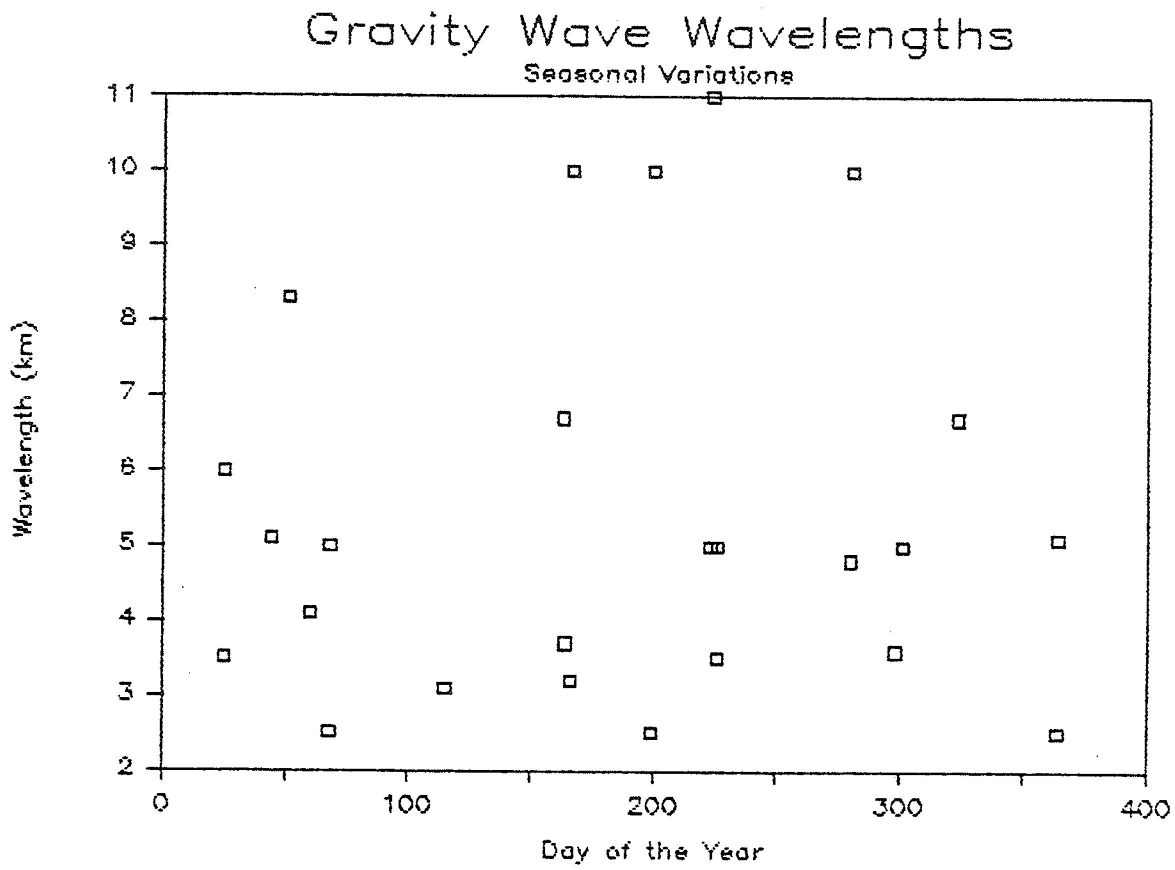

Figure 6.5 Seasonal variation of the wavelength of gravity waves. The x axis is in days of the year from 1 to 365.

tend to be longer in the summer months and shorter in the winter months. This observation agrees with the conclusions of Fritts [1984] and Hirota [1984] who found similar results using atmosphere radar data from several different latitudes. Wavelengths in the range of 6 to 12 km were observed in the summer months, but very long wavelengths were observed in the winter months. The range of gravity waves seen in the data agrees with the theoretical predictions made in Chapter 5, in which the layer was shown to be most sensitive to waves in the 5 to 6 km region for a layer width of 4 km.

Figure 6.6 shows the period of the observed gravity waves during the year. There is a slight trend for shorter period waves in the summer, but due to the variable nature of the gravity waves, it is difficult to clearly determine the period of the waves. The results of these experiments show that gravity-wave activity is an important dynamic force in the mesosphere, and that the wave activity has a seasonal variation, possibly due to changes in the sources of gravity waves.

6.3.2 Comparison of Gravity-Wave Observations with the Gravity-Wave Model

To check the theoretical model of the sodium layer, parameters estimated from the data were used in the models developed in Chapter 5. Section 6.3.2 presents an example of the results of comparing the theoretical model with the actual data and illustrates that the model accurately predicts the layer

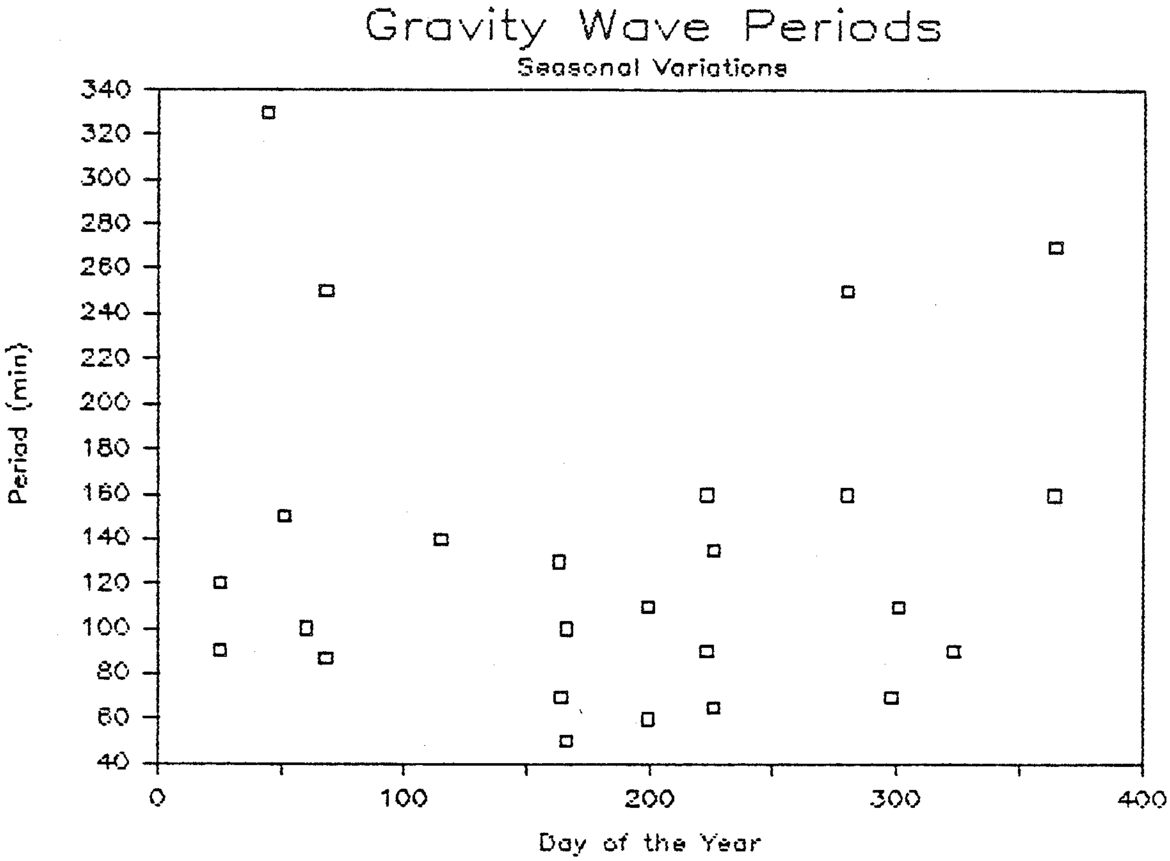

Figure 6.6 Seasonal variation of the period of gravity waves. The x axis is in days of the year from 1 to 365.

response within the restrictions of the assumptions. From the data collected on March 8, 1984, it was determined by using the periodogram and correlation techniques that two gravity waves were present from 20:30 LST to 23:30 LST. Their parameters were:

$\lambda_{z1} = 5.0$ km $\qquad \lambda_{z2} = 2.5$ km
$\lambda_{x1} = 220$ km $\qquad \lambda_{x2} = 40$ km
$T_1 = 250$ min $\qquad T_2 = 87$ min
$A_1\beta_{z1} = 0.35$ m/s $\qquad A_2\beta_{z2} = 0.25$ m/s

These parameters were used in the two-gravity-wave model developed in Chapter 5 with the average profile, $n_s(z)$, calculated from the average of the data over the interval 20:30 to 23:30. The results of the model are shown in Figure 6.7, and the data collected are shown in Figure 6.8. These figures show a close qualitative agreement between the modeled data and the actual data.

To better identify the gravity-wave features in the data, the periodogram estimate of the power spectrum of modeled data and actual data is also shown in Figures 6.7 and 6.8. The periodogram shows that the model accurately predicts the signature of the two gravity waves in the power spectrum and that the model is accurately describing the mesospheric dynamics. The signature of two gravity waves is nearly identical in both the simulated data and the lidar data, and the amplitude of the gravity waves is shown to be nearly identical by the relative values of the peak of the spectral signatures in both plots. This

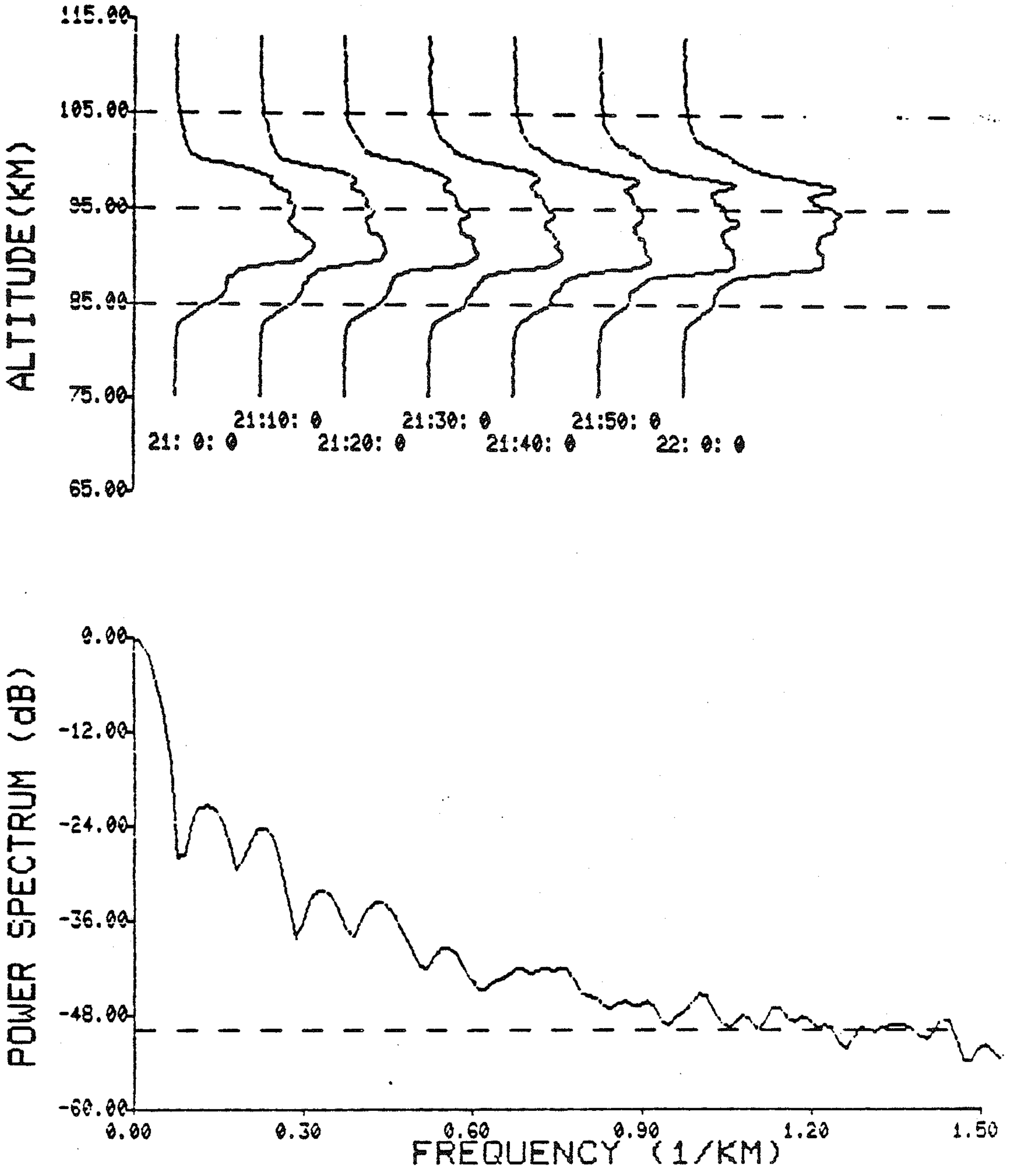

Figure 6.7 (a) Data collected at The University of Illinois lidar site on March 8, 1984, from 21:00 to 22:00 CST. The data were spatially filtered at a low-pass cut-off frequency of 1.0 km^{-1}. Each profile is the average of 2800 laser shots. (b) Periodogram estimate of the power spectrum of the data shown in (a).

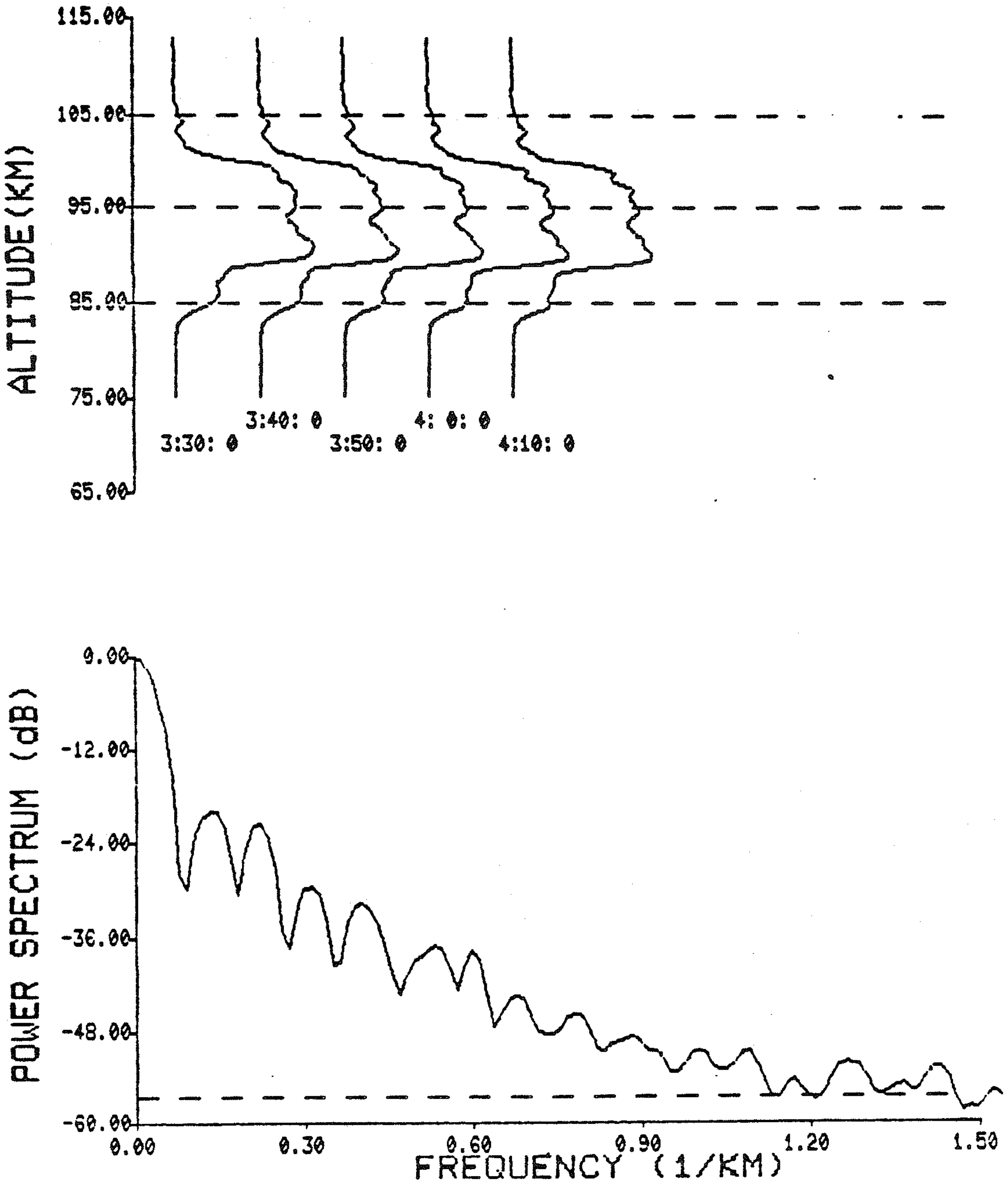

Figure 6.8 (a) Simulated profiles with the same wave parameters calculated by the estimation techniques described in Chapter 4. The steady-state profile, $n_s(z)$, was calculated from the data. (b) Spectral signatures of the gravity waves as predicted by the model. The results of the simulation closely model the actual data.

implies that, at least for short periods, the assumptions used to derive the two-gravity-wave model are valid. Thus, for gravity waves whose parameters do not vary or vary slowly with time, the model of the sodium layer predicts the effects of multiple gravity waves.

6.3.3 Variability of Gravity Waves

To study the temporal and spatial variability of gravity-wave parameters, the Wigner time-frequency distribution was introduced in Chapter 4. The results of the space-spatial frequency and time-temporal frequency analysis (discussed in Chapter 4) on the lidar data showed that the gravity-wave spectral energy does vary in space (using Wigner analysis on a spatial profile) and time (using Wigner analysis on a temporal profile). Five successive spatial profiles, analyzed using the Wigner distribution, are shown in Figures 6.9(a) to 6.9(e). These plots were made by first calculating the average spatial profile for the night and subtracting it from each of the five profiles to be analyzed. Then, for each 10-minute profile collected from 1:00 LST to 1:40 LST on February 29, 1984, the spatial Wigner distribution is calculated. In these Wigner distribution plots, each isopleth represents an increase in the spatial spectral energy at the specific altitude and spatial frequency. Thus, the contours are highest where the gravity-wave activity is the strongest both in altitude and gravity-wave spatial frequency. These plots show that the energy of the gravity

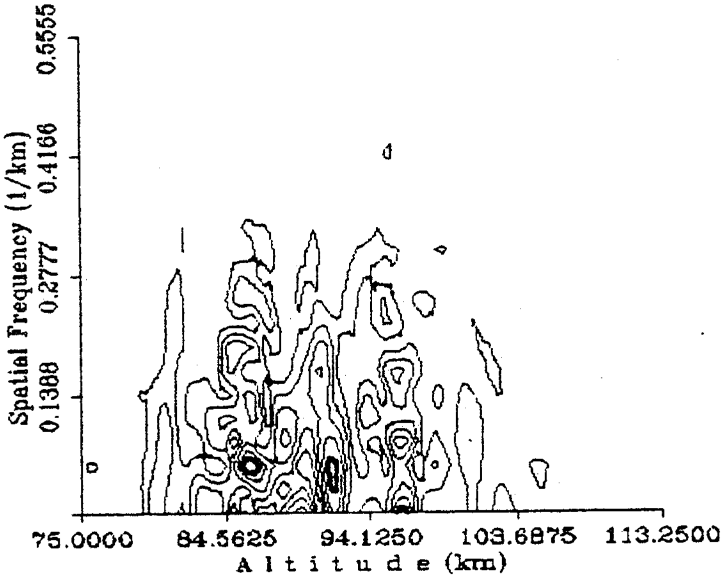

Figure 6.9(a) Series of five spatial pseudo-Wigner distributions calculated 10 minutes apart. The data were collected in Urbana on February 29, 1984, from 1:00 CST till 1:40 CST in 10 minute profiles. (a) is the profile collected at 1:00. The altitude range was from 75 km to 113.25 km.

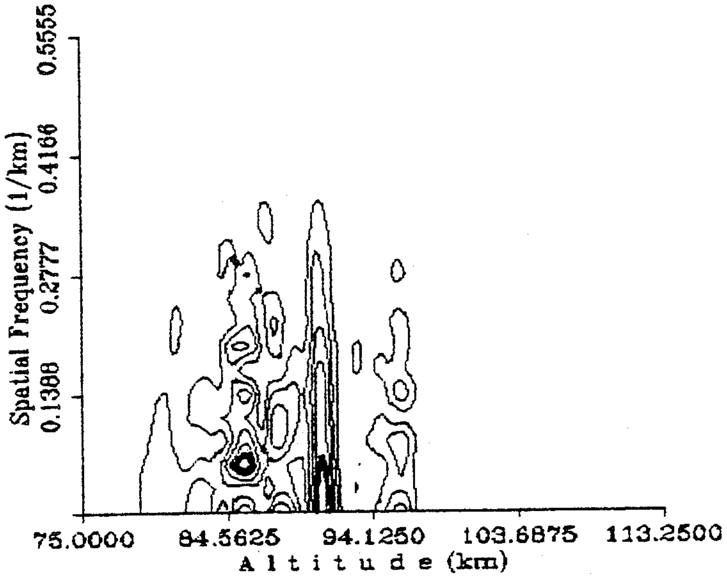

Figure 6.9(b) Spatial pseudo-Wigner distribution of data collected on February 29, 1984 at 1:10.

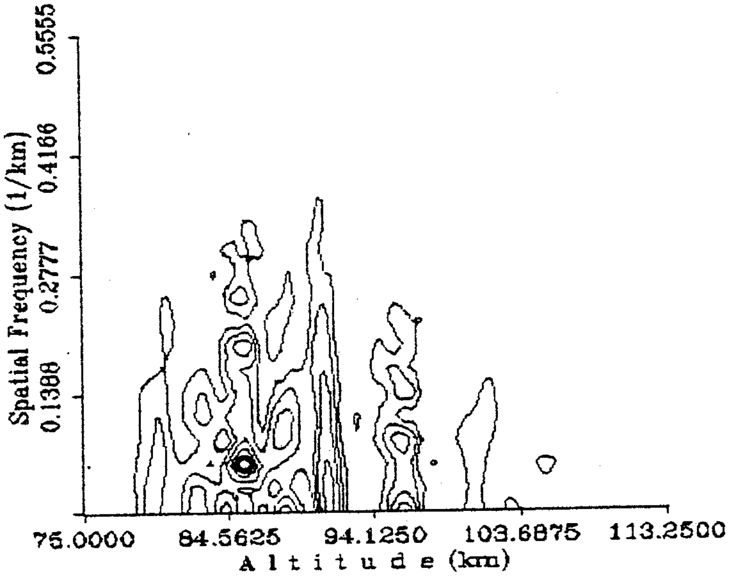

Figure 6.9(c) Spatial pseudo-Wigner distribution of data collected on February 29, 1984 at 1:20.

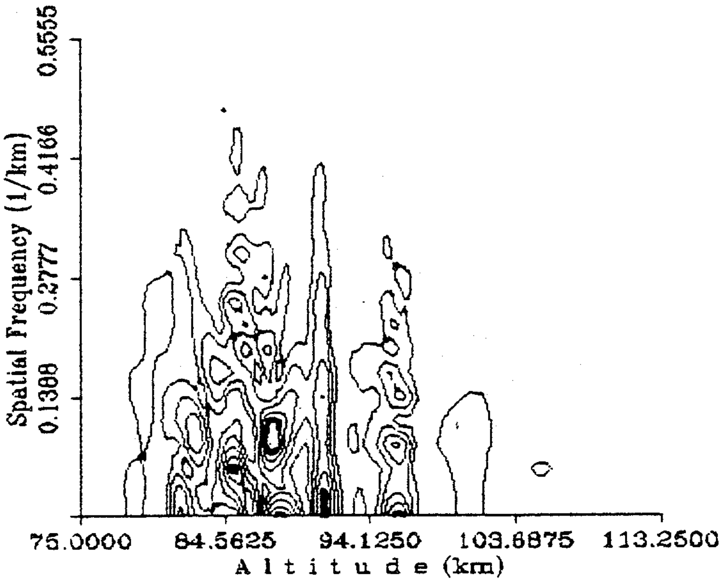

Figure 6.9(d) Spatial pseudo-Wigner distribution of data collected on February 29, 1984 at 1:30.

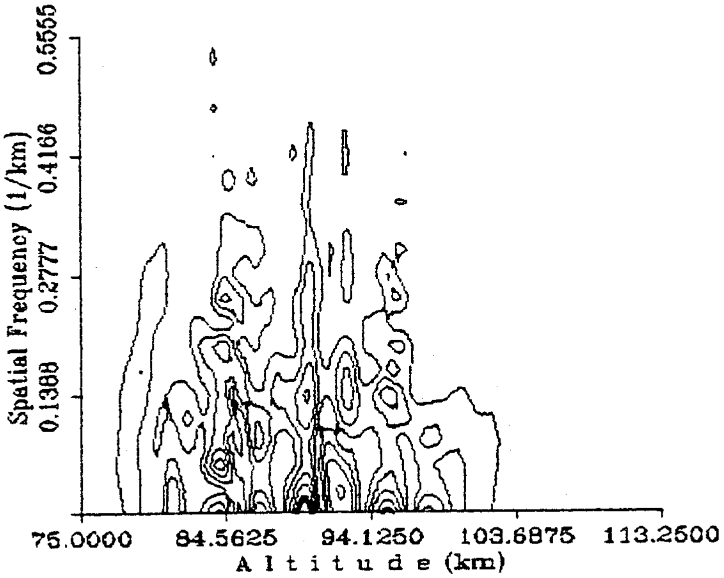

Figure 6.9(e) Spatial pseudo-Wigner distribution of data collected on February 29, 1984 at 1:40.

waves is distributed in altitude, and that the layer amplifies and attenuates the energy, as predicted by Chiu and Ching [1978]. Thus, the layer complicates the analysis of gravity-wave effects.

The peaks in all five of the Wigner distribution plots are consistent in that they appear to move down in altitude, similarly to the phase fronts of the waves. The changes in these features from plot to plot show that the gravity waves do not have uniform spatial spectral components, and the spatial wave energy actually varies in altitude. If stationary gravity waves were observed (as in simulations), there is no change in successive spatial Wigner plots.

Figures 6.10(a) through 6.10(e) show five successive temporal Wigner distributions taken at altitudes ranging from 83 to 85.5 km. This altitude range was chosen to reduce the effect of the layer gradient, since the gradient is approximately constant in this range. Again, the higher isopleths represent stronger gravity-wave activity, but in this case, the energy is in the time-temporal frequency domain. It is clear that the wave energy changes during the night. Also, as in the spatial Wigner distributions, the plots have temporal spectral features that can be traced from plot to plot and appear to follow the wave phase progression downward (i.e., features move to the right as they move down in altitude). The variability of the frequency distribution of energy with time seems to be related to the variability of gravity waves, as noted by many authors (Hirota [1984]; Witt [1962]; Grishin [1967]; Haurwitz and Fogle [1969];

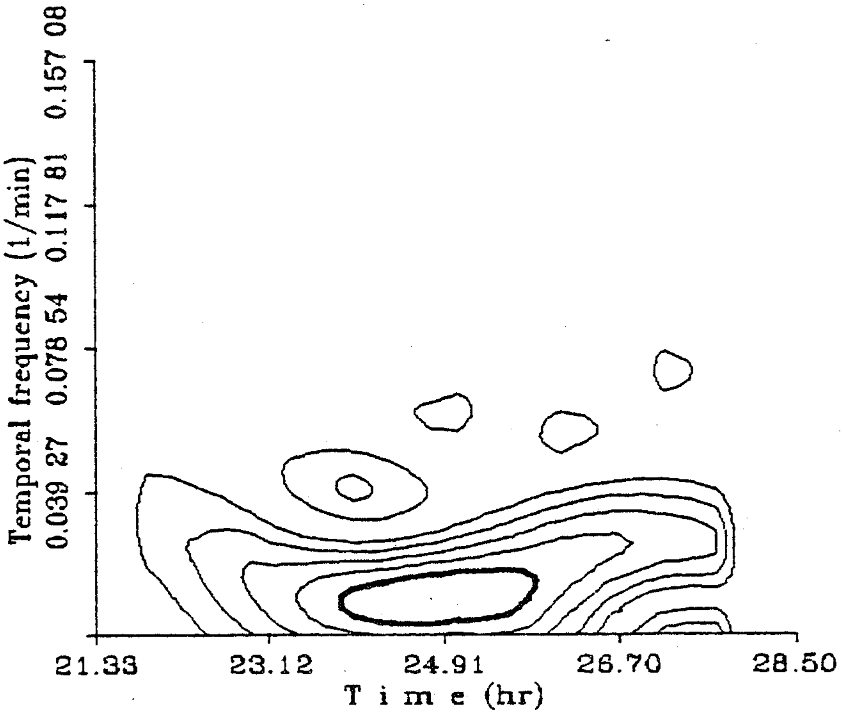

Figure 6.10(a) (a) through (e) are a series of five temporal pseudo-Wigner distribution calculated 0.5 km apart. The data were collected in Urbana on February 29, 1984, from 21:20 CST till 7:30 CST in 10 minute profiles. (a) Profile collected at the altitude 83 to 83.5 km.

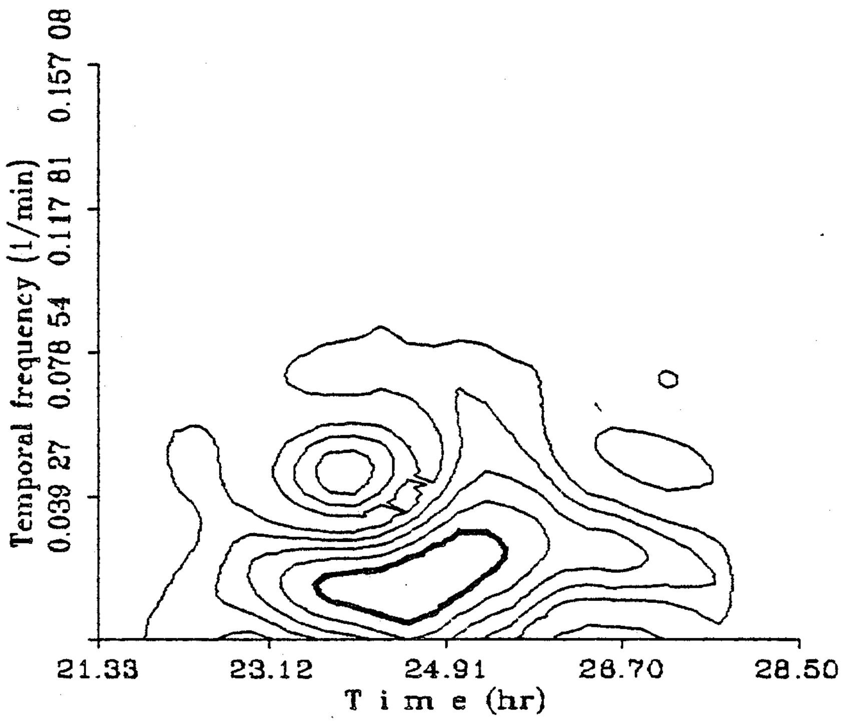

Figure 6.10(b) Temporal pseudo-Wigner distribution of data collected on February 29, 1984, at an altitude of 83.5 km to 84 km.

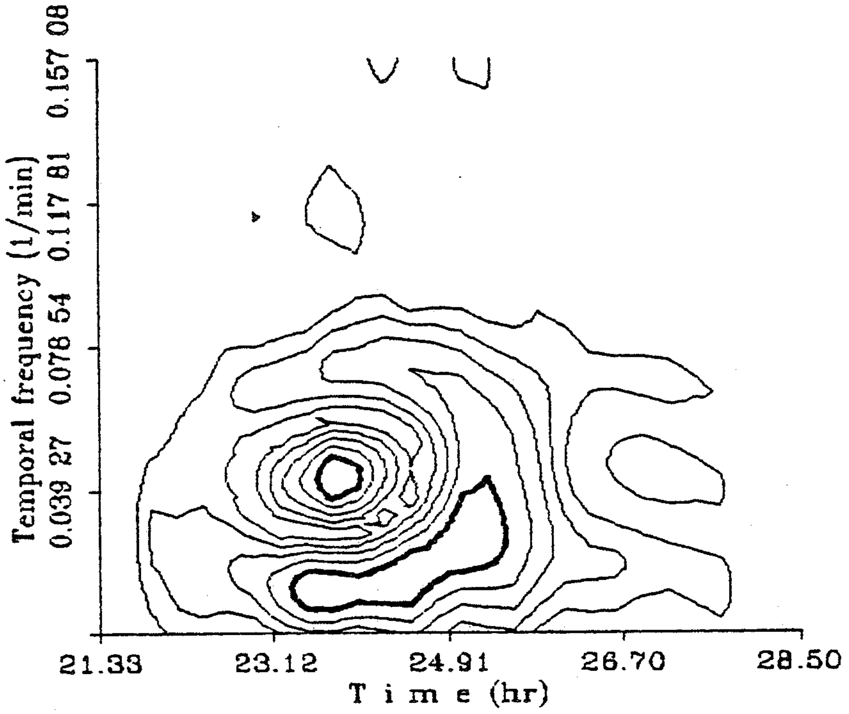

Figure 6.10(c) Temporal pseudo-Wigner distribution of data collected on February 29, 1984, at an altitude of 84 km to 84.5 km.

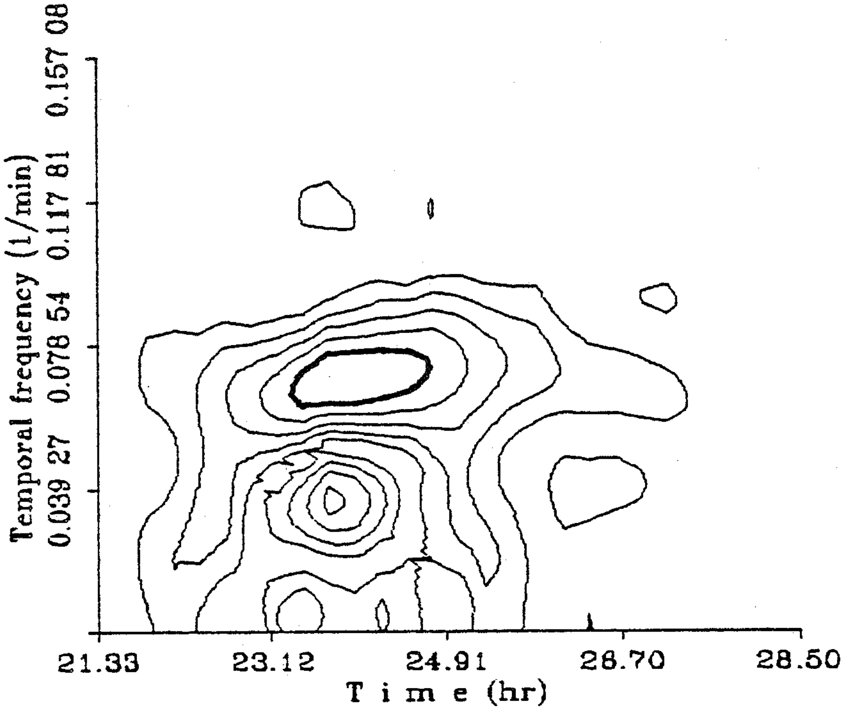

Figure 6.10(d) Temporal pseudo-Wigner distribution of data collected on February 29, 1984, at an altitude of 84.5 km to 85 km.

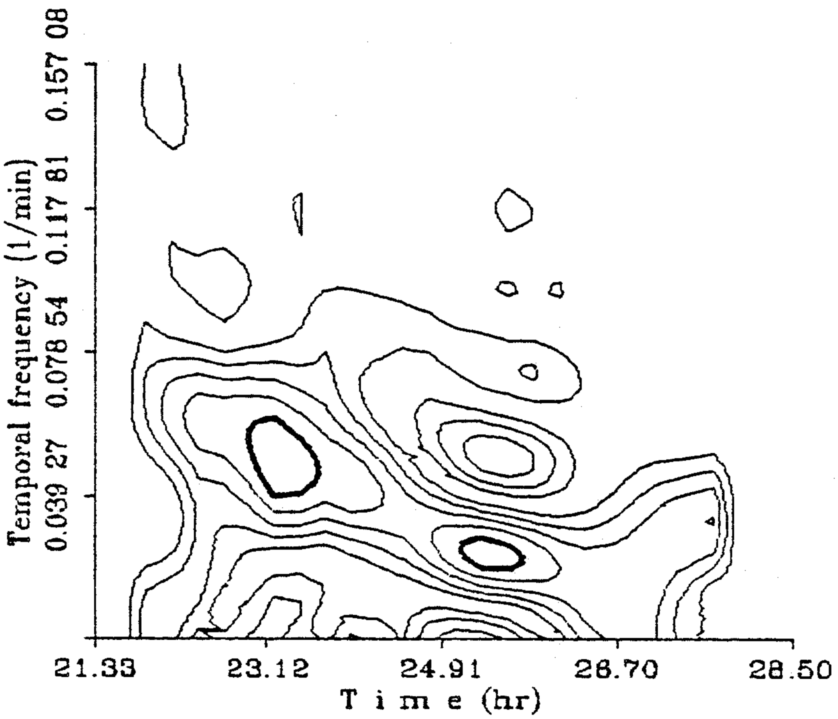

Figure 6.10(e) Temporal pseudo-Wigner distribution of data collected on February 29, 1984, at an altitude of 85 km to 85.5 km.

Carter and Balsley [1982]; Vincent and Reid [1983]; Balsley et al. [1983]; and Smith and Fritts [1983]). The Wigner distribution shows that this gravity-wave variability is also seen in the lidar data.

Thus, the Wigner distribution shows variability in both the spatial and temporal gravity-wave perturbations found in lidar data. This analysis helps to explain the gravity wave variability that complicates the estimation of gravity-wave parameters. Also, this analysis shows that spectral features in the Wigner distribution are coherent from altitude to altitude and from spatial profile to spatial profile, but these features do change in both time and space. This variability also makes it more difficult to use harmonic steady-state wave analysis to model this region of the atmosphere. Thus, it is necessary to incorporate the variability of the gravity-wave sources and the time-variable effects of gravity-wave/mean-flow interaction to produce models that better represent the atmosphere.

6.4 Results of the Airborne Lidar Experiment

The purpose of the airborne lidar experiment was to show the feasibility of an airborne sodium lidar system and to observe the horizontal structure of sodium. This work did not relate to the investigation of the gravity waves in the mesosphere due to the short observation time of the experiment and the large horizontal phase velocity of the gravity waves (typically two to three times the speed of the airplane).

The airborne lidar experiment was performed in the National Aeronautics and Space Administration (NASA) Lockheed Electra L-188 turboprop aircraft. The University of Illinois lidar system was used (see Chapter 3), with the exception of the receiving telescope, which was a NASA 16 inch f/2.5 telescope. The equipment for the experiment was bolted to optical tables mounted in the plane. The experiment was performed from 22:06 EST to 22:59 EST on March 30, 1983. The flight path was chosen due to weather conditions as a round trip from Wallops Island, Virginia (38°N, 74°W) to Albany, New York (42°N, 73°W) and back. The cruising altitude was approximately 29,000 ft, but due to spurious cirrus clouds at 30,000 ft, the data were attenuated during short periods of the experiment. The attenuated data were discarded, and the results of the experiment are plotted in Figure 6.11.

Figure 6.11 shows some interesting results of the experiment. First, the density of sodium atoms vary in the horizontal direction. Second, since the plane passed the same point twice during the trip, one is able to tell how fast the layer changed that evening. It appears that the shape of the layer was fairly constant during the two hours and variations were on the order of other data collected. Third, even though the lidar system was at a high altitude (thus reducing the attenuation due to low altitude Rayleigh scatter), the SNR was very poor in comparison to the other data presented in this study. This was due to the smaller telescope, harsh operating conditions in the airplane, and cloudy weather conditions.

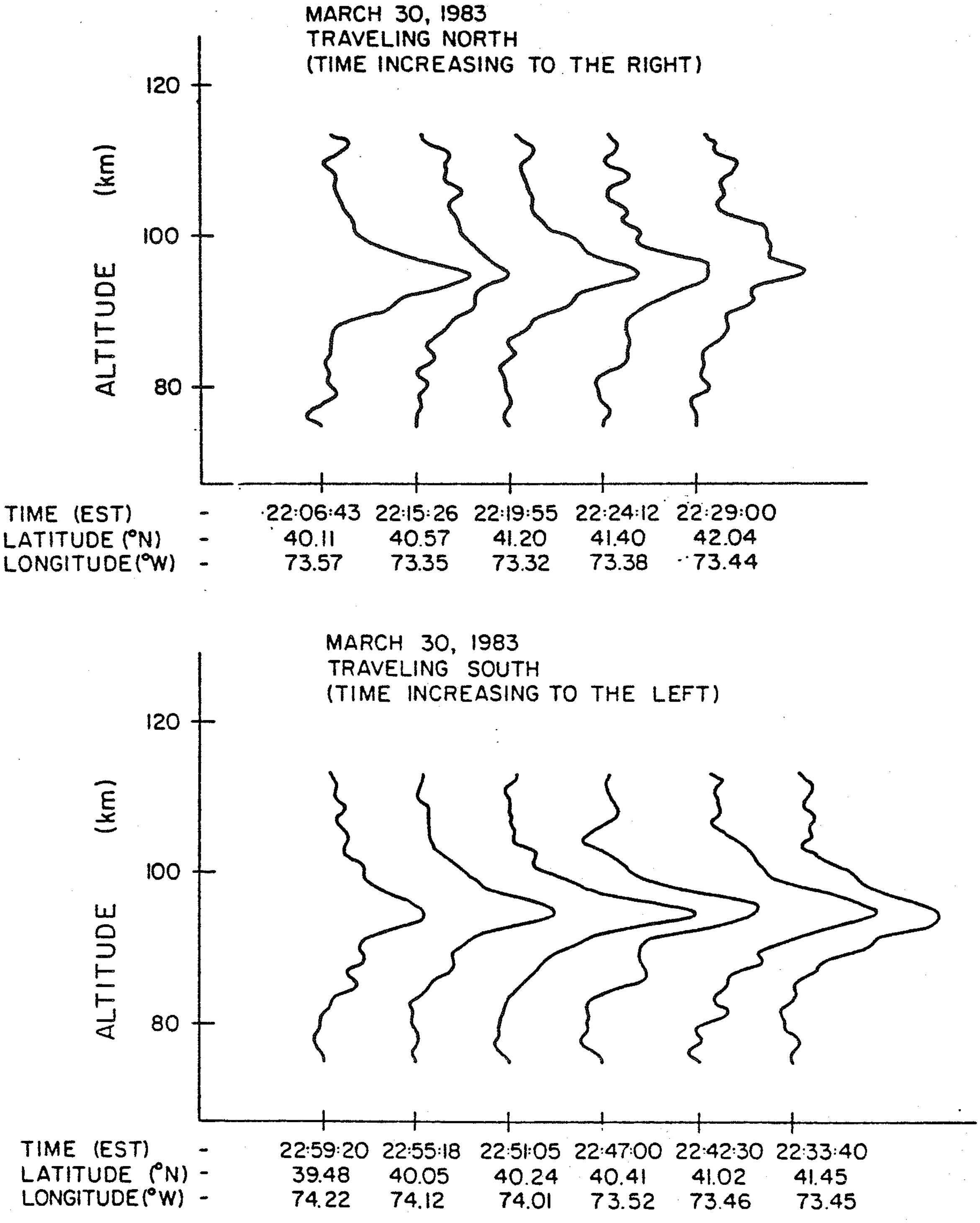

Figure 6.11 Results of the airborne lidar experiment. The data were spatially low-pass filtered at 0.3 km^{-1}.

An analysis of the data and of the problems associated with an airborne study of the horizontal structure of gravity waves, showed that it is feasible to operate a sodium lidar system in the airborne mode, but that the resulting data will have an SNR of 20 dB less than ground-based lidar data.

7.0 SUMMARY AND CONCLUSIONS

7.1 Conclusions

A laser radar system has been used to measure sodium density variations in the mesosphere. These measurements were used to trace the variations in the sodium layer, both seasonally and nocturnally. Gravity waves were also studied, and parameters of the waves were calculated using signal processing techniques. These parameters included vertical wavelength of the gravity wave, temporal period of the wave, amplitude of the wave, and horizontal wavelength. A model of the gravity-wave perturbations and their effects on the sodium layer were derived and shown to agree with the data collected with the lidar system.

The seasonal variation of the sodium layer in Urbana, Illinois, over the nights of data collected, followed trends similar to those trends found in the data of other lidar groups (Gibson and Sandford [1972], Megie and Blamont [1977], and Simonich et al. [1979]). The sodium column abundance reached a maximum of 1.6 X 10^{10} cm^{-2} on November 11, 1984, and a minimum of about 2.2 X 10^{9} cm^{-2} on June 14, 1984. The ratio of the winter (maximum) to summer (minimum) column abundance was about 3:1, which agreed with the past observations of other groups at approximately the same latitude. This agreement of the sodium layer data with past results implies that the sodium layer is uniformly distributed in longitude, since the Urbana site is not at the same longitude as the other lidar sites. Also, since Illinois is not near the ocean, it can be concluded that local geography is not important in the mesospheric sodium layer seasonal variation (although local geography is considered important in the generation of gravity waves and thus would affect the short-term variations). Density values vary between the results of the lidar groups, but since different systems were used to collect the data and different techniques were used to normalize the data, it is difficult to determine any real longitudinal variations between lidar groups. The data, which were collected three weeks apart (in Urbana, Illinois on September 30, 1984, and in Alamo Peak, New Mexico on October 18 and 21, 1984) did not reveal a significant change in the height, width, or column abundance. The height and width of the sodium layer were measured using the centroid and RMS width of the layer. The height of the layer was lower in winter (91.5 km) and higher in summer (92.0 km). The width showed no clear seasonal trends, but did vary from about 2.5 km to about 6 km over the year.

The mean nocturnal variations of the sodium layer showed a peak in column abundance near 3:00 LST, which agreed with a peak found in the early morning data presented by Clemesha et al. [1982] and Sandford and Gibson [1970]. This was attributed to the 2,2 mode of the semidiurnal tide. Also, there was an increase in the topside column abundance of the sodium layer and a decrease in the bottomside column abundance of the layer. This implies that, during one night, changes in the sources and sinks of the sodium layer produced changes in the layer distribution.

The nocturnal variations of each night of data were dominated by gravity-wave activity to some extent, and the gravity waves varied from night to night. These individual nights of data were analyzed using algorithms to estimate the parameters of the gravity waves. These algorithms used periodogram analysis of the spatial and temporal profiles of data to determine the gravity-wave parameters. Also, a correlation technique was developed to more accurately measure the wavelength and period of the gravity waves. These techniques showed that in most of the data one or two dominant frequencies could be found in the data, but in general, waves tended to be highly variable and this variability is most likely due to the variability of the sources of the gravity waves and the distortion of the gravity waves as they propagate through the atmosphere. The gravity-wave parameters which were calculated from the data were in general agreement with the trends determined by Hirota [1984].

It was noted in calculating the gravity wave parameters, that the gravity waves seemed to vary in both altitude and time. To further investigate this variability, the Wigner distribution was introduced. This distribution showed the variation of the spectral component of the gravity waves in time and thus could be used to analyze the gravity-wave variability both spatially and temporally. This analysis showed that the energy of the gravity waves was confined to temporal and spatial regions and that these regions were not stationary in time or altitude. The spectral features in the Wigner distributions were recurrent from altitude to altitude and from temporal profile to temporal profiles but varied continually.

Modeling the effects of the gravity-wave perturbations on the sodium layer showed that the layer had select frequency ranges where gravity-wave excitation produced a maximum of density response in the width, height and column abundance. The modeling also showed that the relative phase of the width, height, and column abundance variations were sensitive to the wavelength of the gravity wave. This fact can be used to analyze the lidar data by analyzing the width, height, and column abundance variations for gravity-wave perturbations.

A model using a perturbation solution for the interaction of two gravity waves and the sodium layer was presented, and experimental data were compared to the model-derived data to show that the two-gravity-wave model is valid. A model of the sodium layer response near a critical layer was presented and showed that a critical layer would produce standing waves in the data and that these standing waves would also be distorted by the layer shape effects. This standing-wave phenomena could explain the standing waves noted by Rowlett et al. [1979] and Clemesha et al. [1978]. These models, although simplistic (since they do not include chemical effects, tidal effects and diffusion), do show that a mechanistic model that includes only dynamic effects can help to analyze lidar data and to explain some of the features in the data.

An airborne experiment showed that it is feasible to collect lidar data aboard an airplane over a long baseline. This experiment also demonstrated the difficulty in measuring gravity-wave activity from an airborne platform.

7.2 Suggestions for Future Research

Future investigations of the sodium layer should include more correlative measurements. During this study, attempts were made to make sodium density measurements simultaneously or nearly simultaneously with the Urbana meteor radar, the Urbana coherent scatter radar, and an atmospheric measurement made during a rocket launch. Unfortunately, it was difficult to coordinate such experiments, and data to compare the results of these experiments are not available. More attempts at these types of correlative experiments are necessary to better understand the types of chemical and dynamical activity found in the middle atmosphere region.

Daytime experiments, like those of Gibson and Sandford [1972], would enable longer time measurements and could be compared with the results of other lidar groups. These measurements could also be used to study gravity waves during daytime hours.

More theoretical modeling of the atmosphere to include chemical effects of the atmosphere and the effects of dynamics coupled with the chemistry would produce a more realistic model of the atmosphere. Also, a dynamical model which incorporated a continuous spectrum of gravity-wave energy and also the non-stationarity of gravity waves would increase the understanding of the mesospheric region of the atmosphere.

APPENDIX A

REVIEW OF SODIUM LAYER RESEARCH

Lidar Studies

Location	Sodium Layer Seasonal Variation	Sodium Layer Short-Term Variation	Gravity Waves in the Mesosphere
Winkfield, England (51 N,.7 W)			
Bowman et al., 1970		First observations of the sodium layer using a lidar system	
Sandford and Gibson, 1970		Measuring variation of column abundance	
Gibson and Sandford, 1971	Noted the seasonal variation in height and column abundance over one year period		
Gibson and Sandford, 1972		First daytime sodium lidar, showed no change from day to night column abundance	
Thomas et al., 1977		Steerable three-point sodium lidar system, observed horizontal structure	
Gibson et al., 1979		Temperature estimates of the mesosphere the ground-state hyperfine structure of sodium	
Menlo Park, California (37 N,122 W)			
Hake et al., 1972		Enhancements of sodium during meteor showers	

Lidar Studies

Location	Sodium Layer Seasonal Variation	Sodium Layer Short Term Variation	Gravity Waves in the Mesosphere
<u>Haute-Provence, France (44 N,6 W)</u>			
Megie and Blamont, 1977	Measurements of height, width and column abundance variations for 100 nights of data	Correlation of anomalous increases of column abundance with meteor showers	Mentioned sodium perterbations due to gravity waves
Megie et al., 1978	Seasonal variation of sodium versus seasonal variation of Potassium		Dynamics of gravity waves observed
Granier and Megie, 1982	No seasonal variation in the day-to-night transition, noted a seasonal variation in the peak of sodium concentration	No regular variation during the day of the column abundance or height	Noted variation due to gravity wave
Jegou et al., 1984 series of three papers	Paper 2-Seasonal and meridional variations of alkali metals	Paper 3-Nocturnal trends shown not as important as seasonal trends	Noted importance in short term
<u>Heyess Island, USSR (80 N,50 E)</u>			
Juramy et al., 1981			Large variation of column abundance due to gravity wave
<u>Sao Paulo, Brazil (23 S,46 W)</u>			
Kirchoff and Clemesha, 1973		Variation of topside scale height, noted smaller abundance in lower latitude	

Lidar Studies

Location	Sodium Layer Seasonal Variation	Sodium Layer Short Term Variation	Gravity Waves in the Mesosphere
Clemesha et al., 1978a		Simultaneous lidar and Airglow measurements of sodium	Saw a 10 km wave and stationary waves
Simonich et al., 1979	Seasonal variation of 344 days of data no significant variation in height or structure. Similar seasonal variation in column abundance to other groups. Meridional variation.	Minimum in height of layer reached around midnight rising after that. Enhancement of column abundance in early morning	10-12 km waves, phase speeds are about 1km/hr
Clemesha et al., 1979b		Temperature dependence of sodium density	10 and 15 km wavelengths phase velocities of 1-2 km/hr
Clemesha et al., 1979a	Strong seasonal variation of column abundance in southern hemisphere		
Clemesha et al., 1980		First observation of sodium clouds	
Clemesha et al., 1981b			Calculation of wind profile from 3 point experiment, wavelengths of 10 km E-W, 5 km N-S
Clemesha et al., 1982		Continuous measurements over 4 days of variation in centroid(height) and column abundance	Observed tidal waves
Kirchoff and Takahishi, 1984		Sodium Clouds and correlation with meteor showers	

Lidar Studies

Location	Sodium Layer Seasonal Variation	Sodium Layer Short Term Variation	Gravity Waves in the Mesosphere
Bastista et al., 1985			Tidal waves modeling and observation
<u>Urbana, Illinois (40 N,88 W)</u>			
Rowlett et al., 1978			Waves on the on the order of 3-15 km
Richter et al., 1981			Waves observed 3-15 km wavelengths
Avery and Tetenbaum, 1983			Simultaneous meteor radar and lidar. 10 km waves
Gardner and Shelton, 1985			Modeled and observed gravity wave

Modeling Studies

Sodium Layer Models-A Brief Review of Origins and Variations of the Sodium Layer

Allen, 1970	Source of sodium in atmosphere evaporating sea spray
Donahue and Meier, 1967	Sodium released from a layer of dust or aerosol
Hunten and Wallace, 1967	Sodium released form a layer of dust or aerosol (independently from Donahue and Meier)
Junge et al., 1962; Gadsden, 1968, 1970	From the ablation of meteors
Fiocco and Visconti, 1974	Proposed the seasonal temperature change of the mesosphere caused the seasonal variation of column abundance by changing the sublimation rate of sodium from dust
Narcisi, 1968; Zbinden et al., 1975; Megie and Blamont, 1977	Correlation of enhancement of sodium and meteor showers, showing sodium concentration related to meteor influx
Megie et al., 1978	Seasonal enhancement of sodium and potassium are different, thus meteor is not the only source of metallic atoms
Ferguson, 1978; Liu and Reid, 1979	Modeled meteoric influx as the source of sodium and showed the dominant species below the sodium layer is NaOH
Richter and Sechrist, 1979	Modeled sink of sodium as the higher order cluster ions with the layer shape influenced by the vertical transport of Na^+.
Hunten, 1981	Modeled meteoric influx as the source of sodium and dust of meteoric origin as the sink of sodium atoms and ions
Clemesha et al., 1981	Noted that the seasonal variation in height of the layer disagreed with Hunten's model

Modeling Studies

Sodium Layer Models-A Brief Review of Origins and Variations of the Sodium Layer

Sze et al., 1982; Kirchhoff, 1983	Changes in the estimated reaction rates for sodium revised the chemical model with a much higher production rate for NaOH. This lead to the prediction of a lowering of the sodium concentration on the bottom side of the layer.
Thomas et al., [1983]	Solved the diffusion and continuity equations for oxygen, hydrogen and sodium to examine the height distribution of sodium.
Jegou et al. [1984]	Model the seasonal variation of sodium of sodium using changes in temperature and wind patterns from winter to summer as controlling factors on the clustering of sodium atoms to water.
Swider [1985]	Modeled seasonal variation of sodium column abundance by noting the temperature dependence of the three-body process for sodium.

REFERENCES

Abramowitz M. and I. A. Stegun [1972], Handbook of Mathematical Functions, Dover Publications, Inc., N.Y.

Allen, E. R. [1970], Chemical factors regulating free alkali metal atoms in the upper atmosphere, J. Geophys. Res., 75, 2947-2950.

Armstrong, E. B. [1982], The association of visible airglow features with gravity waves, J. Atmos. Terr. Phys., 44, 325.

Avery, S. K. and D. Tetenbaum [1983], Simultaneous sodium and wind measurements in the upper mesosphere using the Urbana meteor radar and lidar systems, J. Atmos. Terr. Phys., 45, 753-764.

Balsley, B. B., W. L. Ecklund, and D. C. Fritts [1983], VHF echoes from high latitude mesosphere and lower thermosphere: Observations and interpretations, J. Atmos. Sci., 39, 2451.

Batista, P. P., B. R. Clemesha, D. M. Simonich and V. W. J. H. Kirchhoff [1985], Tidal oscillations in the atmospheric sodium layer, J. Geophys. Res., 90, 3881-3888.

Battaner E. and A. Molina [1980], Turbopause internal gravity waves, 557.7 nm airglow, and eddy diffusion coefficient, J. Geophys. Res., 85, 6803-6810.

Blamont, J. E., M. L. Chanin, and G. Megie [1972], Vertical distribution and temperature profile of the nighttime atmospheric sodium layer obtained by laser backscatter, Ann. Geophys., 28, 833-838.

Blamont, J. E. and T. M. Donahue [1961], The dayglow of the sodium D lines, J. Geophys. Res., 66, 1407-1423.

Booker, J. R. and F. P. Bretherton [1967], The critical layer for internal gravity waves in a shear flow, J. Fluid Mech., 27, 513-539.

Bowman, M. R., A. J. Gibson, and M. C. W. Sandford [1969], Atmospheric sodium measured by a tuned laser radar, Nature, 221, 456-457.

Bridges, W. B. [1978], Characteristics of an opto-galvanic effect in cesium and other gas discharge plasmas, J. Opt. Soc. Am., 68, 352-360.

Brown, T. L. [1973], The chemistry of metallic elements in the ionosphere and mesosphere, Chem. Rev., 73, 645-667.

Carter, D. A. and B. B. Balsley [1982], The summer wind field between 80 and 93 km observed by the MST radar at Poker Flat, Alaska (65° N), J. Atmos. Sci., 39, 2905-2915.

Cerny, T. and C. F. Sechrist, Jr. [1980], Calibration of the Urbana lidar system, Aeron. Rep. No. 94, Dep. Elec. Eng., Univ. Ill., Urbana, Ill.

Chanin, M. L. and A. Hauchecorne [1981], Lidar observations of gravity and tidal waves in the stratosphere and mesosphere, J. Geophys. Res., 86, 9715-9721.

Chester, D. B. [1982], The Wigner Distribution and Its Application to Speech Recognition and Analysis, Ph.D. thesis, Univ. Cincinnati, Cincinnati, Ohio.

Chiu, Y. T. and B. K. Ching [1978], The response of atmospheric and lower ionospheric layer structures to gravity waves, Geophys. Res. Lett., 5, 539-542.

CIRA [1972], COSPAR International Reference Atmosphere, Akademie-Verlag, Berlin.

Claasen, T. A. C. M. and W. F. G. Mecklenbrauker [1980a], The Wigner distribution - A tool for time-frequency signal analysis, Part 1: Continuous-time signals, Philips J. Res., 35, 217-250.

Claasen, T. A. C. M. and W. F. G. Mecklenbrauker [1980b], The Wigner distribution - A tool for time-frequency signal analysis, Part 2: Discrete-time signals, Philips J. Res., 35, 276-300.

Claasen, T. A. C. M. and W. F. G. Mecklenbrauker [1980c], The Wigner distribution - A tool for time-frequency signal analysis, Part 3: Relations with other time-frequency signal transformations, Philips J. Res., 35, 372-389.

Clemesha, B. R., V. W. J. H. Kirchhoff, and D. M. Simonich [1975], Automatic wavelength control of a flashlamp-pumped dye laser, Opt. Quant. Elec., 7, 193-196.

Clemesha, B. R., V. W. J. H. Kirchhoff, and D. M. Simonich [1978a], Simultaneous observations of the Na 5893 Å nightglow and the distribution of sodium atoms in the mesosphere, J. Geophys. Res., 83, 2499-2503.

Clemesha, B. R., V. W. J. H. Kirchhoff, and D. M. Simonich [1979a], Concerning the seasonal variation of the mesospheric sodium layer at low-latitudes, Planet. Space Sci., 27, 909-910.

Clemesha, B. R., V. W. J. H. Kirchhoff and D. M. Simonich [1981a], Comments on "A meteor ablation model of the sodium and potassium layers" by D. M. Hunten, Geophys. Res. Lett., 8, 1023-1025.

Clemesha, B. R., V. W. J. H. Kirchhoff, D. M. Simonich and P. P. Batista [1981b], Mesospheric winds from lidar observations of atmospheric sodium, J. Geophys. Res., 86 868-870.

Clemesha, B. R., V. W. J. H. Kirchhoff, D. M. Simonich and H. Takahashi [1978b], Evidence of an extra-terrestrial source for the mesospheric sodium layer, Geophys. Res. Lett., 5, 873-876.

Clemesha, B. R., V. W. J. H. Kirchhoff, D. M Simonich, H. Takahashi, and P. P. Batista [1979b], Simultaneous observations of sodium density and NaD, OH (8,3). and OI 5577-Å nightglow emissions, J. Geophys. Res., 84, 6477-6482.

Clemesha, B. R., V. W. J. H. Kirchhoff, D. M. Simonich, H. Takahashi, and P. P. Batista [1980], Spaced lidar and nightglow observations of an atmospheric sodium enhancement, J. Geophys. Res., 85, 3480-3484.

Clemesha, B. R., D. M. Simonich, P. P. Batista, and V. W. J. H. Kirchhoff [1982], The diurnal variation of atmospheric sodium, J. Geophys. Res., 87, 181-186.

Cohen, L. [1966], Generalized phase space distribution functions, J. Math. Phys., 7, 781-786.

Coy, L [1983], The Vertical Propagation of Internal Gravity Waves in a compressible atmosphere, Ph.D. thesis, Univ. Wash. Seattle, Wash.

de Bruijn, N. G. [1973], A theory of generalized functions, with applications to Wigner distribution and Weyl correspondence, Nieuw Arch. Wiskunde, 21, 205-280.

Dewan, E. M. [1985], On the nature of atmospheric waves and turbulence, Radio Science, 20, 1301-1307.

Donahue, T. M. and R. R. Meier [1967], Distribution of sodium in the daytime upper atmosphere as measured by a rocket experiment, J. Geophys. Res., 72, 2803-2839.

Dovichi, N. J., D. S. Moore, and R. A. Keller [1982], Use of the optogalvanic effect and the uranium atlas for wavelength calibration of pulsed lasers, App. Opt, 21, 1468-1473.

Dunkerton, T. J. [1981a], Wave transience in a compressible atmosphere. Part 1: Transient internal wave, mean-flow interaction, J. Atmos. Sci., 38, 281-297.

Dunkerton, T. J. [1981b], Wave transience in a compressible atmosphere. Part II: Transient equatorial waves in the quasi-biennial oscillation, J. Atmos. Sci., 38, 298-307.

Dunkerton, T. J. [1982a], Wave transience in a compressible atmosphere. Part III: The saturation of internal gravity waves in the mesosphere, J. Atmos. Sci., 39, 1042-1051.

Dunkerton, T. J. [1982b], Stochastic parameterization of gravity wave stresses, J. Atmos. Sci., 39, 1711-1725.

Ecklund, W. L. and B. B. Balsley [1981], Long-term observations of the arctic mesosphere with the MST radar at Poker Flat, Alaska, J. Geophys. Res., 86, 7775-7780.

Einaudi, F., D. P. Lalas, and G. E. Perona [1978/79], The role of gravity waves in tropospheric processes, Pure Appl. Geophys., 117, 627.

Ferguson, E. E. [1978], Sodium hydroxide ions in the stratosphere, Geophys. Res. Lett., 5, 1035-1038.

Fiocco, G. and G. Visconti [1973], On the seasonal variation of upper atmospheric sodium, J. Atmos. Terr. Phys., 35, 165-171.

Forbes, J. M. [1982a], Atmospheric tides, 1, Model description and results for the solar diurnal component, J. Geophys. Res., 87, 5222-5240.

Forbes, J. M. [1982a], Atmospheric tides, 2, The solar and lunar semidiurnal components, J. Geophys. Res., 87, 5241-5252.

Fritts, D. C. [1975], The Gravity Wave-Critical Level Interaction, Ph.D. thesis, Univ. Ill., Urbana, Ill.

Fritts, D. C. [1984a], Gravity wave saturation in the middle atmosphere: A review of theory and observations, Reviews of Geophys. and Space Phys., 22, 275-308.

Fritts, D. C. [1984b], A quasi-linear study of gravity wave saturation an self-acceleration, J. Atmos. Sci., 41, 3272-3289.

Fritts, D. C. and T. J. Dunkerton [1984], A quasi-linear study of gravity wave saturation and self acceleration, J. Atmos. Sci., 41, 3272-3289.

Fritts, D. C., M. A. Geller, B. B. Balsley, M. L. Chanin, I. Hirota, J. H. Holton, S. Kato, R. S. Lindzen, M. R. Schoeberl, R. A. Vincent, and R. F. Woodman [1984], Research status and recommendations from the Alaska workshop on gravity waves and turbulence in the middle atmosphere, Fairbanks, Alaska, 18-22 July 1983, Bull. Am. Meteorological Soc., 65, 149-159.

Fiocco, G. and G. Visconti [1974], Origin of the upper atmosphere Na from sublimating dust: a model, Ann. Geophys., 30, 517-528.

Gadsden, M. [1968], Sodium in the upper atmosphere: meteoric origin, J. Atmos. Terr. Phys., 30, 151-161.

Gadsden, M. [1970], Metallic atoms and ions in the upper atmosphere, Ann. Geophys., 26, 141-150.

Gadsden, M. and C. M. Purdy [1970], Observations of the sodium dayglow, Ann. Geophys., 26, 43-51.

Gardner, C. S. and J. D. Shelton [1981], Spatial and temporal filtering techniques for processing lidar photocount data, Opt. Lett., 6, 175-176.

Gardner, C. S. and J. D. Shelton [1985], Density response of neutral atmospheric layers to gravity wave perturbations, J. Geophys. Res., 90, 1745-1754.

Gardner, C. S., C. F. Sechrist, Jr. and J. D. Shelton [1983], High resolution lidar system for measuring the spatial and temporal structure of the mesospheric sodium layer, Optical and Laser Remote Sensing, edited by D. K. Killinger and A. Mooradian, Springer-Verlag, N. Y., 199-204.

Gardner, C. S. and D. G. Voelz [1985], Lidar measurements of gravity wave saturation in the sodium layer, submitted to Geophys. Res. Lett..

Georges, T. M. [1967], Ionospheric effects of atmospheric waves, ESSA Rep. IER 57-ITSA 54, Environ. Sci. Serv. Admin., Washington, D.C.

Gibson, A. J. and M. C. W. Sandford [1971], The seasonal variation of the night-time sodium layer, J. Atmos. Terr. Phys., 33, 1675-1684.

Gibson, A. J. and M. C. W. Sandford [1972], Daytime laser radar measurements of the atmospheric sodium layer, Nature, 239, 509-511.

Gibson, A. J., L. Thomas and S. K. Bhattacharyya [1979], Laser observations of the ground-state hyperfine structure of sodium and of temperatures in the upper atmosphere, Nature, 281, 131-132.

Granier, C. and G. Megie [1982], Daytime lidar measurements of the mesospheric sodium layer, Planet. Space Sci., 30, 169-177.

Grimshaw, R. [1975], Nonlinear internal gravity waves and their interactions with the mean wind, J. Atmos. Sci., 32, 1779-1793.

Grishin, N. I. [1967], Dynamics morphology of noctilucent clouds, Meteorol. Gidrol., 1, 23.

Hake, R. D., Jr., D. E. Arnold, D. W. Jackson, W. E. Evans, B. P. Ficklin and R. A. Long [1972], Dye-laser observations of the nighttime atomic sodium layer, J. Geophys. Res., 77, 6839-6848.

Haurwitz, B., and B. Fogle [1969], Waveforms in noctilucent clouds, Deep Sea Res., 16 85.

Herse, M., G. Moreels, and J. Clairemidi [1980], Waves in the OH emissive layer: Photogrametry and topography, Appl. Opt., 19, 355.

Hines, C. O. [1960], Internal atmospheric gravity waves at ionospheric heights, Can. J. Phys., 38, 1441-14481.

Hines, C. O. and C. A. Reddy [1967], On the propagation of atmospheric gravity waves through regions of wind shear, J. Geophys. Res., 72, 1015.

Hirota, I. [1984], Climatology of gravity waves in the middle atmosphere, in Dynamics of the Middle Atmosphere, edited by J. R. Holton and T. Matsuno, Terra Scientific Publishing Co., Terra, Tokyo, 65-75.

Holton, J. R. [1975], The Dynamic Meteorology of the Stratosphere and Mesosphere, Lancaster Press, Lancaster, Pa.

Hunten, D. M. [1967], Spectroscopic studies of the twilight airglow, Space Sci. Rev., 6, 493-573.

Hunten, D. M. [1971], Airglow - introduction and review, The Radiating Atmosphere, B. M. McCormac (ed.), Reidel Publishing Co., Dordrecht-Holland, 3-16.

Hunten, D. M. [1981], A meteor ablation model of sodium and potassium layers,Geophys. Res. Lett., 8, 369-372.

Hunten, D. M. and W. L. Godson [1967], Upper-atmospheric sodium and stratospheric warming at high latitudes, J. Atmos. Sci., 24, 80-87.

Hunten, D. M. and L. Wallace [1967], Rocket measurements of the sodium dayglow, J. Geophys. Res., 72, 69-79.

Janse, C. P. and Kaizer, J. M. [1983], Time-frequency distribution of loudspeakers: The application of the Wigner distribution, J. Audio Eng. Soc., 31, 198-222.

Jegou, J. P., M. L. Chanin, G. Megie, and J. E. Blamont [1980], Lidar measurements of atmospheric lithium, Geophys. Res. Lett., 7, 995-998.

Jegou, J. P., C. Granier, M. L. Chanin, and G. Megie [1984], General theory of the alkali metals present in the earth upper atmosphere, series of three papers to be published.

Jones, W. L. [1969], Ray tracing for internal gravity waves, J. Geophys. Res., 74, 2028-2033.

Junge, C. E., O. Oldenberg, and J. T. Wasson [1962], On the origin of sodium present in the upper atmosphere, J. Geophys. Res., 67, 1027-1039.

Juramy, P., M. L. Chanin, G. Megie, G. F. Toulinov and Y. P. Doudoladov [1981], Lidar sounding of the mesospheric sodium layer at high latitudes, J. Atmos. Terr. Phys., 43, 209-215.

Keller, R. A. and E. F. Zalewski [1980], Noise considerations, signal magnitudes, and detection limits in a hollow cathode discharge by optogalvanic spectroscopy, App. Opt., 19, 3301-3305.

Kent, G. S., W. Keenliside, M. C. W. Sandford and R. W. H. Wright [1972], Laser radar observations of atmospheric tides in the 70-100 km height region, J. Atmos. Terr. Phys., 34, 373-386.

Kent, G. S. and W. Keenliside [1975], Laser radar observations of the $_{3}{}'^{1}$ diurnal atmospheric tidal mode above Kingston, Jamaica, J. Atmos. Sci., 32, 1663-1666.

Kirchhoff, V. W. J. H. [1983], Atmospheric sodium chemistry and diurnal variations: an update, Geophys. Res. Lett., 10, 721-724.

Kirchhoff, V. W. J. H. and P. P. Batista [1983], Calculation of the vertical drift of the sodium ion, Ann. Geophys., 1, 509-514.

Kirchhoff, V. W. J. H. and B. R. Clemesha [1973], Atmospheric sodium measurements at 23° S, J. Atmos. Terr. Phys., 35, 1493-1498.

Kirchhoff, V. W. J. H. and B. R. Clemesha [1983], The atmospheric neutral sodium layer 2. Diurnal variations, J. Geophys. Res., 88, 442-452.

Kirchhoff, V. W. J. H., B. R. Clemesha, and D. M. Simonich [1981], The atmospheric neutral sodium layer 1. Recent modeling compared to measurements, J. Geophys. Res., 86, 6892-6898.

Kirchhoff, V. W. J. H., B. R. Clemesha, and D. M. Simonich [1981], Average nocturnal and seasonal variations of sodium nightglow at 23° S, 46° W, Planet. Space Sci., 29, 765-766.

Kirchhoff, V. W. J. H. and H. Takahashi [1984], Sodium clouds in the lower thermosphere, Planet. Space Sci., 32, 831-836.

Klostermeyer, J. and C. H. Liu [1978], Indication of gravity wave-meanflow interaction in upper atmospheric radar observations, Geophys. Res. Lett., 5, 507-510.

Lindzen, R. S. [1969], Data necessary for the detection and description of tides and gravity waves in the upper atmosphere, J. Atmos. Terr. Phys., 31, 449-456.

Lindzen, R. S. [1981], Turbulence and stress due to gravity wave and tidal breakdown, J. Geophys. Res., 86, 9707-9714.

Lindzen, R. S. [1984], Gravity Waves in the mesosphere, in Dynamics of the Middle Atmosphere, edited by J. R. Holton and T. Matsuno, Terra Scientific Publishing Co., Terra, Tokyo, 3-18.

Lindzen, R. S. and S. Hong [1974], Effects of mean winds and horizontal temperature gradients on solar and lunar semi-diurnal tides in the atmosphere, J. Atmos. Sci., 31, 1421-1446.

Liu, S. C. and G. C. Reid [1979], Sodium and other minor constituents of meteoric origin in the atmosphere, Geophys. Res. Lett., 6, 283-286.

Manson, A. H., J. B. Gregory, and D. G. Stephenson [1973], Winds and wave motions (70-100km) as measured by a partial reflection radiowave system, J. Atmos. Terr. Phys., 35, 2055-2067.

Manson, A. H., J. B. Gregory, and D. G. Stephenson [1975], Winds and wave motions to 110 km at mid-latitudes. IV. Coupling between internal gravity waves and the mean flow, J. Atmos. Sci., 32, 1682-1688.

Manson, A. H., C. E. Meek, and R. J. Stening [1979], The role of atmospheric waves (1.5 h-10 days) in the dynamics of the mesosphere and thermosphere of Saskatoon (52^oN, 107^oW) during four seasons of 1976, J. Atmos. Terr. Phys., 41, 325-335.

Manson, A. H., C. E. Meek, and J. B. Gregory [1981], Gravity waves of short period (5-90 min), in the lower thermosphere at 52^0 N (Saskatoon, Canada); 1978/1979, J. Atmos. Terr. Phys., 43, 35-44.

Margeneau, H. and L. Cohen [1967], in Quantum Theory and Reality, edited by M. Bunge, Springer, Berlin, 71-89.

Measure, R. M. [1977], Lidar equation analysis allowing for target lifetime, laser pulse duration, and detector integration period, App. Opt., 16, 1092-1103.

Measure, R. M. [1984],Laser Remote Sensing Fundamentals and Applications, Wiley and Sons, N.Y.

Megie, G. and J. E. Blamont [1977], Laser sounding of atmospheric sodium interpretation in terms of global atmospheric parameters, Planet, Space Sci., 25, 1039-1109.

Megie, G., F. Bos, J. E. Blamont, and M. L. Chanin [1978], Simultaneous nighttime lidar measurements of atmospheric sodium and potassium, Planet. Space Sci., 26, 27-35.

Merrill, J. T. and J. R. Grant [1979], A gravity wave-critical layer encounter observed in the atmosphere, J. Geophys. Res., 84, 6315-6320.

Molina, A. [1983], Sodium nightglow and gravity waves, J. Atmos. Sci., 40, 2444-2450.

Narcisi, R. S., [1968], Processes associated with metal-ion layers in the E-region of the ionosphere, Space Res., 8, 360-369.

Nilssen, R. V. [1981], Spectral Linewidth Measurements of a Pulsed Laser, MS Thesis, University of Illinois, Urbana, IL.

Oppenheim, A. V. and R. W. Schafer [1975], Digital Signal Processing, Prentice-Hall, Englewood Cliffs, N. J.

Papoulis, A. [1965], Probability, Random Variables, and Stochastic Processes, McGraw-Hill, N.Y.

Philbrick, C. R., K. U. Grossmann, R. Henning, G. Lange, D. Krankowsky, D. Offermann, F. J. Schmidlin. and U. von Zahn [1983], Vertical density and temperature structure over Northern Europe, Adv. Space Res., 2, 121.

Pierson, W. J. Jr. and L. Moskowitz [1964], A proposed spectral form for fully developed wind seas based on the similarity Theory of S. A. Kitaigorodskii, J. Geophys. Res., 69, 5181-5190.

Rastogi, P. K. and S. A. Bowhill [1976], Scattering of radio waves from the mesosphere, 2, Evidence for intermittent mesosphere turbulence, J. Atmos. Terr. Phys., 38, 449.

Richter, E. S. and C. F. Sechrist, Jr. [1978], Theoretical and Experimental studies of the Atmospheric Sodium Layer, Aeron. Rep. No. 79, Dep. Elec. Eng., Univ. Ill., Urbana, Ill.

Richter, E. S.. and C. F. Sechrist, Jr. [1979a], A cluster ion chemistry for the mesospheric sodium layer, J. Atmos. Terr. Phys., 41, 579-586.

Richter, E. S. and C. F. Sechrist, Jr. [1979b], A meteor ablation-cluster ion atmospheric sodium theory, Geophys. Res. Lett., 6, 183-186.

Richter, E. S., J. R. Rowlett, C. S. Gardner and C. F. Sechrist, Jr. [1981], Lidar observations of the mesospheric sodium layer over Urbana, Illinois, J. Atmos. Terr. Phys., 43, 327-337.

Rottger, J. [1981], Equatorial spread-F by electric fields and atmospheric gravity waves generated by thunderstorms, J. Atmos. Terr. Phys., 43, 453-462.

Rowlett, J. R., C. S. Gardner, E. S. Richter and C. F. Sechrist, Jr. [1978], Lidar observations of wave-like structure in the atmospheric sodium layer, Geophys. Res. Lett., 5, 683-686.

Rowlett, J. R. and C. S. Gardner [1979], Signal Processing of Sodium Lidar Photocount Data, R.R.L. Publication No. 504, Radio Res. Lab., Dept. Elec. Eng., Univ. Ill., Urbana, Ill.

Sandford, M. C. W. and A. J. Gibson [1970], Laser radar measurements of the atmospheric sodium layer, J. Atmos. Terr. Phys., 35, 165-171.

Scheffler, A. O. and C. H. Liu [1985], On the observation of gravity wave spectra in the atmosphere by using MST radars, Radio Science 20, 1309-1322.

Schoeberl, M. R. and D. F. Strobel [1978], The zonally averaged circulation of the middle atmosphere, J. Atmos. Sci., 35, 577-591.

Schoeberl, M. R., D. F. Strobel, and J. P. Apruzese [1983], A numerical model of gravity wave breaking and stress in the mesosphere, J. Geophys. Res., 88, 5249-5259.

Schoeberl, M. R. [1981], The secondary flow near a baroclinic planetary wave critical line, J. Atmos. Sci., 38, 630-638.

Segal, A. C., D. Voelz, C. S. Gardner and C. F. Sechrist, Jr. [1984], Airborne lidar observations of the mesospheric sodium layer, presented at the ILRC, 1984.

Shelton, J. D., C. S. Gardner and C. F. Sechrist, Jr. [1980], Density response of the mesospheric sodium layer to gravity wave perturbations, Geophys. Res. Lett., 7, 1069-1072.

Shelton, J. D. and C. S. Gardner [1981], Theoretical and Lidar Studies of the Density Response of the Mesospheric Sodium Layer to Gravity Wave Perturbations, Aeron. Rep. No. 99, Dept. Elec. Eng., Univ. Ill., Urbana, Ill.

Slipher, V. M. [1929], Publs. Astr. Soc. Pacif., 41, 262.

Simonich, D. M. and B. R. Clemesha [1983], Resonant extinction of lidar returns from the alkali metal layers in the upper atmosphere, App. Opt., 22, 1387-1389.

Simonich, D. M., B. R. Clemesha and V. W. J. H. Kirchhoff [1979], The mesospheric sodium layer at 23° S: Nocturnal and Seasonal Variations, J. Geophys. Res., 84, 1543-1550.

Smith, S. A. and D. C. Fritts [1983], Estimation of gravity wave motions, momentum fluxes and induced mean flow accelerations in the winter mesosphere over Poker Flat, Alaska, Proc. 21 Conf. Radar Meteorol., Edmonton, Canada, 104-110.

Stening, R. G., C. E. Meek, A. H. Manson, and D. G. Stephenson [1978], Winds and wave motions to 110 km at midlatitudes, VI, Tidal, gravity and planetary waves, J. Atmos. Sci., 2194-2204.

Swider, W. [1985], Enhanced seasonal variations for chemical rates with inverse temperature dependencies: Application to seasonal abundance of mesospheric sodium, Geophys. Res. Let., 9, 589-591.

Sze, N. D., M. K. W. Ko, W. Swider, and E. Murad [1982], Atmospheric sodium chemistry I, The altitude region 70-100 km, Geophys. Res. Lett., 9, 1187-1190.

Takahashi, H., Y. Sahai, B. R. Clemesha, P. P. Batista and N. R. Teixeira [1977], Diurnal and seasonal variations of the OH (8,3) airglow band and it correlation with OI 5577 Å, Planet. Space Sci., 25, 541-547.

Tetenbaum, D. [1981], Correlative Studies of the Mesospheric Sodium Layer at Urbana, MS Thesis, University of Illinois, Urbana, Ill.

Theon, J. S., W. Nordberg, C. B. Katchen, and J. J. Horvath [1967], Some observations on the thermal behavior of the mesosphere, J. Atmos. Sci., 24, 428.

Thomas, L., A. J. Gibson, and S. K. Bhattacharyya [1976], Spatial and temporal variations of the atmospheric sodium layer observed with a steerable laser radar, Nature, 263, 115-116.

Thomas, L., A. J. Gibson, and S. K. Bhattacharyya [1977], Lidar observations of a horizontal variation in the atmospheric sodium layer, J. Atmos. Terr. Phys., 39, 1405-1409.

Thomas, L., M. C. Isherwood, and M. R. Bowman [1983], A theoretical study of the height distribution of sodium in the mesosphere, J. Atmos. Terr. Phys., 45, 587-594.

Ville, J. [1948], Théorie et applications de la notion de signal analytique, Cables et Transmissions, 20A, 61-74.

Vincent, R. A. [1984a], Gravity wave motion in the mesosphere, J. Atmos. Terr. Phys., 46, 119-128.

Vincent, R. A. [1984b], MF/HF radar measurements of the dynamics of the mesopause region-A review, J. Atmos. Terr. Phys., 46, 961-974.

Vincent, R. A. and I. M. Reid [1983], HF doppler measurements of mesospheric gravity wave momentum fluxes, J. Atmos. Sci., 40, 1321-1333.

Voelz, D. G. and C. F. Sechrist, Jr. [1983], Design and implementation of a preprocessing system for a sodium lidar, Aeron. Rep. No. 112, Dep. Elec. Eng., Univ., Ill., Urbana, Ill.

Voelz, D. G., A. C. Segal, C. S. Gardner and C. F. Sechrist, Jr. [1984], Nighttime variability of the mesospheric sodium layer structure, presented at ILRC, 1984.

Voelz, D. G. [1985], private communication.

Weinstock, J. [1976], Nonlinear theory of acoustic-gravity waves, 1. Saturation and enhanced diffusion, J. Geophys. Res., 81, 633-652.

Weinstock, J. [1978], Theory of the interaction of gravity waves with O_2(') airglow, J. Geophys. Res., 83, 5175-5185.

Weinstock, J. [1982], Nonlinear theory of gravity waves: Momentum deposition, generalized rayleigh friction, and diffusion, J. Atmos. Sci., 39, 1698-1710.

Weinstock, J. [1985], Theoretical gravity wave spectrum in the atmosphere: Strong and weak wave interactions, Radio Science 20, 1295-1300.

Wigner, E. [1930], On the quantum correction for thermodynamic equilibrium, Phys. Rev., 40, 749-759.

Witt, G. [1962], Height, structure, and displacements of noctilucent clouds, Tellus, 14, 1.

Yeh, K. C. and C. H. Liu [1985], Evolution of atmospheric spectrum by processes of wave-wave interaction, Radio Science, 20, 1279-1294.

Zbinden, P. A., M. A. Hidalgo, P. Eberhardt, and J. Geiss [1975], Mass spectrometer measurements of the positive ion composition in the D- and E-regions of the ionosphere, Planet. Space Sci., 23, 1621-1642.

VITA

Andrew Segal was born in Newark, New Jersey on August 1, 1958. He received a B.S. degree in Electrical Engineering from Rensselaer Polytechnic Institute, Troy, New York in 1980, and an M.S. degree in Electrical Engineering from the University of Illinois, Urbana-Champaign, in 1982.

He received the New Jersey State Scholarship, the RCA Scholarship, the Rensselaer Scholarship and the Harvey M. Bryans Scholarship during his undergraduate years. During the summer of 1979 he worked at Sandia National Labs in Albuquerque, New Mexico as a summer intern. After graduating from RPI he worked at Hewlett-Packard Corporation, in Cupertino, California until he returned to graduate school at the University of Illinois. While a graduate student at the University of Illinois, he was both a teaching assistant in the Department of Electrical Engineering and a research assistant at the Coordinated Sciences Laboratory and the Aeronomy Laboratory. Since March, 1985, Mr. Segal has been a Research Engineer at SRI International, Menlo Park, California.

Mr. Segal is a member of Tau Beta Pi, Eta Kappa Nu, Phi Kappa Phi, the Institute of Electrical and Electronic Engineers, the Association of Computer Machinery, and the American Geophysical Union.

Cause for nonlinear interaction between 2 gravity waves
Medium nonlinearity
Wave Eq nonlinearity